Spring 5-16-2011

The Multiplexed Squid Tes Array at Ninety Gigahertz (Mustang)

Phillip M. Korngut
University of Pennsylvania, pkorngut@physics.upenn.edu

The Multiplexed Squid Tes Array at Ninety Gigahertz (Mustang)

Abstract
The Multiplexed SQUID/TES Array at Ninety Gigahertz (MUSTANG) is a bolometric continuum imaging camera designed to operate at the Gregorian focus of the 100m Green Bank Telescope (GBT) in Pocahontas county, West Virginia. The combination of the GBT's large collecting area and the 8x8 array of transition edge sensors at the heart of MUSTANG allows for deep imaging at 10" resolution at 90GHz. The MUSTANG receiver is now a facility instrument of the National Radio Astronomy Observatory available to the general astronomical community.

The 3.3mm continuum passband is useful to access a large range of Galactic and extra-Galactic astrophysics. Sources with synchrotron, free-free and thermal blackbody emission can be detected at 3.3mm. Of particular interest is the Sunyaev Zel'dovich effect in clusters of galaxies, which arises from the inverse Compton scattering of CMB photons off hot electrons in the intra-cluster medium. In the MUSTANG band, the effect is observationally manifested as an artificial decrement in power on the sky in the direction of the cluster. There have been many experiments in the past two decades dedicated to measurements of the SZE, however, nearly all of them were accomplished with angular resolution larger than ~1'. The massive primary of the GBT enables measurements of the SZE on 10" scales. This provides a new technique to map pressure substructure in the plasma atmospheres of merging clusters of galaxies. By analyzing MUSTANG data along side X-ray data, spatially resolved measurements of the temperature, density and pressure of the ICM can be performed which can be used to infer the physics governing major mergers.

This thesis details the design, commissioning and operation of the various components which comprise the MUSTANG receiver. This includes the sub-kelvin cryogenic cooling, the time domain multiplexed readout electronics and the array of transition edge sensor bolometers. Laboratory characterization of the detector array is thoroughly described, including the measurements of the transition temperatures, thermal conductance, noise properties and time constants.

Bolometric cameras measure celestial radiation as time ordered data. To reliably produce images from traces in the time domain, care must be taken to modulate the signal in an optimized fashion during observations. Once the data are taken, algorithms must be developed to isolate the signal of interest from the foregrounds produced by atmospheric emission.

This thesis presents the techniques developed to scan, calibrate, filter and produce images from time ordered data taken with MUSTANG and the GBT.

From the Fall of 2006 to the winter of 2010, the MUSTANG receiver was commissioned on the GBT and used for a range of astrophysical measurements. The commissioning process and early science results are given in this thesis. This includes the modifications made to the instrument which have resulted in dramatically enhanced sensitivity as well as the images produced from bright extended millimeter sources such as high mass star forming regions, active galactic nuclei and supernova remnants.

This thesis presents a sample of merging clusters of galaxies imaged through their Sunyaev Zel'dovich signatures at high angular resolution. In the massive cluster RXJ1347, a previously reported pressure enhancement to the south east of the cluster peak was confirmed. This is now interpreted as a parcel of hot shock heated gas (KT~20keV) produced in a recent merger. In the high redshift systems MACS0744 and CL1226, pressure substructure was identified and is believed to be associated with merger activity. Both systems contain peaks in dark matter revealed by gravitational lensing which are not associated with baryonic

emission, supportive of a scenario in which an infalling cluster has passed through a main cluster being stripped of its baryons. In MACS0744, the SZE and X-ray morphology is suggestive of a shock wave propagating through the ICM. By fitting the Rankine Hugoniot jump conditions in a simultaneous SZE/X-ray analysis, the likelihood of this interpretation is explored. The system is well described by a mildly supersonic shock wave propagating with a Mach number of ~1.2.

Degree Type
Dissertation

Degree Name
Doctor of Philosophy (PhD)

Graduate Group
Physics & Astronomy

First Advisor
Mark Devlin

Keywords
Sunyaev Zeldovich effect, Bolometers, Cosmology, Radio Telescopes

Subject Categories
External Galaxies | Instrumentation

THE MULTIPLEXED SQUID TES ARRAY AT NINETY GIGAHERTZ (MUSTANG)

Phillip M. Korngut

A DISSERTATION

in

Physics and Astronomy

Presented to the Faculties of the University of Pennsylvania

in Partial Fulfillment of the Requirements for the degree of Doctor of Philosophy

2011

Supervisor of Dissertation:

_____

Mark Devlin, Professor, Astrophysics Experiment

Graduate Group Chairperson:

_____

A. T. Charlie Johnson, Professor, Condensed Matter Experiment

Dissertation Committee:

Masao Sako, Assistant Professor, Astrophysics

Gary Bernstein, Professor, Astrophysics

Bhuvnesh Jain, Professor, Astrophysics Theory

Josh Klein, Associate Professor, Experimental Particle Physics

Acknowledgements

Throughout my tenure as a graduate researcher at UPENN, I have had the privilege of getting to work with a wide range of scientists at a variety of institutions. The work presented in this thesis would not have been possible without their help and I am in their debt.

My advisor, Mark Devlin, has consistently provided wise and meaningful guidance. His knowledge of the field and keen insight to the way in which things fit into a larger picture have taught me valuable lessons about the process of science. He works harder than anyone else I know, tirelessly proposing to secure funding and look out for the future of those around him. His extensive success in the field is clearly well earned. I am grateful for all the opportunity he has provided me with. It has had profound positive influence on the path my career has taken.

Much of my effort in the proverbial trenches at the front lines of MUSTANG research was directly guided by two mentors; Simon Dicker and Brian Mason. My knowledge of data analysis, cryogenics, optics and all aspects of telescope operation is a direct consequence of working with them. They have always been more than willing to work closely with me through the gritty details of the experiment and have proved to be excellent companions through the long months spent at Green Bank.

The functionality of MUSTANG would not have been possible without a tremendous amount of support from the staff at NRAO. I've always had help from the receiver folks like Steve White, Mike Stennes and Dave Woody. The cryo guys, Bob Simon and Kenny Lehman, were always there to troubleshoot helium related issues and to provide any fitting or pipes we needed. Software people like Melinda Mello, Mark Whitehead and Ray Creager have ensured a fantastic control interface and were quick with fixing any obscure bug I came across. The GBT operators, Greg Monk, Donna Stricklin and Barry Sharp have provided lots of late night assistance while running observations and I thank them for their attentiveness.

I have learned a tremendous amount about TES detectors from working with the teams at NASA GSFC and NIST. Dominic Benford, Johannes Staghun, Jay Chervenak, Tali Figueroa, Harvey Moseley, Joel Ullom and Galen O'Neil have taught me the intricacies of detector operation and optimization.

I'd also like to thank several senior scientists who have helped me along the way including Masao Sako, Craig Sarazin, Bill Cotton and James Aguirre. Post-docs like Erik Reese and Tony Mroczkowski helped me work through difficult problems. Fellow graduate students and staff who worked in the Experimental Cosmology lab such as Marie Rex, Dan Swetz, Chris Semich, Matt Truch, Bob Thornton, Danica Marsden, Elio Angile, Ben Schmidt, Alex Young, Jeff Klein, Fritz Stabeneau, Kim Scott and Roxana Lupu have also made for a pleasant and productive work environment.

There is no way I could have made it through classes without the help of my friends and classmates, in particular Ravi Gupta, Jon McDonald, and Jon Fischer. They made working through difficult problem sets feasible and at times, even fun.

My parents, Robert and Heidi Korngut, have always encouraged my scientific endeavors and they presented me with the opportunities to pursue them. I am forever grateful for their support. Finally, I would like to thank Rebekah Midberry, for her love and understanding throughout the PhD process.

ABSTRACT

THE MULTIPLEXED SQUID TES ARRAY AT NINETY GIGAHERTZ (MUSTANG)

Phillip M. Korngut

Mark Devlin

The Multiplexed SQUID/TES Array at Ninety Gigahertz (MUSTANG) is a bolometric continuum imaging camera designed to operate at the Gregorian focus of the 100 m Green Bank Telescope (GBT) in Pocahontas county, West Virginia. The combination of the GBT's large collecting area and the 8×8 array of transition edge sensors at the heart of MUSTANG allows for deep imaging at $10''$ resolution at 90 GHz. The MUSTANG receiver is now a facility instrument of the National Radio Astronomy Observatory available to the general astronomical community.

The 3.3 mm continuum passband is useful to access a large range of Galactic and extra-Galactic astrophysics. Sources with synchrotron, free-free and thermal blackbody emission can be detected at 3.3 mm. Of particular interest is the Sunyaev Zel'dovich effect in clusters of galaxies, which arises from the inverse Compton scattering of CMB photons off hot electrons in the intra-cluster medium. In the MUSTANG band, the effect is observationally manifested as an artificial decrement in power on the sky in the direction of the cluster. There have been many experiments in the past two decades dedicated to measurements of the SZE, however, nearly all of them were accomplished with angular resolution larger than $\sim 1'$. The massive primary of the GBT enables measurements of the SZE on $10''$ scales. This provides a new technique to map pressure substructure in the plasma atmospheres of merging clusters of galaxies. By analyzing MUSTANG data along side X-ray data, spatially resolved measurements of the temperature, density and

pressure of the ICM can be performed which can be used to infer the physics governing major mergers.

This thesis details the design, commissioning and operation of the various components which comprise the MUSTANG receiver. This includes the sub-kelvin cryogenic cooling, the time domain multiplexed readout electronics and the array of transition edge sensor bolometers. Laboratory characterization of the detector array is thoroughly described, including the measurements of the transition temperatures, thermal conductance, noise properties and time constants.

Bolometric cameras measure celestial radiation as time ordered data. To reliably produce images from traces in the time domain, care must be taken to modulate the signal in an optimized fashion during observations. Once the data are taken, algorithms must be developed to isolate the signal of interest from the foregrounds produced by atmospheric emission. This thesis presents the techniques developed to scan, calibrate, filter and produce images from time ordered data taken with MUSTANG and the GBT.

From the Fall of 2006 to the winter of 2010, the MUSTANG receiver was commissioned on the GBT and used for a range of astrophysical measurements. The commissioning process and early science results are given in this thesis. This includes the modifications made to the instrument which have resulted in dramatically enhanced sensitivity as well as the images produced from bright extended millimeter sources such as high mass star forming regions, active galactic nuclei and supernova remnants.

This thesis presents a sample of merging clusters of galaxies imaged through their Sunyaev Zel'dovich signatures at high angular resolution. In the massive cluster RXJ1347, a previously reported pressure enhancement to the south east of the cluster peak was confirmed. This is now interpreted as a parcel of hot shock heated gas ($kT_e > 20$ keV) produced in a recent merger. In the high redshift systems MACS0744 and CL1226, pressure substructure was identified and is believed to be associated with merger activity. Both systems contain peaks in dark matter revealed by gravitational lensing which are not associated with baryonic emission, supportive of a scenario in which an infalling cluster has passed through a main cluster being stripped of its baryons. In MACS0744, the SZE and X-ray morphology is suggestive of a shock wave propagating through the ICM. By fitting the Rankine Hugoniot jump conditions in a simultaneous SZE/X-ray analysis, the likelihood of this interpretation is explored. The system is well described by a mildly supersonic shock wave propagating with a Mach number of $\sim$1.2.

Contents

List of Tables

List of Figures

Chapter 1

Introduction

1.1 The 3.3 mm Continuum Universe

The continuum band centered around the atmospheric transmission window at 3.3 mm (90 GHz) is a rich region of the electromagnetic spectrum with applications to a wide range of astrophysical phenomena, both in our Galaxy and beyond. There are three basic emission mechanisms which dominate the millimeter sky; free-free, synchrotron, and thermal blackbody.

1.1.1 Free-Free

Young O and B stars are substantially hotter then our Sun and subsequently emit strongly in the ultra-violet (UV). These UV photons can ionize the surrounding inter-stellar medium producing vast HII regions with temperatures typically on the order of $\sim 10,000$ K. The free electrons in these plasmas scatter off one another, producing radiation with every charge accelerated by an interaction. The electrons remain unbound after the interaction and thus are dubbed free-free. This process produces a continuous spectrum of radiation which typically spans the radio and continues into the millimeter. It is also known as thermal bremsstrahlung radiation.

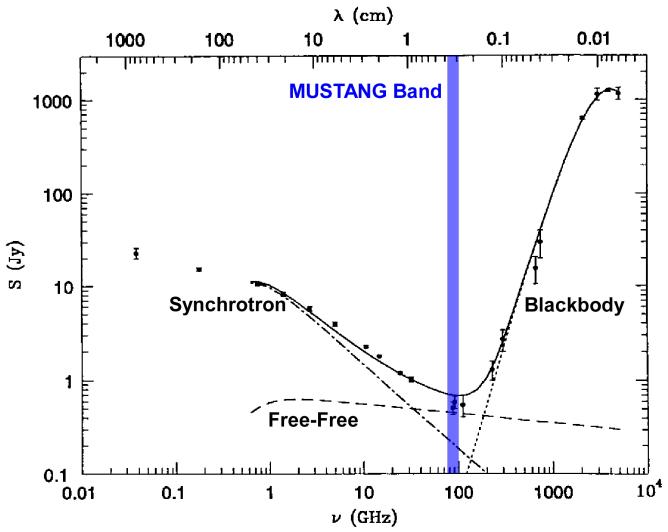

Figure 1.1 - Spectral energy distribution of M82, a nearby starburst galaxy, from the radio to the submm. Continuum radiation in the 3.3 mm MUSTANG band has components arising from free-free, synchrotron, and thermal dust emission. Figure adapted from ESSENTIAL RADIO ASTRONOMY by J. J. Condon and S. M. Ransom (NRAO).

1.1.2 Synchrotron

When charged particles spiral along magnetic field lines they emit synchrotron radiation. The frequency of the photons emitted depends on the energy of the relativistic electron population. Synchrotron emission is essential to the study of objects such as active galactic nuclei (AGN), supernova remnants and planetary nebulae. Typical synchrotron spectral energy distributions are well characterized empirically by a falling power law in the radio which peaks below 1 GHz. Therefore, adding a 90 GHz flux measurement to a dataset of lower frequency radio measurements allows for a more sensitive determination of the energy population of the relativistic electrons.

1.1.3 Blackbody

The motion of charged particles within an optically thick body in thermal equilibrium gives rise to blackbody radiation. The characteristic blackbody spectrum of intensity, B_ν,

as a function of frequency, ν, depends strongly on an object's temperature, T and is given by

$$B_\nu(T) = 2\frac{\nu^2}{c^2}\frac{h\nu}{e^{\frac{h\nu}{kT}} - 1}, \tag{1.1}$$

where h is Planck's constant, c is the speed of light and k is Boltzmann's constant. When a blackbody is on the order of 6000 K as is our sun, its spectrum peaks in the optical. However, an object which is much colder, on the order of 10 K, will emit radiation which peaks at longer wavelengths, in the submillimeter. Cold celestial objects like molecular clouds in star forming regions, debris disks around young stars and dusty high redshift star forming galaxies have significant blackbody emission at 3.3 mm.

The diversity of the 3.3 mm continuum band is embodied by the spectral energy distribution shown in Figure 1.1. M82 is a nearby starburst galaxy seen close to edge on. There are many star formation processes ongoing which give rise to all three of the emission mechanisms discussed above. The MUSTANG bandpass, is located at the nexus of the three spectra. A high resolution camera at 3.3 mm provides new access to all of these phenomena.

1.2 The Sunyaev Zel'dovich Effect

1.2.1 The CMB

The cosmic microwave background (CMB) is a uniform radiation field found in all directions on the sky. It's spectral characteristics are spectacularly well described by a blackbody emitter (Equation 1.1) with a temperature of 2.725 K [Mather et al., 1990] and therefore has a spectrum which peaks at ~ 1 mm. This signal arises from relic radiation in the early Universe, at a redshift of approximately 1100. It is the signature of the epoch of recombination, when the ionized early Universe just several hundred thousand years after

the Big bang cooled enough to become neutral and optically thin.

The discovery and subsequent exploration of the CMB has provided cosmologists with an immense pool of data and subsequent insight to the history and nature of the Universe. It's exploration has pioneered experiments on many platforms. Missions to explore this signal have been built on aircrafts[Smoot et al., 1977], satellites[Mather et al., 1990][Page et al., 2003], sub-orbital balloons[Netterfield et al., 2002][Oxley et al., 2004], and ground based telescopes in exotic locations such as the South Pole[Takahashi et al., 2010] and the Atacama desert[Pearson et al., 2003]. The profound and precise information provided by the CMB has given cosmologists the most accurate measurements of the age, energy content, and curvature of the Universe and has resulted in the award of two Nobel prizes.

1.2.2 The Intra Cluster Medium

The early 1970s marked the birth of space based X-ray astronomy with the launch of the *Uhuru* satellite. The *Uhuru* data revealed mysterious extended ($\sim 0.5^{\circ}$) sources in the 2 keV to 8 keV band which appeared to be associated with nearby rich clusters of galaxies like Virgo, Coma and Perseus [Gursky et al., 1972]. These detections prompted investigations targeting other known galaxy clusters and it was soon confirmed that nearly all rich clusters contained extended X-ray sources.

With masses ranging up to the order of 10^{15} $M_{\odot}$, clusters of galaxies are the largest gravitationally bound objects in the Universe. When diffuse gas (predominately hydrogen) which forms an intra-cluster medium (ICM) is trapped in the immense gravitational potential of a cluster, it is heated and ionized, reaching energies on the order of ~ 10 keV per electron. In undisturbed clusters, this medium is in hydrostatic equilibrium and the thermal energy associated with the gas is consistent with that expected from virilization. The charged particles in the plasma interact and scatter off each other, producing bremsstrahlung radiation, which at these energies emits a continuous spectrum of X-ray photons.

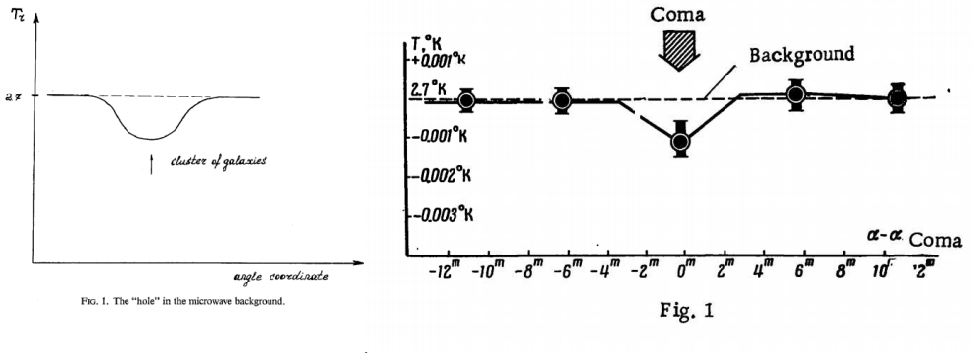

FIG. 1. The "hole" in the microwave background.

Fig. 1

Figure 1.2 - Left: The Sunyaev-Zel'dovich effect in clusters of galaxies is observationally manifested at frequencies <218 GHz as an artificial decrement in the cosmic microwave background. This hand drawn figure originally appeared in Sunyaev and Zeldovich [1972] and poses the theoretical prediction for observations in the radio in the direction of a cluster. Right: First claimed detection of the SZE made at 4 cm with the Pulkovko radio telescope in Soviet Russia. This detection in the direction of the Coma cluster appeared in Pariiskii [1972].

1.2.3 Interaction between the CMB and the ICM

The first observational discovery of the CMB was reported in 1965 by Penzias and Wilson [1965] who measured an excess antenna temperature of ~ 3.5 K at all locations in the sky at 4080 Mc/s (Mega cycles per second. The unit "Hz" was not commonly used yet). In the following few years it was confirmed in the radio at multiple frequencies and by the early 1970s the radiation was understood to be well described by a blackbody around 2.7 K. During this period, at the height of the cold war, two Soviet theoretical cosmologists, Sunyaev and Zel'dovich, had been investigating the observational effects that Compton scattering processes in hot electron baths might have on this relic radiation [Zeldovich and Sunyaev, 1969].

Motivated by the recent discovery of X-ray emission in clusters of galaxies [Gursky et al., 1972], Sunyaev and Zel'dovich, calculated the observational signature imparted by inverse Compton scattering of CMB photons in the hot ICM. They found that the transfer of energy from the electrons to the photons produced a net blueshift of the CMB's Planck spectrum ($B_\nu(T = 2.725K)$) in the direction of the cluster. Therefore, if the CMB field

were to be mapped in the radio around a massive cluster, a cooler temperature should be observed and the ICM will imprint a "hole" in the microwave background. A hand drawn illustration of this effect which first appeared in Sunyaev and Zeldovich [1972] is given in Figure 1.2. The first detection, made towards the Coma cluster with the Polkovko radio telescope, was claimed shortly after the publication of the proposed signature and appeared in Pariiskii [1972]. When writing their seminal paper [Sunyaev and Zeldovich, 1972], the authors were aware of the detection and cite Pariiskii [1972] as "in press". It is interesting to note that this detection paper, the first measurement of Compton scattering in the ICM, was published in the Journal of Soviet astronomy, and has only received 12 citations to date[1]. The phenomenon of Compton scattering of the CMB in the ICM has been named after its proposers and is referenced in the literature as the Sunyaev Zel'dovich effect (SZE).

The importance of this new tracer of the ICM, and thus large scale structure in the Universe was immediately recognized. In the decades since its proposal and discovery, an entire field of observational astrophysics has been developed which seeks to apply the effect to a wide range of astrophysical measurements.

1.2.4 Characteristics of the SZE

Inverse Compton scattering of CMB photons off hot electrons in the ICM shifts the 2.725 K blackbody spectrum to higher energies. This spectral effect as calculated for a large cluster is shown in Figure 1.3. The magnitude of the signal in this plot is $\sim 1,000\times$ larger than that for even the most massive clusters in the Universe. This is shown for illustration purposes, because the amplitude of the effect in actual clusters is exceedingly small, with only $\sim 1\%$ of photons undergoing the scattering.

The Intensity of the SZE signal, $\triangle I_{SZE}$, seen from a given cluster relative to the back-

[1]Citations archived by the NASA astrophysics database system as of 3/17/2011

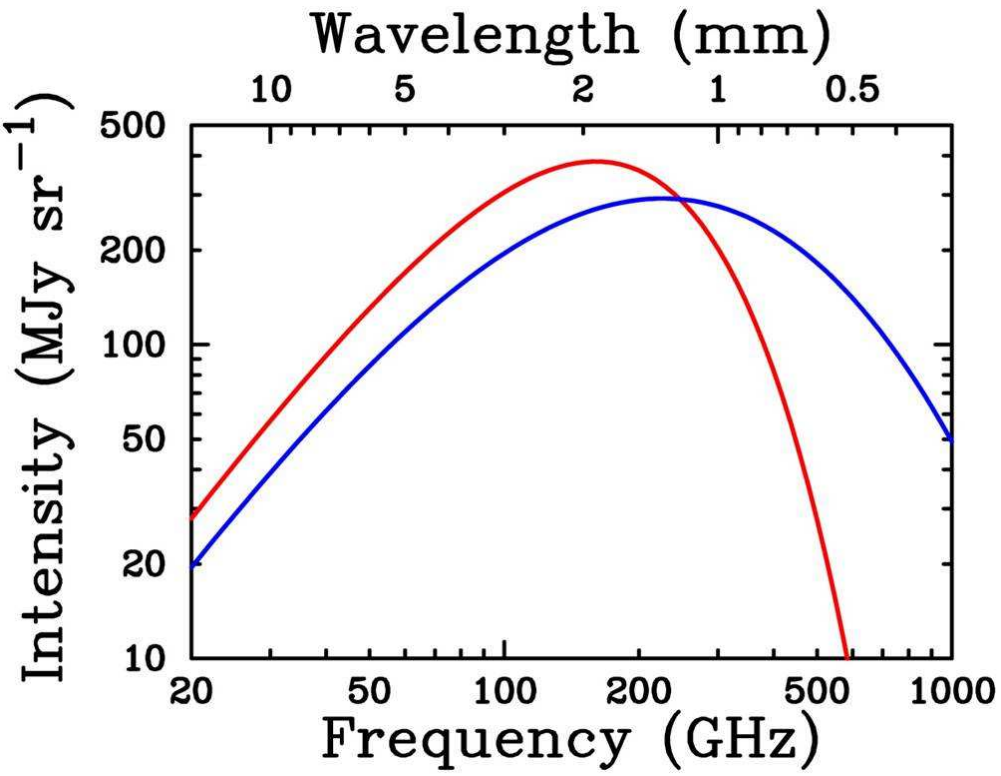

Figure 1.3 - CMB spectral energy distribution. Red shows the spectrum of the intrinsic thermal relic radiation, a 2.725 K Planckian distribution. Blue shows the red spectrum after undergoing inverse Compton scattering processes while passing through the hot ionized intra-cluster medium of a fictional cluster $\sim 1,000\times$ more massive than typical observed clusters. This large mass is used to better illustrate what is normally a very small effect. Figure courtesy of Erik Reese.

ground CMB is expressed as

$$\triangle I_{SZE} = g(x) I_o y_C, \tag{1.2}$$

where the intensity normalization is

$$I_o = 2\frac{(kT_{CMB})^3}{(hc)^2}. \tag{1.3}$$

The frequency dependence of the effect is encapsulated in the function g(x), where

$$g(x) = \frac{x^4 e^x}{(e^x - 1)^2}\left(x\frac{e^x + 1}{e^x - 1} - 4\right)(1 + \delta), \tag{1.4}$$

and x is the reduced frequency, $x = h\nu/kT_{CMB}$. The parameter δ encapsulates the relativistic corrections to the thermal effect and is also a function of frequency [Carlstrom et al., 2002b].

The Compton y_C parameter is defined as the line of sight integral of the pressure, $P_e = n_e k T_e$, of the ICM and is given by

$$y_C = \int \sigma_T \frac{P_e}{m_e c^2} dl, \tag{1.5}$$

where, n_e is the electron density, σ_T is the Thomson cross section of the electron, T_e is the temperature of the plasma and m_e is the mass of the electron.

1.3 Applications of the SZE

Over the past two decades, measurements of the SZE in clusters of galaxies have been used to probe a wide range of cosmological and astrophysical questions. It has been used by dedicated surveys to search for clusters [e.g., Hincks et al., 2009, Vanderlinde et al., 2010, Menanteau et al., 2010, Marriage et al., 2010], combined with X-ray data to measure

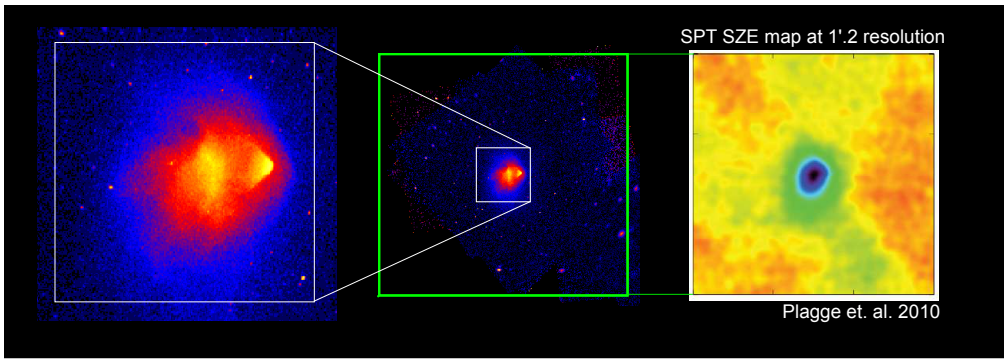

Figure 1.4 - Right: SZE image of the bullet cluster made with the South Pole Telescope at 1.′2 resolution reported by Plagge et al. [2010]. Center: *Chandra* image from 500 ks of exposure time on the same object. The green box corresponds to the field of view in the SZE image. Left: Zoomed in image of the *Chandra* result. The system is highly disturbed, multiply peaked, with a $\mathcal{M} \sim 3$ shock propagating [Markevitch and Vikhlinin, 2007]. Large beam SZE measurement is a powerful tool for detecting clusters in large surveys and fitting profiles to large cluster-centric radii, however all substructure on ~ 10 kpc scales will be missed entirely. High angular resolution SZE images are needed to directly map pressure substructure which complement the high quality X-ray observations.

the Hubble flow [e.g., Mason et al., 2001, Reese et al., 2002, Bonamente et al., 2006] and to derive physical cluster properties from radial profiles [e.g., LaRoque et al., 2003, Bonamente et al., 2006, Mroczkowski et al., 2009]. For reviews of the SZE and its applications, see Birkinshaw [1999] and Carlstrom et al. [2002b].

Measurements of the SZE at high angular resolution are difficult because of the large collecting areas required. Nearly all measurements currently in the literature have effective angular resolution larger than $\sim 1'$. These large angular scales (corresponding to ~ 365 kpc at $z = 0.5$) are useful for measuring cluster properties within large cluster-centric radii [e.g., Nord et al., 2009] but are unable to resolve cluster substructure within the ICM.

High-resolution X-ray imaging from *Chandra* and XMM *Newton* in the last decade opened a new window to cluster physics. Objects once thought to be spherically symmetric and relaxed have been shown to display evidence of interesting phenomena which provide insight to the complicated dynamics at play in these structures. Among these are shocks and cold-fronts induced by recent mergers [e.g., Markevitch and Vikhlinin, 2007], cavities

and heating caused by AGN interactions [e.g., McNamara et al., 2005] and sharp surface brightness edges caused by gas sloshing [e.g., ZuHone et al., 2009].

High-resolution images of the SZE in clusters provide a new tool which, when combined with X-ray measurements, can constrain complicated physics in galaxy clusters. This is particularly true of the high-redshift Universe as the X-ray surface brightness data (proportional to the product of the density squared and square root of temperature integrated along the line of sight) suffer from cosmological dimming. The X-ray also trace a fundamentally different observable. The intensity of bremsstrahlung radiation is proportional to the line of sight integral of density squared and is weakly dependent on temperature. Combining high resolution SZE with X-ray imaging and spectroscopy allows for a spatially resolved reconstruction of the pressure, temperature, and density morphologies in the ICM.

In the hierarchical scenario currently favored in standard cosmology, large scale structure evolved over time from initial conditions set forth by quantum fluctuations in the early Universe. This gave rise to the filamentary density distribution of the large scale structure of the Universe seen today. At the intersections of these filaments lie clusters. As cosmic time evolves, these clusters grow through mergers. The ICM which pervades this structure behaves like a fluid, and like any medium, waves propagate through it with a characteristic sound speed. When mergers occur, the infall velocities between subclusters can reach speeds of thousands of km/s, faster than the speed of sound [Sarazin, 2002]. When this occurs, supersonic shock waves are formed which obey a specific set of jump conditions which govern supersonic flow in all fluid dynamics (see Landau and Lifshitz [1959]). Shocks produce compression in the gas, and since the SZE intensity is directly proportional to the line of sight integrated pressure, shocks are manifested as localozed enhancements to the SZE. These shocks are observed in the X-ray as sharp surface brightness discontinuities [Markevitch and Vikhlinin, 2007].

A particularly striking example of a shock in a merging system is seen in the Bullet

cluster, which is propagating ∼3 times faster than the sound speed [Markevitch et al., 2002b]. The X-ray emission as imaged by *Chandra* in this cluster is shown in Figure 1.4. Also shown in this figure is the detection in SZE as measured by the South Pole telescope (SPT) [Plagge et al., 2010]. The SPT experiment was designed with a large field of view and the intention of mapping large swathes of sky to search for clusters through their SZE signature. By looking at this figure it is clear that the goal was accomplished and a very significant detection is seen in the direction of the bullet cluster. However, the morphology in this SZE image is entirely unresolved ($1\farcm2$ beam) and would be well approximated with spherical symmetry. From the *Chandra* data we know that this approximation is not valid in this object and a tremendous amount of information regarding the assembly dynamics of this system is lost. Adding SZE with angular resolution an order of magnitude higher than that of the SPT would allow for direct measurements of the pressure substructure in the ICM of merging systems, which, when combined with X-ray data provides the necessary information for detailed modeling of the fluid dynamics governing the system.

The potential of resolved SZE was first demonstrated by Komatsu et al. [2001], who used the Nobeyama 45m to image RXJ1347-1145, a massive X-ray luminous cluster previously thought to be relaxed and spherically symmetric [Schindler et al., 1997]. The asymmetry revealed by their work was the first indication that the system was disturbed, and it is now believed to have undergone a recent merger [Kitayama et al., 2004]. This object, and the physics inferred from the resolved SZE will be discussed in detail in Chapter 7.

This thesis presents measurements taken with the Multiplexed SQUID/TES Array at Ninety Gigahertz (MUSTANG) receiver on the 100 m Robert C. Byrd Green Bank Telescope (GBT). The large collecting area of the GBT combined with the focal plane array of bolometers make this system ideal for probing substructure in clusters through the SZE. The results are among the first sample of clusters to be imaged through the SZE at subarcminute scales.

1.4 MUSTANG

The 3.3 mm band is a technologically interesting electromagnetic regime, nestled between the radio and far infrared/submm, where both traditional radio heterodyne receiver systems and bolometric cameras with reimaging optics are deployed. Both have respective advantages. With a heterodyne system, the coherence of incident radiation is maintained. This makes traditional radio receivers excellent tools for spectroscopy and polarization studies. They also maintain the phase of the signal and can therefore be used in interferometry. However, they require sophisticated back-end correlators to process the data and are difficult to scale up to large arrays. They also have narrower bandpasses making continuum sensitivity limited.

Bolometric imagers have several favorable characteristics for continuum operation at 3.3 mm. The bandpass is defined by capacitive mesh filters in a tube of reimaging refractive optics, similar to what one might see in an optical camera. This makes a wide bandpass achievable (81-99 GHz), excellent for continuum sensitivity. The detectors are very scalable, and the readout can be multiplexed. This makes large format arrays feasible. Since the coherence of incident radiation is not maintained, data do not need to be sampled at RF frequencies, making data files of manageable size.

The MUSTANG instrument (originally called the Penn Array Receiver), was designed to provide broad-band, sensitive imaging on the Green Bank Telescope at 90 GHz. It was developed in collaboration with a number of institutions who provided the broad skill set necessary to produce this complicated instrument. The development was centered at the University of Pennsylvania, where the instrument was designed and integrated. NASA GSFC provided the array of transition edge sensor (TES) detectors and readout electronics. The SQUID amplifiers were fabricated by the quantum sensor group at NIST in Boulder, CO. NRAO provided support in software, operation and installation along with

the machining of the critical large scale components. The optical filters and IR blockers were provided by Cardiff University in the UK. This thesis details the design and implementation of the various systems required for MUSTANG operation.

Chapter 2

Instrument

2.1 The Green Bank Telescope

MUSTANG was designed to operate on the Robert C. Byrd Green Bank Telescope (GBT), located in a remote valley in Pocahontas County, West Virginia. The telescope is a facility instrument operated by the National Radio Astronomy Observatory (NRAO) and is available to the general astronomical community through a science merit based proposal system. The telescope operates over a broad range of bandwidth, from ∼300 MHz, all the way to MUSTANG's band centered at 90 GHz.

The primary aperture of the GBT is 100 m in diameter and is completely unblocked by the support struts common in traditional radio telescope architecture. This is enabled by an off-axis optical design in which the primary reflector is a 100 m section of a 300 m parent paraboloid. The free-standing feedarm supports a secondary mirror and a receiver cabin at the Gregorian focus.

To enable such a wide frequency band, many receivers are needed. The low frequency receivers which operate below 1 GHz are located at the primary focus of the telescope on a retractable boom which sits in front of the 8 m concave parabolic secondary mirror. The majority of the GBT's receivers, including MUSTANG, are located at the Gregorian focus

of the telescope. All of the Gregorian receivers are mounted on a rotating turret in the receiver cabin. To change frequency band, the remotely operated turret can be rotated such that the desired instrument is located in the focus position.

The surface of the primary is composed of 2004 panels with an actuator located at the intersection of every four. This active surface is essential to maintain a precise alignment of the panels in the shape of the specified paraboloid. MUSTANG operates at a wavelength more four orders of magnitude smaller than the diameter of the primary. This puts severe requirements on the tolerable level of surface fluctuations. Through an extensive effort of phase coherent holography, the precision telescope control system team at NRAO has improved the accuracy of the surface to an RMS of $\sim$220 μm. This produces a main beam efficiency at 90 GHz of 35%, suitable for MUSTANG operation. A photograph of the GBT and its various components is given in Figure 2.1. A detailed description of the design and capabilities of the GBT can be found in Jewell and Prestage [2004].

2.2 Cryostat

In order to operate MUSTANG's superconducting detectors, and minimize instrumental optical loading, it is essential to cryogenically cool the receiver close to absolute zero. The MUSTANG cryostat, outlined in Figure 2.2 houses the core elements of the receiver. The cryostat is organized in concentric cylinders of decreasing temperature to regulate the radiative load on the cooler stages. The outermost stage is a room temperature vacuum can and lid. The lid is designed to mount directly to the GBT turret in a 38.0 in aperture. This lid contains the hermetically sealed 50 pin D connector feedthroughs for cryogenic housekeeping cables and the vacuum window opening to the optics. A toroidal RFI and weather shield ("the donut") mounts to the room temperature lid and sits on the roof of the receiver cabin. This ensures that low frequency radiation from MUSTANG's readout

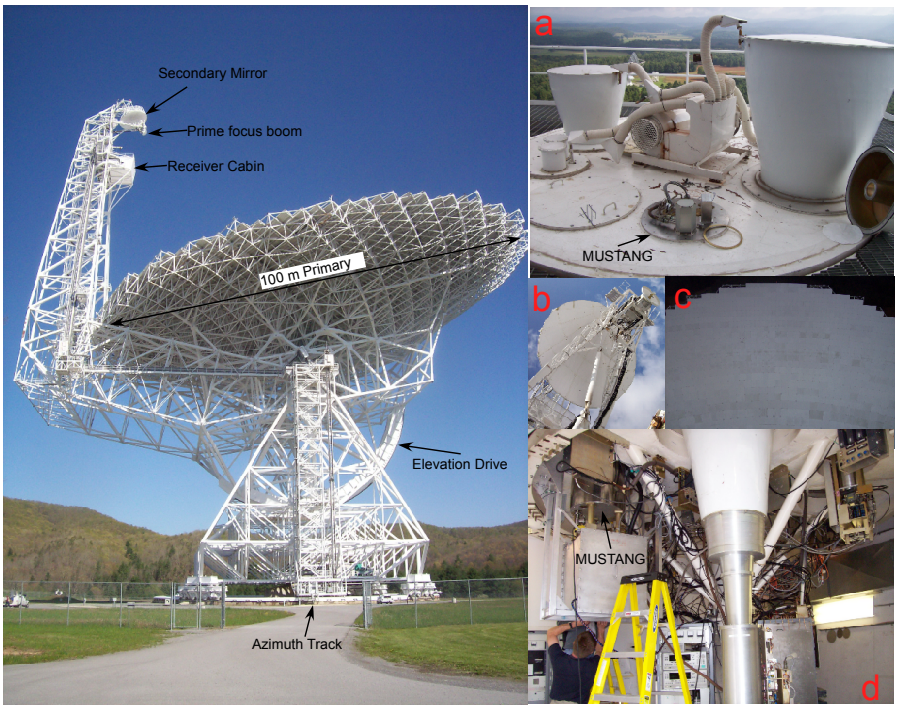

Figure 2.1 - Left: Photograph of the 100 m Green Bank telescope with various features labeled. *a* : The roof of the receiver cabin. Six receivers are installed at the Gregorian focus on a rotating turret. MUSTANG is pictured without its weather and RFI shield in the center bottom of the photo. *b* : Photograph taken from the roof of the receiver cabin looking up at the secondary mirror. In this case the prime focus boom is extended. *c* : The active surface of the primary mirror as seen from above. *d* : The inside of the receiver cabin looking at the turret. Simon Dicker is pictured standing under the MUSTANG electronics crate.

electronics does not contaminate other GBT receivers. It also prevents rain or snow from damaging the delicate components.

A 40 K base-plate and radiation shield provides another layer of heat-sinking and load control. This stage contains several optical elements including the first band-defining filter and lens. All thermometry cables are heat-sunk at this stage as well to reduce the parasitic load on colder stages introduced by conduction along the wires.

Inside the 40 K assembly is the 3 K stage and radiation shield. The baseplate at 3 K houses the third stage amplifiers, the Lyot stop, several reimaging optics and the cold address driver used in multiplexing. This stage also houses and pre-cools two sorption fridges

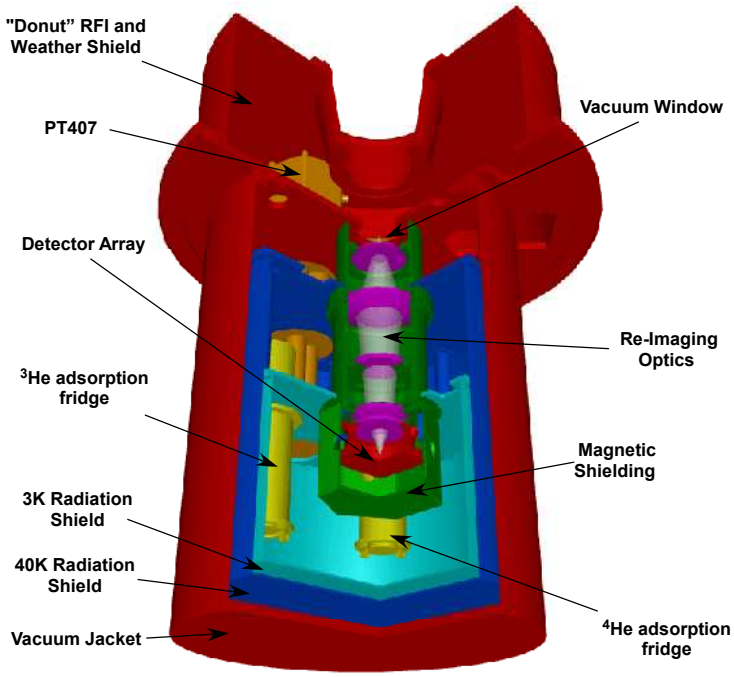

Figure 2.2 - Layout of the MUSTANG cryostat with various features annotated.

used to acheive the final stages of cooling. The sub-Kelvin cryogenics are described in Section 2.2.2. Inside a magnetic shield at the base of the optics tube lies the 300 mK assembly. To thermally isolate the detectors from the 3 K stage and maintain the appropriate location in the optical path, a Kevlar suspension system is implemented. Kevlar is an ideal material as it is durable with a small diameter and is a poor thermal conductor [Roach, 1992]. A photograph of the detector mount and suspension system is given in Figure 2.4.

2.2.1 Operating the Pulse Tube

A commercially obtained, two stage, Cryomech[1] pulse tube (PT) serves as the primary cooler on MUSTANG. Driven by a helium compressor located at the base of the telescope, it is capable of providing 0.7 W of cooling at 4.2 K and 25 W at 55K. Operating this device on the GBT poses several challenges. The first arises from the large distance between the

[1]PT-407 model from Cryomech Inc. See www.cryomech.com for more details.

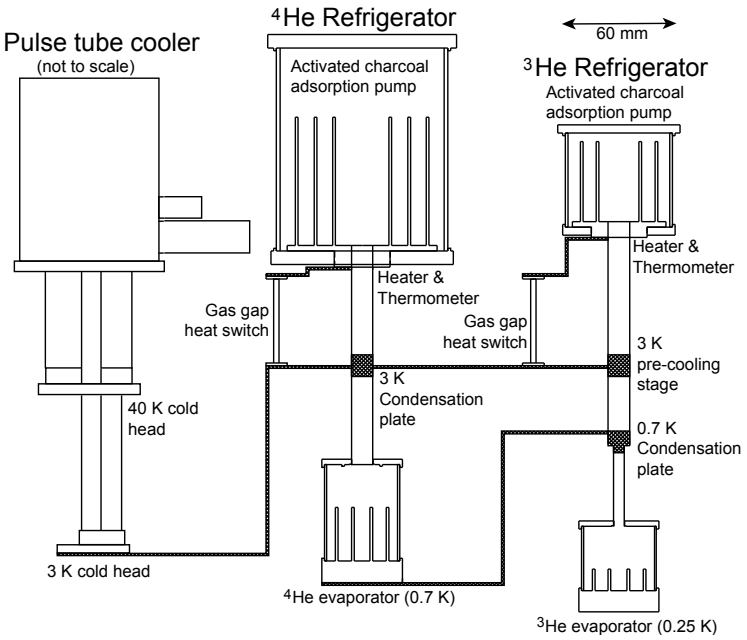

Figure 2.3 - MUSTANG's multi-stage cryogenic system. Initial cooling is provided by a Cryomech PT407 Pulse Tube cooler which reaches a baseplate temperature of 3 K. A ^{4}He adsorption refrigerator cools to 0.7 K and a ^{3}He adsorption refrigerator cools the final stage to < 300 mK where the detectors operate. Figure from Devlin et al. [2004].

compressor and cold head, with the compressor at the base of the telescope and the receiver in the Gregorian focus, 420 ft above the ground. Approximately 1000 ft of lines are needed to route the compressed helium up the telescope. The majority of this is in the form of rigid stainless steel helium pipes tig welded together which are fixed to the structure. Flexible hoses are needed in regions which require motion relative to the azimuth track, such as the elevation bearing and the rotating turret in the receiver cabin. At these locations the flexible helium lines are routed through a wrap to avoid over-stressing the pipes.

The performance of the PT depends on its orientation, degrading as it is tipped further from the vertical axis. The off-axis optical design of the GBT are configured such that when the receiver cabin is vertical, the telescope is pointed at 77 degrees elevation. While the first stage will slowly warm up as the elevation is decreased, second stage cooling is more or less stable until the telescope is pointed below 25 degrees. For MUSTANG observations, this is

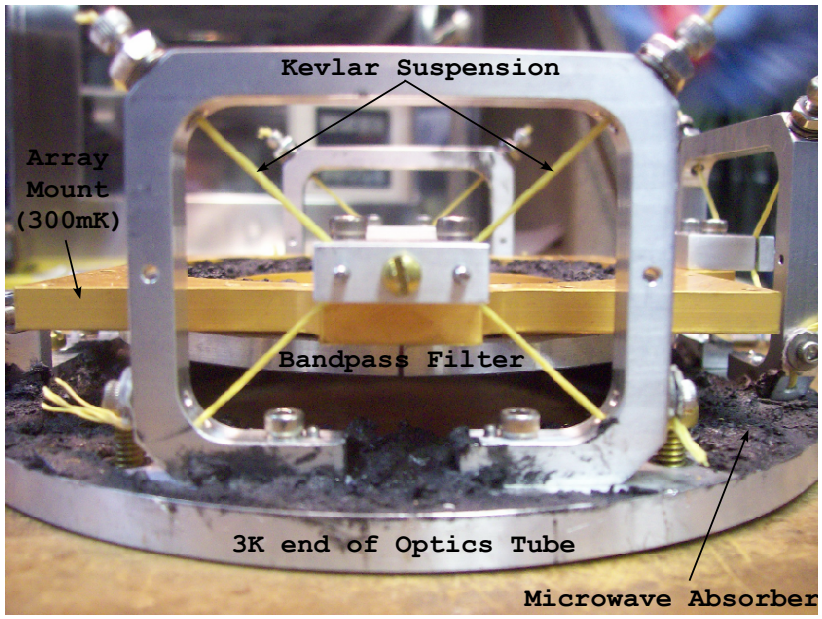

Figure 2.4 - Photograph of the 300 mK array mount on Kevlar suspension. The assembly is pictured here outside of the cryostat on a lab bench with the array removed.

sufficient, as the atmosphere is much more optically thick at low elevations. However, the GBT is used frequently at low frequencies where the atmosphere is always optically thin. These observers often track low declination sources which causes extreme warming of the PT. During and after heavy snowfall, the telescope is tipped over to 5 degrees elevation to dump the snow off the primary. Scheduling MUSTANG observations must account for recovery from low elevation to avoid missed observations due to warm cryogenics.

2.2.2 Sub-Kelvin Cooling

The second stage of the PT reaches a base temperature of $\sim$ 3 K under the loading conditions present in the MUSTANG cryostat. This is used to pre-cool a custom built closed-cycle system capable of providing the additional cooling below 300 mK that is required to operate the superconducting detectors and amplifiers. This system consists of two helium sorption fridges, one containing ^{4}He and the other ^{3}He. Activated charcoal inside the fridges pump on the reservoirs of liquid helium, reducing the temperature of

the boiling point. The thermal conductance between the charcoal and PT is regulated by gas gap heat switches commercially obtained from Chase Cryogenics [2]. The design of this system is outlined schematically in Figure 2.3 and described in detail in Devlin et al. [2004].

The ^{4}He fridge is capable of 10 mW of cooling at 1 K and the ^{3}He can cool 100 μW at 300 mK. However, the cooling is not continuous. When all of the helium has been adsorbed by the charcoal, the fridges need to be cycled by expelling and re-condensing the helium.

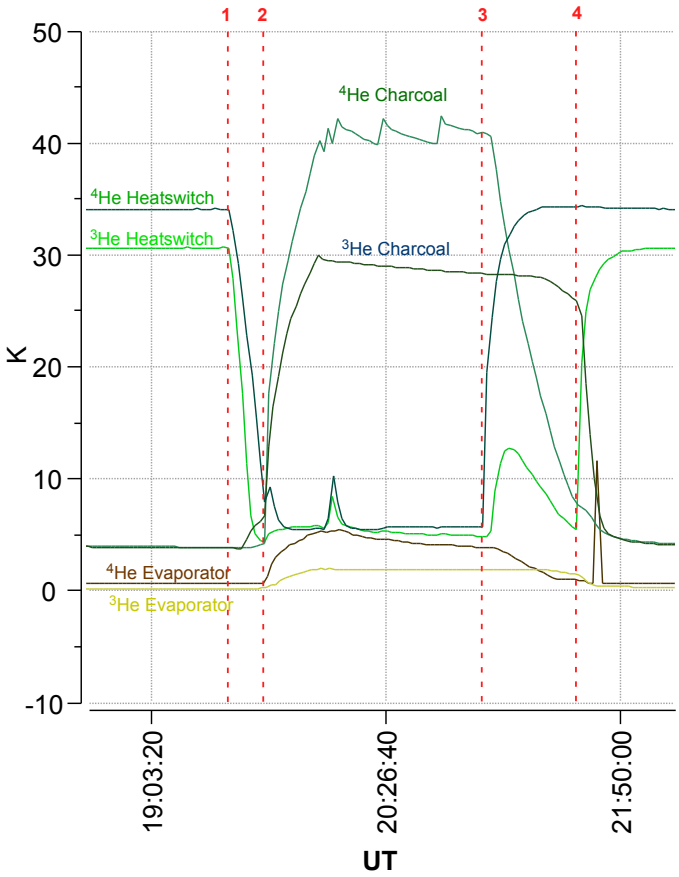

Figure 2.5 - Temperatures of several cryogenic components during a cycle while on the telescope. The enumerated red lines correspond to active configuration changes and are described in the text. The temperature spike between steps 2 and 3 was produced by the PT second stage warming when the telescope was briefly tipped to 5 degrees elevation. The apparant spike in the ^{4}He evaporator temperature after step 4 is an artifact produced when the calibration curve of the thermometer changed ranges.

The process of refrigerator cycling has been automated and is performed daily at a

[2]For detailed information on the heat switches see http://www.chasecryogenics.com/

fixed time during normal telescope operations. There are currently four versions of the autocycle optimized for different cryogenic scenarios; cooldown, normal, quick and custom. The normal cycle is the default and is most often used. It takes ∼2 hours to complete and will provide ∼20 hours of cooling with the ^{4}He fridge. The quick cycle and more aggressively the custom cycle take less time but will also provide shorter hold times. These are useful if the receiver has been warmed up by another observer looking at low elevation and MUSTANG observations are scheduled without enough time to perform a normal cycle. Since all MUSTANG observations are conducted at night, ^{3}He hold times of ∼12 hours are sufficient for the longest observing sessions, easily accommodated by the quick and custom cycles. The hold time of the ^{4}He fridge is substantially less than the ^{3}He. It is possible to observe with an empty ^{4}He fridge but the loading on the array will be greater and it will run at a higher temperature. This places the bath temperature of the array closer to the transition temperatures of the detectors and reduces the margin between the cooling power of the bath and saturation.

The autocycle algorithm is outlined below with the parameter values given in table 2.1. The cryogenic temperatures during a cycle with the configuration changes labeled is shown in Figure 2.5.

1. The heat applied to the gas gap heatswitches during cold operation is removed. This thermally isolates the charcoal from the 3 K base-plate. When the heatswitches cool below 10 K they are determined to be sufficiently off and the charcoal can be heated.

2. Power is applied to the heaters on the charcoal in both fridges. This expels the helium from the porous charcoal and releases it into the main cavity of each fridge. Once the ^{4}He and ^{3}He charcoals reach set-points a and c respectively, the power is removed from the heaters. During this phase, the ^{4}He gas is condensed into liquid. The charcoal temperatures are monitored and if they cool below set-points b and d,

Table 2.1. Cryogenic Autocycle Set Parameters

Parameter	Abbreviation	Cooldown	Normal	Quick	Custom
^{4}He Charcoal high	(a)	50 K	45 K	40 K	35 K
^{4}He Charcoal low	(b)	45 K	40 K	35 K	30 K
^{3}He Charcoal high	(c)	50 K	40 K	30 K	27 K
^{3}He Charcoal low	(d)	50 K	30 K	25 K	23 K
^{4}He evaporator	(e)	3.95 K	3.95 K	4.3 K	4.15 K
^{3}He evaporator	(f)	1.5 K	1.5 K	1.8 K	1.8 K

Note. — Trigger parameters used in the several configurations of automated cryogenic cycles.

the power to the charcoal heaters is re-applied.

3. When the ^{4}He evaporator has cooled below set point e, sufficient helium has liquefied on the condenser plate to begin pumping. Heat is applied to the ^{4}He heatswitch. This thermally connects the charcoal to the second stage of the PT and it cools, adsorbing helium gas and reducing the pressure in the chamber. The boiling point of the helium is reduced and it cools through the super-fluid transition point.

4. With the ^{4}He fridge now cooling the condenser plate in the ^{3}He fridge, ^{3}He begins to liquefy. Once the evaporator plate cools below set-point f, the ^{3}He heat switch is activated, cooling the charcoal and pumping on the gas. This produces a final base temperature below 300 mK, a suitable operating temperature for the detector array.

2.2.3 Reimaging Optics

The MUSTANG receiver has a series of reimaging optics designed to produce high fidelity focused imaging across the focal plane array. The optical chain begins with a Mylar vacuum window located on the lid of the cryostat at the Gregorian focus of the GBT. To

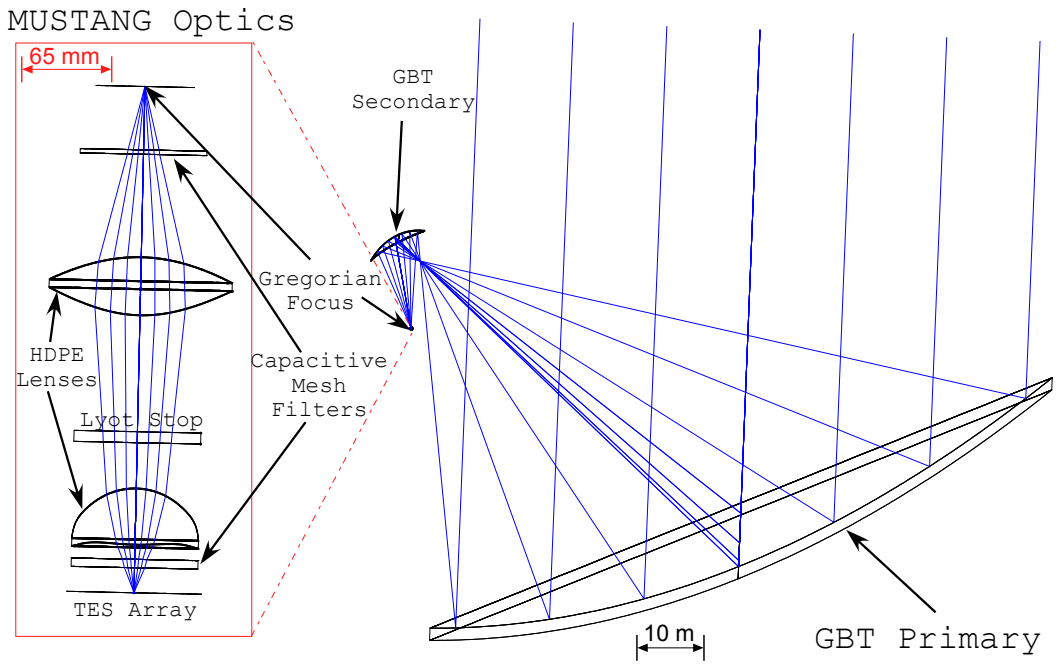

Figure 2.6 - Ray tracing through the GBT and MUSTANG optics. All optical components in the red inset are located inside the cryostat. The GBT off axis optical design brings the rays to a Gregorian focus. Inside the cryostat, the rays are reimaged using two high density polyethylene (HDPE) lenses. The bandpass is defined by two capacitive mesh filters in the optical path. The illumination of the primary is limited to a 45 m radius by the cold Lyot stop. Ray tracing for this figure was done by Simon Dicker.

control cryogenic loading, a series of three infrared blockers are stationed throughout the optics tube which reject out of band radiation. A high density polyethylene lens mounted on the 40 K cryogenic stage is used to form an image of the GBT primary. A Lyot stop is placed at this exit pupil to restrict the illumination of the dish to the central 90 m diameter. Also located at the 3 K Lyot stop is an inverse bolometer, an easily controllable millimeter wavelength emitter used for detector flat-fielding. It is placed at the Lyot stop so it uniformly illuminates the array. In this thesis this source is referred to as CAL. A second HDPE lens produces the final focus at the detector array. A ray tracing diagram for the GBT and reimaging optics is given in Figure 2.6.

The pixels are designed to be spaced by $5''$ or 0.65 $f\lambda$. This is slightly below Nyquist sampling. This does not pose a problem as the array pointing is constantly modulated on the sky during observations. Measurements of the beam offsets taken through the GBT and all the reimaging optics are shown in Figure 2.7. The evenly spaced rectangular pattern shows excellent agreement with prediction indicating the optics fall well within the design specifications.

To reduce reflections, the HDPE lenses have $\frac{\lambda}{4}$ grooves machined into their surfaces. The MUSTANG bandpass of 81 to 99 GHz is defined by two capacitive mesh filters produced by collaborators at Cardiff University. To control stray light, the internal walls of the optics tube are coated with efficient black-body absorber.

2.3 Detectors

2.3.1 Bolometers

At the core of MUSTANG is an 8×8 array of transition edge sensor (TES) bolometers. Generally, a bolometer consists of a photon absorbing membrane weakly connected via some thermal conductance, G, to a bath. On the membrane sits a sensitive thermistor.

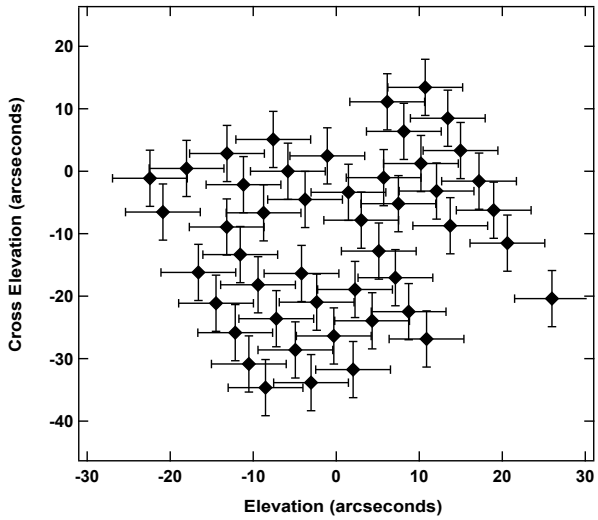

Figure 2.7 - Measured beam offsets for the MUSTANG detector array. Error bars denote the FWHM of the beam. Measurements were made by making a map with each individual detector from a series of daisy scans on a bright unresolved calibrator. Centroids were determined by fitting an elliptical gaussian to each map. Gaps indicate locations with malfunctioning detectors or amplifiers.

When radiation is incident on the bolometer, its energy is deposited in the membrane and causes an increase in temperature which is measured by the thermistor. Eventually, the power is removed through the weak connection by the bath. A schematic diagram of three MUSTANG style TES bolometers is given in Figure 2.8.

In the case of MUSTANG, bismuth absorber is coated on a 10μm thick, 3.3 mm square silicon membrane. The bismuth coating is designed such that its surface resistance is well matched to the impedance of free space, $Z_0 = \mu_0 c_0$ ($\sim 376\Omega$), where μ_0 is the magnetic constant and c_0 is the speed of light in free space. With a well matched absorber, the incident radiation will deposit its energy in the detector its temperature will increase. The silicon membrane is mounted above a reflective backshort, separated by one quarter of a wavelength to further increase the absorption efficiency.

The silicon membrane is weakly connected to the bath via 4, 10μm wide silicon legs located at the corners of the square membrane. Two of these legs are functionally thermal only, and the other two also contain the superconducting leads which bias and read out

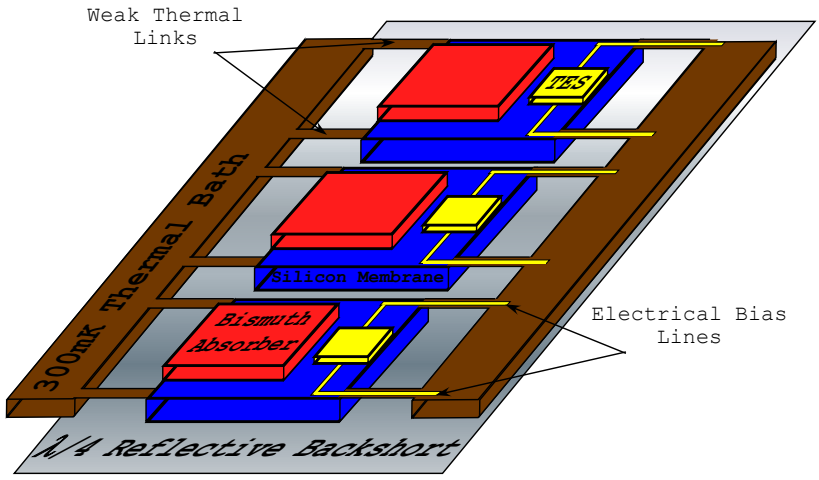

Figure 2.8 - Cartoon schematic of a three detector MUSTANG array. Diagram is not to scale. The MUSTANG detectors are 3.3 mm square silicon membranes (blue). The membranes are coated with a layer of bismuth which functions as an absorber (red). The TESs themselves are a bilyaer of molybdenum and gold (yellow). A reflective backshort is placed 1/4 of a wavelength behind the array to increase the absorption efficiency (Silver). The membranes are connected to the thermal bath by 4, 10μm wide legs of silicon which sets the thermal conductance of the devices. Two of these legs also contain the superconducting leads which bias the TESs.

the detector. The thermistor itself is a TES, made from a molybdenum/gold bi-layer. Photographs of the MUSTANG detector array are shown in Figure 2.9

2.3.2 Critical Temperatures

A TES is a superconductor, meaning at some low critical temperature, T_C, its electrical resistance drops to zero. While extremely sharp, this transition has a finite width. By voltage biasing the superconductor on its transition, a minute change in temperature produces a larger change in resistance and thus a measurable change in current. The superconducting transitions of two MUSTANG detectors are shown in Figure 2.10. These data were taken in the MUSTANG cryostat with an aluminum blank installed at 300 mK, ensuring the radiative load on the detectors to be near zero. Placing the minimal amount of voltage bias allowed by the DAC (37μV) across the detector circuit, the bath temperature was

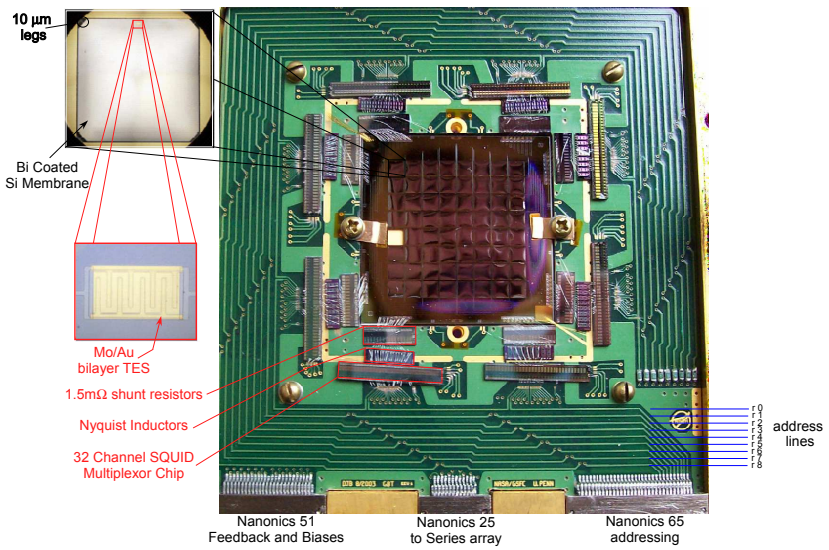

Figure 2.9 - MUSTANG's 8×8 array of TESs. The detector chip is pictured here mounted in its package and wire bonded into the circuitboard. Circling around the package on the top layer of the board are the address lines which carry the multiplexed boxcar voltage signal to read out the detectors. Visible on the circuitboard are 3 chips for each of 8 electrical columns. These are the shunt resistor chip, Nyquist inductor chip (bypassed in current configuration) and a 32-channel SQUID multiplexor chip. The two levels of inset show an individual detector membrane supported by the 10μm legs and a TES bilayer. The reflection of my face is visible in this photograph of the array.

systematically increased and the current flowing measured at each temperature. The low bias is required to ensure minimal Ohmic dissipation. The accuracy of the measurement relies on the assumption that the temperature of the detector is the same as that of the bath. Since the circuit was kept at constant voltage, the only change in current is caused by a change in resistance over a narrow range in temperature.

2.3.3 TES Theory and Electrothermal Feedback

The response of a TES is governed by a set of two coupled differential equations [Irwin, 2005]. They describe the dynamics governing the electrical and thermal circuits. The

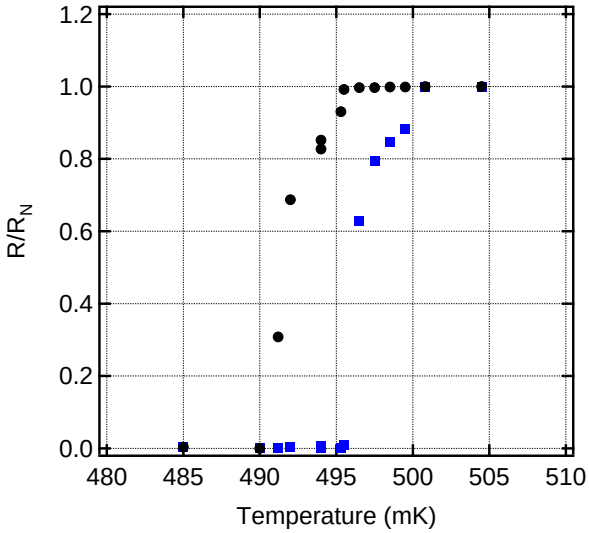

Figure 2.10 - Measurement of the superconducting transition temperature in two MUSTANG detectors. Data were taken with an optical blank at 300 mK and 37μV of detector bias.

thermal differential equation is given by:

$$C\frac{dT}{dt} = -P_{bath} + P_J + P_{sig}, \tag{2.1}$$

where C is the combined heat capacity of the TES, bismuth absorber and silicon membrane, T is the temperature, P_{bath} is the power flowing from the detector to the bath, $P_J = \frac{V^2}{R}$ is the Joule power dissipation and P_{sig} is the power from incident radiation in the form of a signal or optical loading from the atmosphere and internal optics. The electrical differential equation is:

$$L\frac{dI}{dt} = V - IR_L - IR(T, I), \tag{2.2}$$

where L is the inductance, V is the bias voltage, I is the current flowing through the sensor, R_L is the resistance of the shunt resistor plus any parasitic resistance in the circuit and $R(T, I)$ is the resistance of the sensor which is a function of both temperature and current. It should be noted than in both cases here, power contributions from noise fluctuations

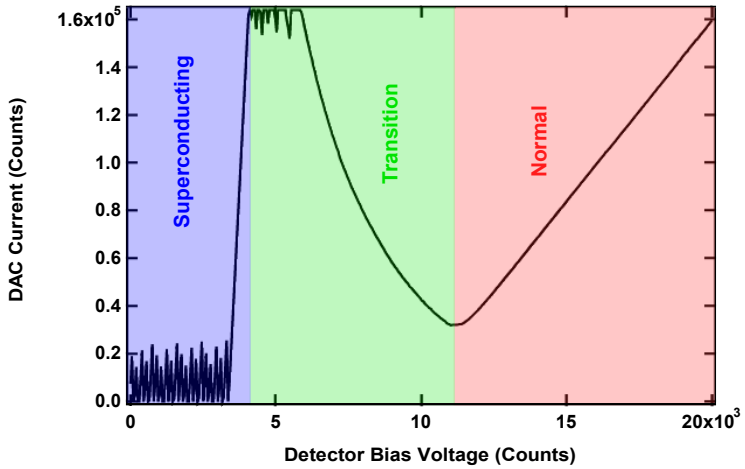

Figure 2.11 - I-V curve taken for a single detector through the MUSTANG readout electronics. Units are un-calibrated in raw counts. The dynamic range is set by the number of bits in the DAC feedback (2^{14}). There are three distinct regions of the curve; Red: High bias, where the TES is just a normal resistor and the I-V curve obeys Ohm's law. Blue: Low bias, where the TES is superconducting and the only resistance in the detector circuit is set by the shunt resistor and the I-V curve is a straight line again. Green: The region where the TES is on its transition and is governed by electrothermal feedback. All detectors must be biased in this region to be sensitive to radiation. Apparent oscillations at the base of the transition and throughout the superconducting region are artifacts which are produced when the dynamic range of the feedback loop is exceeded. One count of detector bias corresponds to 37 μV.

have been ignored for simplification.

The temperature dependence of the resistance term in Equation 2.2 and the presence of P_J in Equation 2.1 produce a complicated interplay between electrical and thermal effects in the TES behavior. When a photon is absorbed it produces a temperature signal in the TES. This is transformed into a current signal via the change in resistance. The change in current causes Ohmic dissipation and it is turned back into a temperature signal. This process, known as electrothermal feedback, works to naturally self-bias the device in temperature on the transition.

2.3.4 I-V Curves

Superconducting transitions of the TESs are controlled by voltage biasing so the bath temperature of the array can be kept fixed well below the transition temperatures. An extremely useful measurement for understanding the transitions of these devices is the $I-V$ curve, in which the detector bias voltage is varied and current flowing through the TES circuit is measured. These sweeps in V are always performed from high to low. This is necessary as it is impossible to drive a superconductor normal electrically by heating as it has no resistance and therefore will not heat through Ohmic dissipation. The detector must be driven normal by exceeding its critical current. Once the TES is normal, stepping down the bias V will take it through the transition.

An example of an $I-V$ curve taken with a single MUSTANG detector through the nominal readout electronics while on the telescope is shown in Figure 2.11. There are three distinct regions revealed. At high bias, the $I-V$ curve is a straight line. Here the TES behaves as a normal resistor in parallel with the shunt resistor. The same is true for low bias, when the resistance of the TES is exactly zero and the slope of the $I-V$ curve is determined by the resistance of a (1 kΩ) load resistor in series with the detector loop. When the TES is biased on its transition, the resistance changes with bias voltage and the $I-V$ curve is a hyperbola.

The apparent rapid oscillations in Figure 2.11 at the bottom of the transition and throughout the superconducting region, are artifacts caused by the limited the dynamic range of the feedback loop. Because of the non-linear nature of the amplifier chain (discussed in Section 2.4.1), the current scale in a raw $I-V$ curve taken with the MUSTANG electronics have an arbitrary DC offset. Each time the dynamic range is exceeded in an $I-V$ curve, the feedback loop is broken, and when it recovers, the DC offset will have changed. This offset can be measured by fitting a line to the normal section of the curve, as

Ohm's law dictates that an $I-V$ curve for a simple resistor should go through the origin. To calibrate an $I-V$ curve for measurements of intrinsic detector properties (e.g. Section 2.3.5), a line is fit to the normal section and the offset is subtracted from the entire curve. Only data taken within the dynamic range are used as they will have the same DC level.

2.3.5 Measurement of G for a MUSTANG Detector

The $I-V$ curve is an essential measurement for extracting device parameters such as the thermal conductance to the bath, G, which plays a crucial role in the speed and noise performance of the device. Figure 2.12 shows a series of $I-V$ curves taken at varied bath temperatures, T_{Bath}, with a single MUSTANG detector. These data were taken with an aluminum plate covering the array, heatsunk at 300 mK to ensure that $P_{sig}=0$. The power flow to the heat bath is related to the thermal conductance by

$$P_{bath} = K(T_C^{\beta+1} - T_{bath}^{\beta+1}), \tag{2.3}$$

where β is the thermal conductance exponent and $K = G/((\beta+1)T_C^{\beta})$ [Irwin, 2005]. By measuring P_J at a fixed point on the transition from $I-V$ curves in a radiation free environment, the intrinsic thermal parameters G, and β can be extracted by fitting equation 2.3 to the data. The resulting fit and residuals for a single typical MUSTANG pixel are shown in the right two panels of Figure 2.12. The best fit parameters and their 1σ statistical errors are given in the inset. In this fit, prior information was provided by measuring T_c with the method shown in Figure 2.10, this reduces the number of free parameters to two.

2.3.6 Detector Time Constants

Bolometers are inherently time domain detectors. During observations, the current flowing through the devices is constantly monitored as the telescope slews across a source

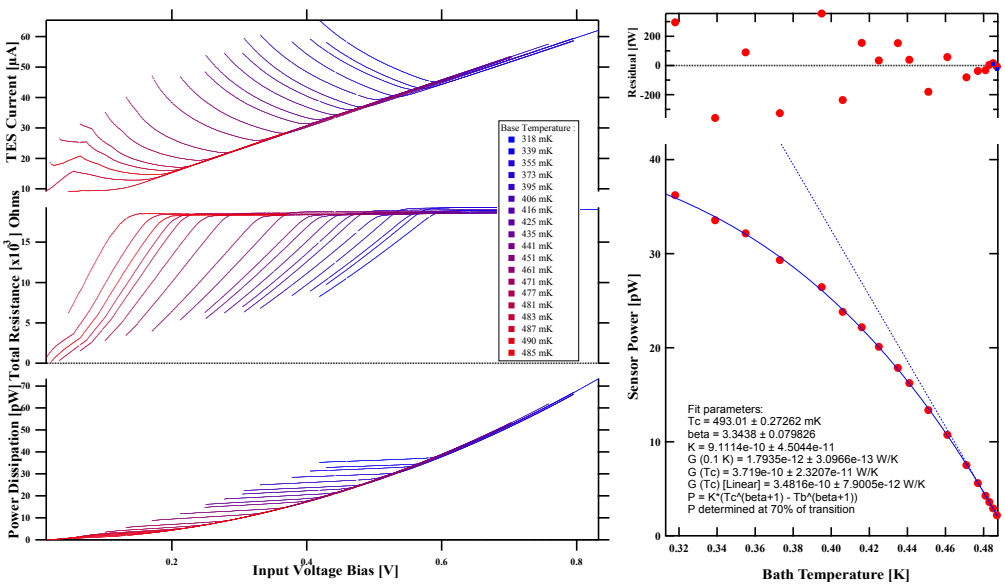

Figure 2.12 - Top Left: Measured $I-V$ curves for a single detector at varied bath temperatures. Middle Left: Total resistance as a function of bias voltage, calculated from above. Bottom Left: Power dissapation as a function of bias voltage, also calculated from the $I-V$ curves. Bottom Right: Sensor power at 70% normal resistance as a function of bath temperature and the fit expression.

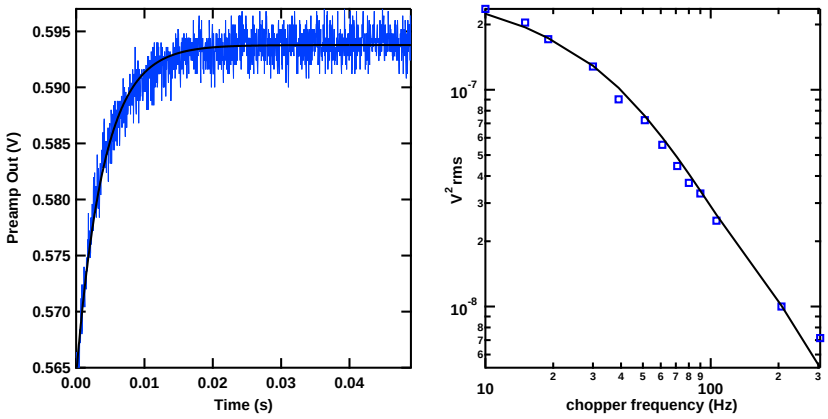

Figure 2.13 - Measurements of the detector speed of a typical MUSTANG pixel measured in the lab with two methods. Left: Blue shows the time response of a pixel responding to a square wave on the detector bias line. Black is the best fit exponential model with a time constant of 4.2 ms. Right: Blue shows the amplitude of a signal in the power spectrum of the detector with a nitrogen load chopped at variable frequency. Black is the best fit empirical model consisting of a two pole exponential rolloff with time constants of 5.0 ms and 1.0 ms.

with some characteristic speed. The details of this process are discussed further in Section 3.5. For a detector to measure a celestial signal, the incident photons deposit their energy in the bismuth coated membrane which causes heating subsequently measured by the TES. This process, like any exchange in thermodynamics, has a timescale associated with it. In a simplified case (ignoring electrothermal feedback for the time being), the thermal time constant of a bolometer, $\tau = C/G$, where C is the heat capacity and G the thermal conductance between the membrane and the bath. This means that a step function in signal will appear in the detector output as if it were convolved with the function $e^{-t/\tau}$. If the telescope were scanned infinitely fast across a celestial source, no signal would be measured by the TES as it would not have time to warm up and detect the radiation. It is essential to measure the characteristic time constant of the devices and ensure that it is much shorter than the time it will take for a source to move through the beam. For speeds which the GBT can realistically scan, a point source will go through the beam in a time on the order of several hundred milliseconds.

Detector time constants were measured in two independent fashions to confirm the system had adequate speed capabilities. To measure τ in the time domain, a square wave was fed down the detector bias line. Figure 2.13 shows the time response of a single detector biased on its transition to the rise of the square wave. These data were digitized with a digital oscilloscope instead of the MUSTANG readout electronics to ensure fast sampling. The data are well described by a simple exponential with $\tau = 4.2$ ms.

The time constant was also measured in the Fourier domain. An optical signal from a 77 K blackbody was modulated with a chopper with a set frequency and placed in the beam of the receiver. The output of the amplified detectors was fed on coaxial signal into an analog spectrum analyzer to take the Fourier transform of the time stream. This was repeated with the frequency increased systematically from 10 Hz to 300 Hz. Figure 2.13 shows the amplitude of the chopped signal in the power spectrum of the detector timestream

as a function of chopper frequency. The attenuation of the signal is well described by a two pole rolloff with $\tau_1 = 5.0$ ms and $\tau_2 = 1.0$ ms.

The results indicate that the speed of the detectors is close to two orders of magnitude faster than the speed at which astronomical signal is modulated. This is more than adequate for the requirements of MUSTANG.

2.3.7 Detector Noise and Saturation Power

The sensitivity of any detector is limited by its noise performance. It is therefore essential to obtain accurate measurements in the laboratory and properly characterize the devices. High frequency spectra of the current noise fluctuations for a single MUSTANG detector in the superconducting, normal, and transition states are shown in Figure 2.14. Because the frequencies of interest are 4 to 5 orders of magnitude higher than astronomical signal would be, the feedback and multiplexing electronics are insufficient for this measurement. In order to probe the noise out to 100 kHz, data were taken with an analog spectrum analyzer in the laboratory. The direct output of the series array with multiplexing disabled was taken from the coaxial cable output from the warm electronics tower and fed directly into the spectrum analyzer. Because the amplitude of the fluctuations is well within the small signal limit, nonlinearities in the amplifier response (discussed in detail in Section 2.4) are not of concern.

When the detector is in either a superconducting or normal state (red and blue traces respectively), the amplitude of current fluctuations is set simply by the Johnson noise of a resistor, $i_n = \sqrt{\frac{4k_B T \triangle\nu}{R_i}}$, where $\triangle\nu$ is the frequency width over which the noise is being measured and R_i is the resistance of the circuit. R_i is set by the shunt resistor when the TES is superconducting or the combination of the shunt and TES in parallel when normal. Figure 2.14 also shows that the high frequency end of the spectra are attenuated in both cases. This is set by the input inductor in series with the TES, which works with

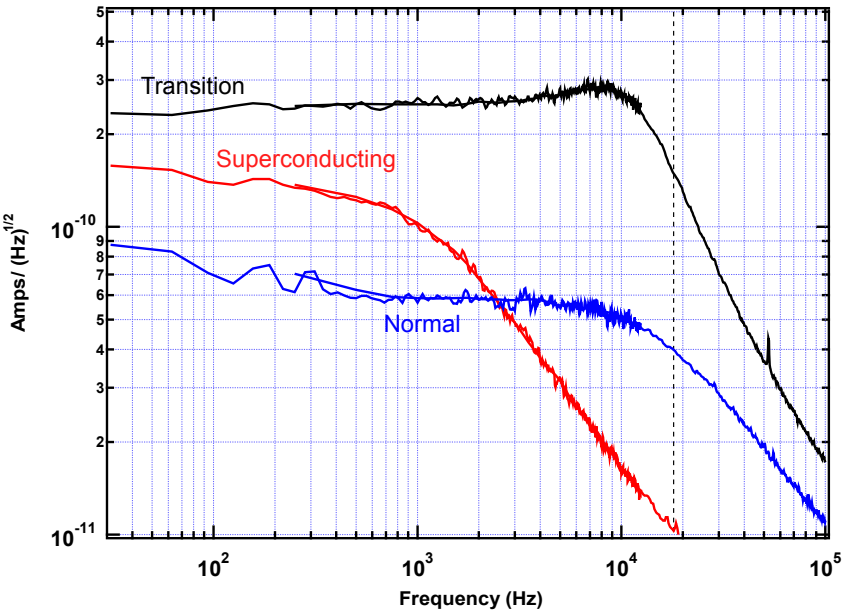

Figure 2.14 - Measurements of the high frequency noise characteristics of a single detector in the superconducting, normal and transition states.

the resistors to form a simple electrical L R filter. The critical frequency of the circuit, $f_c = \frac{R_i}{2\pi L}$, is the frequency at which the filter will attenuate half of an incoming signal. The observed increase in f_c and decrease in i_n from the superconducting to normal states are well described by Johnson noise attenuated by an $L - R$ filter.

When biased on the transition (black spectrum in Figure 2.14), the high frequency noise attenuation is still set by the critical frequency of the $L - R$ filter, where R is now set by the combination of the shunt and TES at some fraction of its normal resistance. The measurement of f_c in the transition state is essential, as it constitutes the Nyquist frequency required for digital sampling of the detector timestreams. Sampling slower than f_c will result in the aliasing of high frequency noise into the signal band which further limits sensitivity. For the MUSTANG pixels, $f_c = 18.5$ kHz. This is marked with the black dashed line in Figure 2.14 and is used as the sampling rate in observations. This frequency can in principle be reduced to avoid such high sampling rates by adding inductance in series with the TES. The original MUSTANG detector design included an inductor chip in each

column specifically for this purpose. These chips are mounted to the surface of the circuit board on the array package and are visible in Figure 2.9. However, when electrical time constants are on the same order as the thermal time constant of the detectors, runaway electrothermal oscillations can occur rendering the detectors useless [Irwin, 2005]. In order to stabilize the array, the inductor chips were bypassed with wirebonds and the f_cs were increased. This does not pose a problem as the multiplexing electronics are capable of Nyquist sampling at 18.5kHz and data sizes can be reduced by coadding samples together.

By comparing the amplitude of the noise on the transition to that in the superconducting and normal states, it is clear that the fluctuations are much higher than expected from Johnson noise alone. The resistance of the TES is in between its values in the superconducting state (exactly 0 Ω + R_L) and the normal state, yet the amplitude is above both other traces. This is due to added noise from thermal fluctuations associated with processes which govern the exchange of energy across a thermal link between two heat capacities [Irwin, 2005]. The thermal fluctuation power noise, $S_{P_{TFN}}$, contributes to the overall power spectrum of the device in the amount

$$S_{P_{TFN}} = 4k_B T^2 G F(T_{bath}, T), \tag{2.4}$$

where the function F parameterizes the details of the nature of the thermal link and its temperature dependance(these details are beyond the scope of this thesis but can be found in Irwin [2005]).

When interpreting the noise spectrum of a MUSTANG detector on its transition, it is clear that the simple model of a TES consisting of a single heat capacity coupled to the bath through a single thermal link is insufficient. As shown in Section 2.3.6, thermal interactions across the G which links the membrane to the bath can only occur on timescales slower than ~ 5 ms. However, the power spectrum shown in Figure 2.14 does not attenuate until

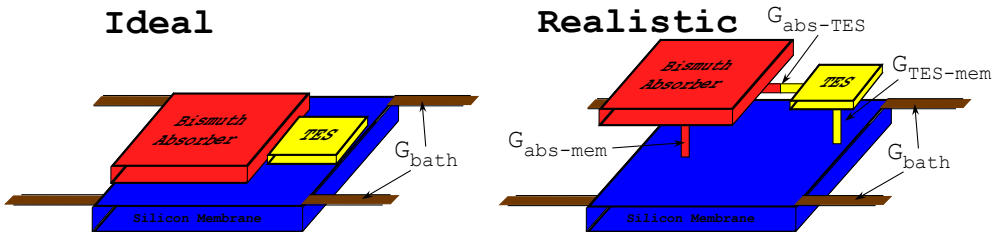

Figure 2.15 - Comparison of cartoon TES models. Left: An ideal MUSTANG style TES bolometer consisting of a single thermal link between the membrane and the bath (G_{bath}). Right: A more realistic model in which there are additional thermal links between the bismuth and the silicon ($G_{abs-mem}$), the bismuth and the TES ($G_{abs-TES}$) and the TES and the silicon ($G_{TES-mem}$). Thermal fluctuation noise across each of these links will contribute to the power spectrum of the device.

18.5 kHz. There must be substantial additional thermal fluctuation noise contributing at high frequency which is originating from thermal links other than those from the bath to the membrane.

Within a detector, there are finite thermal conductance links between the TES and the silicon membrane, the bismuth absorber and the silicon membrane, and the bismuth absorber and the TES. These links all contribute thermal fluctuation noise and can occur on timescales much faster than 5 ms. A cartoon thermal model of a TES bolometer including these links is shown along side the simplest model in Figure 2.15.

A key dependance to note in Equation 2.4 is that the noise equivalent power (NEP) of a TES increases with larger G. Equation 2.3 shows that the saturation power of the device also increases with G. This introduces a tradeoff in device performance. Higher G will provide detectors with more headroom to saturation but will also degrade the noise performance. It will also decrease the thermal time constant. The MUSTANG detectors have saturation powers of 40 pW at $T_{bath} = 300$ mK set by a G of $3.72 \times 10^{-10} \pm 2.3 \times 10^{-11}$ W/K at T_C. This provides a substantial amount of headroom over the ~ 10 pW of loading from the atmosphere on a night with reasonable weather at Green Bank. This conservative design choice led to a robust detector array. The detectors can be operated in the lab with a 300 K optical load without saturating which is useful in characterization. They

will also never saturate during observations from an extremely bright source or extreme atmospheric loading. However, this choice has yielded higher NEPs than desired for the fastest mapping speed possible. The measured NEP for MUSTANG detectors below 10 Hz is $\mathbf{1.6 \times 10^{-16}}$ W/$\sqrt{Hz}$.

2.4 Time Domain Multiplexed Readout

2.4.1 SQUIDs

The MUSTANG readout electronics system consists of a series of superconducting quantum interference devices (SQUIDs) multiplexed in the time domain. They are read out using a set of electronics and amplifiers developed at the National Institute of Standards and Technology and NASA Goddard. The system has been modified to operate the MUSTANG receiver.

For the scope of this thesis, SQUIDs can be regarded simply as exquisitely sensitive detectors of magnetic flux capable of low noise amplification over a broad range of bandwidth. SQUID based amplification systems are complicated by the fact that while sensitive to small changes in magnetic flux, ϕ, their response is highly non-linear. The voltage response of a SQUID is given by

$$V = \frac{R}{2}\sqrt{I^2 - (2I_C cos(\pi\phi/\phi_o))^2}, \tag{2.5}$$

where I_C is the critical current which will drive the superconductor normal if exceeded, and the quantity $1/\phi_o$ is the Josephson constant [Tinkham, 1996]. When the quantity ϕ/ϕ_o is close to an odd multiple of 1/2, the slope of the response function of the SQUID, $dV/d\phi$, can be quite steep. When biased to this region of its response curve, a current signal flowing through the SQUID induced by a magnetic flux signal will be larger than the original current flowing through the input inductor. In other words, the inductor coupled SQUID

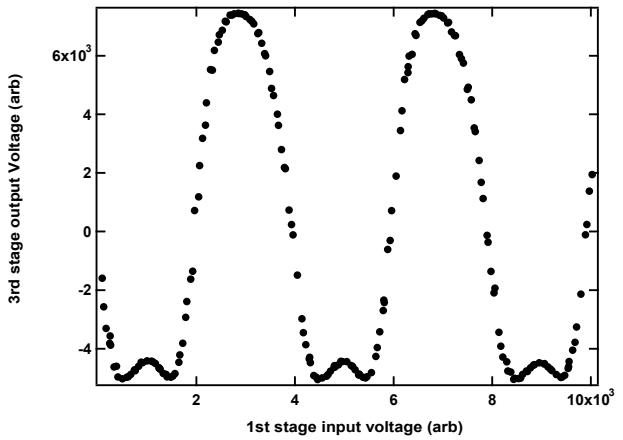

Figure 2.16 - Voltage output of the 3 stage SQUID amplifier chain for a single MUSTANG pixel. The voltage output of the chain responds periodically to the change in magnetic flux through the 1st stage SQUID, however, the range between roughly -2000 and 4000 counts output voltage is approximately linear. The feedback loop is designed to limit the amplifier response to this linear regime.

provides substantial gain for a current signal. This makes SQUIDs useful as amplifiers.

In the case of the MUSTANG amplification system, there are three stages of SQUIDs, in which the output of each stage is input into the next. This is required to achieve the necessary gain to digitize signals with an appropriate dynamic range but produces an even more complicated gain curve such as the one shown in Figure 2.16. To circumvent this unfavorable characteristic of the SQUIDs, a digital feedback loop is implemented to linearize the output. A schematic of the readout system is provided in Figure 2.17. Photographs of the various components of the electronics are given in Figure 2.18.

By including an input inductor, L_{in}, in series with each voltage biased TES, a current signal produced by a resistance change upon absorption of radiation is transduced into a magnetic field. This inductor is geometrically coupled to a first stage SQUID which turns this difference in magnetic flux into a current signal. The MUSTANG architecture has a first stage SQUID for every individual pixel and are read out by multiplexing in the time domain.

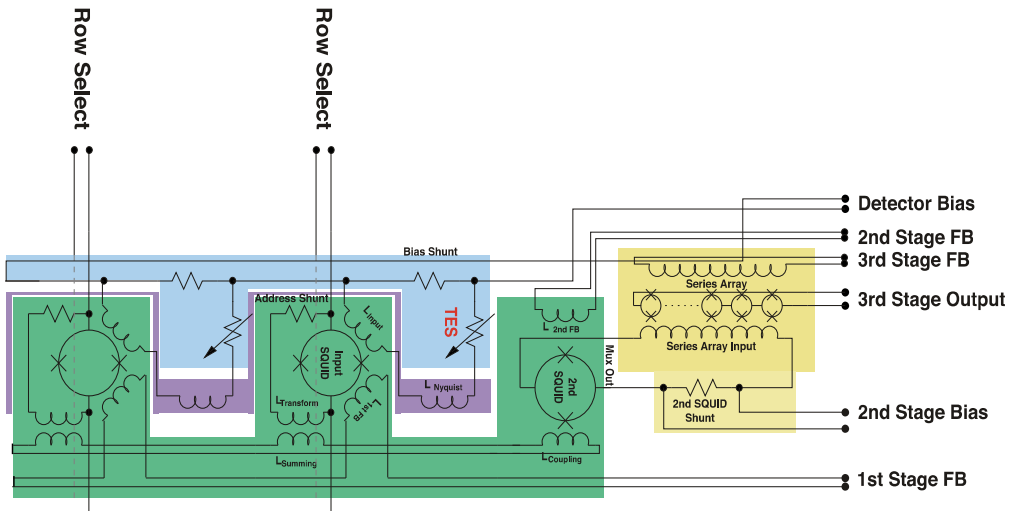

Figure 2.17 - Schematic diagram of the detector circuit and the three stage multiplexed SQUID electronics. For simplicity, only two rows of a single column are shown here. Figure adapted from work by Dominic Benford.

2.4.2 Multiplexing

The multiplexing system exploits the fact that a SQUID is only sensitive when it has the appropriate voltage bias across it. Instead of a DC voltage, the first stage SQUIDs are biased with a periodic boxcar function that is high for a given window, and zero for the rest of the cycle. A readout cycle, or "frame", is subdivided by the number of rows in the electrical column. In the case of MUSTANG, which has an 8×8 array read out with 8 multiplexer chips, a frame is divided into 9 parts (the last row is for a "dark" SQUID which has no detector coupled to it). Throughout this chapter, a column refers to the pixels which share an amplifier chip. This differs from a physical column in the square array. Each subdivision of the frame constitutes a "row visit". The phase of the boxcar function seen by each row of SQUIDs is offset by 1/9th the period of the frame. All of the first stage SQUIDs in a given column are coupled in series through a mutual inductance to the input of a single second stage SQUID. As only one first stage SQUID per column is biased high at a given time, the signal input to the second stage SQUID comes from only one pixel at a given instant.

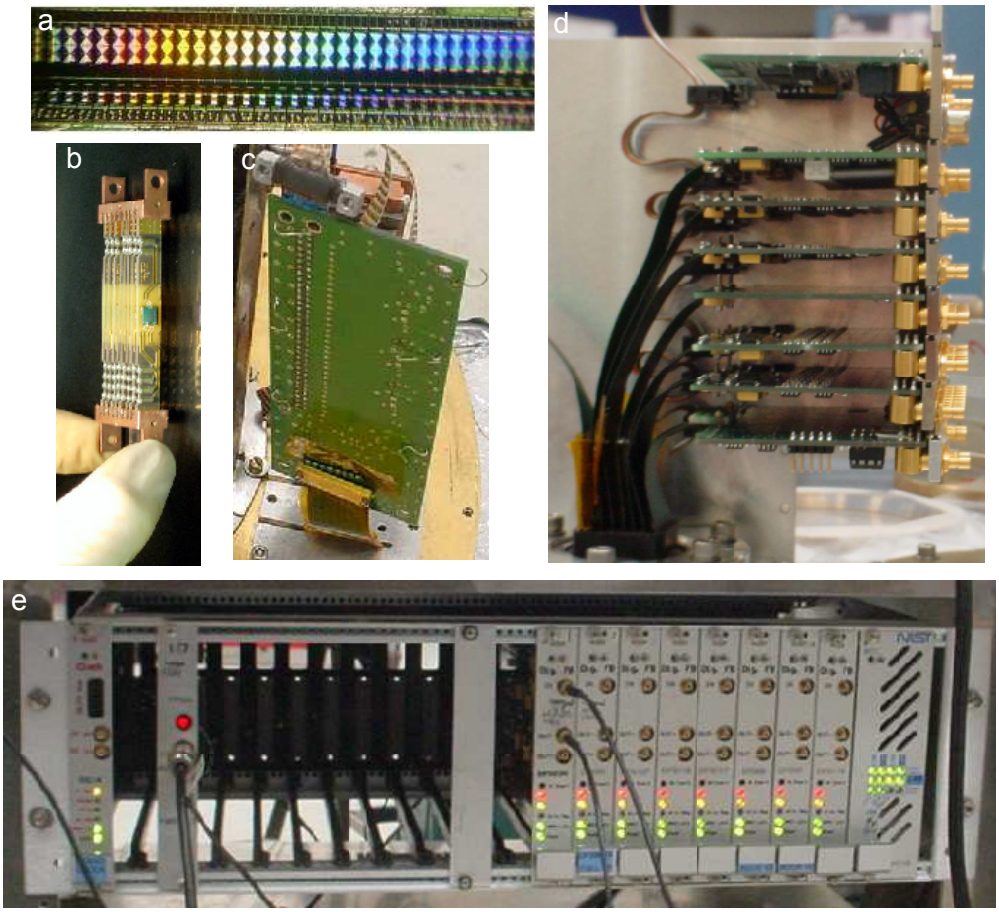

Figure 2.18 - Photographs of the main components in the readout electronics system. *a* : A 32 channel NIST SQUID multiplexor chip. *b* : The series array module without its casing. *c* : The cold address driver which does the multiplexing. *d* : The warm tower electronics cards. Listed in order from top to bottom: Power, Series Array output, 3rd stage feedback, 2nd stage bias, feed-through, 2nd stage feedback, detector bias and address card. *e* : The crate electronics including 8 digital feedback cards, a power card, an interface card and a clock card. These are connected via optical fiber to a computer where the data is archived.

Table 2.2. Multiplexing and Feedback Parameters

Parameter	Value	Description
Clock Divider*	2699	Length of frame (LSync×NStep - 1)
NSTEP	8	Number of row visits per column
LSync*	300	Length of row visit
NSamp*	80	Number of samples of SA output averaged
Settle*	200	Number of samples to wait before averaging after row visit
Coadd	20	Number of consecutive frame visits to average
Vref	400	Reference voltage for high bias in boxcar
LUT start	0	First row to be visited after frame pulse
LUT delta	1	Interval of rows between visits

Note. — *Parameters are in samples of the 50 MHz clock. 1 sample corresponds to 2×10^{-8} s.

The first two stages of amplification are located on a single chip mounted to the surface of the circuit board on the array package at 300mK. The multiplexed signal is then routed through a Nanonics connector and a set of Nomex woven superconducting wires to the third stage of amplification[3] utilizing a series array (SA) of SQUIDs at 3 K which provides the final gain before digital sampling. The signal is then routed on planar flexible RF transmission lines to the 300 K warm electronics tower where it leaves on a coaxial cable. The multiplexed SA output is fed into a digital feedback (DFB) card located in an RFI tight electronics rack which sits below the cryostat on the telescope. The DFB cards contain field programmable gate arrays (FPGAs) with firmware written by the team at NASA Goddard space flight center to run the feedback algorithm. The bolometer signal is the feedback to the first stage SQUID which is digitized and sent to the data acquisition computer.

The first stage SQUIDs are coupled to a feedback inductor, L_{fb}. This coil is wound in the opposite direction as L_{in} and will therefore cancel magnetic flux through the first

[3]Cryogenic cabling commercially obtained from Tekdata (www.tekdata-interconnect.com)

stage SQUID when the appropriate amount of current is applied. The feedback algorithm in the FPGAs is designed to calculate precisely the appropriate amount of current to apply to L_{fb} that will maintain the voltage output of the SA at a given DC target value. This target value is selected to be in the center of the linear regime of the SQUID output. The multiplexed feedback signal is fed down to the detector package through coaxial cable, to a feedthrough card in the tower, down a flex line, through a breakout board at 3 K, through woven superconducting wires, through a Nanonics connector to the array package. The DFB cards are connected via optical fiber to a computer. The output of the digital to analog converter (DAC) on the DFBs are stored digitally on the computer. It is this signal which contains astronomical data. The scaled accumulated error (SAE) is also stored. This is defined as the difference between the measured output of the SA and the target value.

There are several parameters used in the multiplexing and feedback system which have been optimized for use in MUSTANG. These variables and their optimal values are given in Table 2.2. The system keeps time from a 50 MHz clock card operating in the electronics crate. The data sampling rate is set by a "clock divider" which governs the period of a frame pulse. Each detector is sampled once per frame. The minimum sampling speed is set by the noise characteristics of the detectors. The high frequency noise spectrum of a typical detector given by the black trace in Figure 2.14 shows that the noise begins to roll off at $\sim$ 10 kHz. This cutoff frequency is set by the ratio L_{in}/R_{Tot} in the detector loop, where R_{tot} is the effective resistance of the TES and the shunt resistor in parallel. To avoid aliasing high frequency noise into the signal band, the detectors need to be digitally sampled at a higher frequency than the roll off. For the MUSTANG system, the slowest sampling rate necessary to avoid significant aliasing is 18.5 kHz.

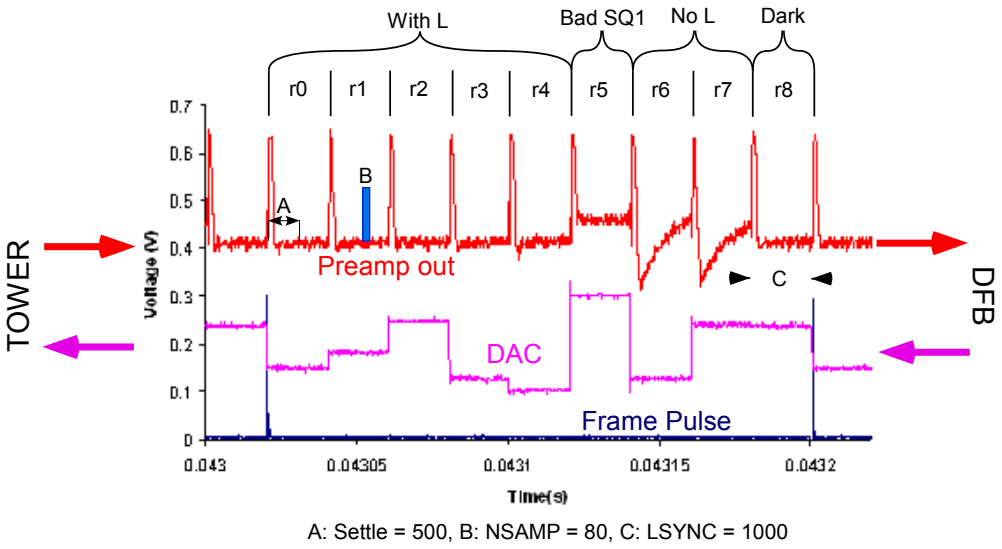

Figure 2.19 - Oscilloscope traces of the frame pulse (blue), Output of the DFB card going into the tower (purple), and the output of the series array going into the DFB cards (red). Sampling parameters used in this trace are labeled. These data were taken in a test configuration in which the first 5 detector loops had additional inductors to limit high frequency noise. This had the side effect of producing electrothermal oscillations when the detectors were biased on the transition. Rows 6 and 7 have the additional inductors removed and therefore show a slow recovery to the clock pulse. While unfavorable, this recovery is stable and does not introduce noise into the feedback loop. The times spanned by the number of 50 MHz samples in Settle, NSAMP and LSYNC, defined in Table 2.2 are shown as well. Multiply by 2×10^{-8} s to convert to time.

2.5 Vibration Susceptibility

The 2006 commissioning season on the GBT was designed to test end to end systems functionality of the receiver and a successful integration with the GBT. While very successful, the data was plagued by low frequency ($1/f$) noise in the detector timestreams. Throughout the run, only the brightest celestial sources in the sky could be mapped.

The extraneous noise had a variety of unexplained features and many models were proposed. Fluctuations introduced by the cryogenics or readout electronics were initially deemed unlikely as principal component analysis demonstrated that the noise was completely uncorrelated from pixel to pixel. This fact, in the context of a multiplexed readout electronics system, made it evident that the noise was being introduced inside individual detector loops.

After several months of tests to determine potential causes intrinsic to pixel membranes, the source was identified. The noise appeared to vanish when the PT cooler was disabled. Initially, electromagnetic RFI was thought to be introduced from the stepper motor driver in the PT head, but running the driver without the flow of compressed helium did not induce fluctuations. It was determined that the likely cause of the noise was mechanical vibrations induced in individual pixels driven by the PT. Non-homogeneous characteristics of individual detectors caused by imperfections in lithographic processes during fabrication could result in slightly different mechanical properties and resonant frequencies of each detector. The intrinsic array architecture consists of a membrane under tension by the thermal legs (see Figure 2.8), making them susceptible to mechanical oscillations.

To test this theory and potentially mitigate the noise, modifications to the cryostat were made to vibrationally isolate the 40 K first stage and 3 K second stage of the PT from their respective baseplates. This was done by replacing hard mounted oxygen free high conductivity (OFHC) copper plate heat straps with flexible copper braid. The 3 K

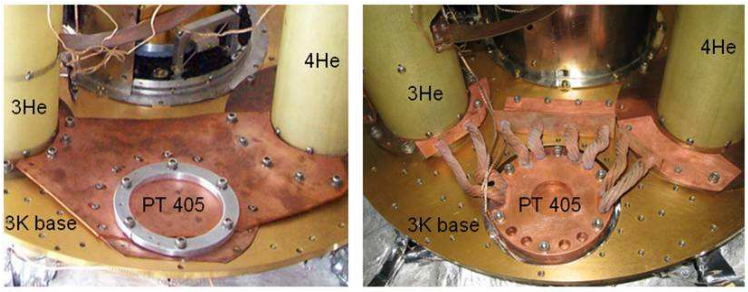

Figure 2.20 - Thermal link from the second stage of the PT before (left) and after (right) modifications for reduced mechanical coupling.

modifications are illustrated in Figure 2.20.

The first cooldown after mechanically isolating the cryostat from the PT confirmed that the fluctuations were indeed being caused by microphonics. A drastic improvement in noise performance was observed across the array. In extreme pixels, the NEP in the 1-2 Hz astronomical signal band improved by over two orders of magnitude. Power spectra from one such pixel are displayed in Figure 2.21.

The narrow feature at 1.4 Hz which remains in the spectrum is caused by thermal fluctuations in the PT. While this undesired effect does reside in the heart of the significant signal band, it is very close to sinusoidal in nature and is completely common mode, making it easily removed in data analysis as described in Section 4.

Figure 2.22 displays noise levels at 1 Hz across the array as seen in a noise power spectrum normalized to optical response before and after vibration isolation. The majority of pixels improved by over a factor of 10 in noise performance, extreme cases improved by over a factor of 100.

While overall array wide fluctuations are greatly reduced, several pixels still display traces of $1/f$. Pixel c2r1 is an extreme example of this effect. A timestream of this detector with the PT turned off during the file is displayed in Figure 2.23. The fluctuations of this pixel manifest themselves as $1/f$ when examined in frequency domain. However,

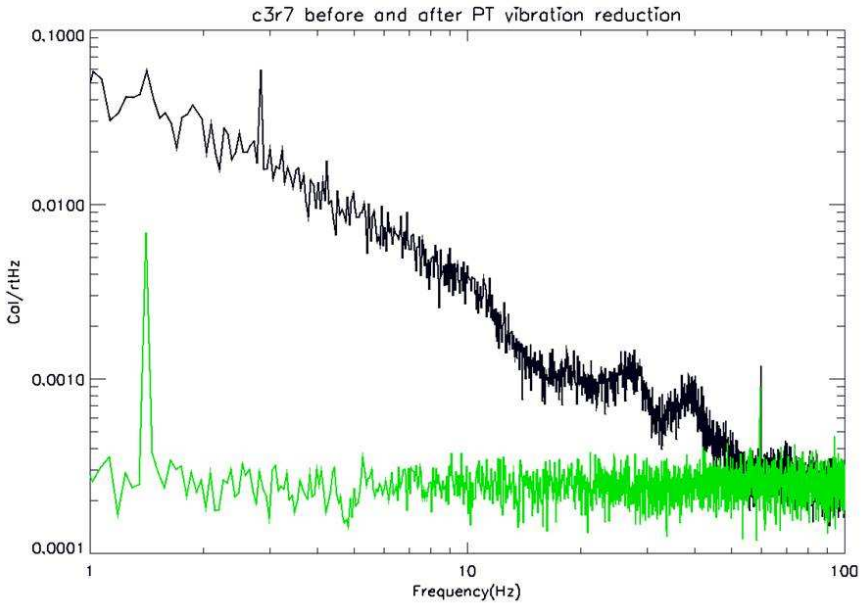

Figure 2.21 - Noise power spectra in units of the CAL response before (black) and after (green) vibrational isolation of the PT. Fluctuations induced by microphonics in the PT have been mitigated severely. The feature at 1.4 Hz in the green spectrum is from thermal fluctuations and is well represented by a sinusoid.

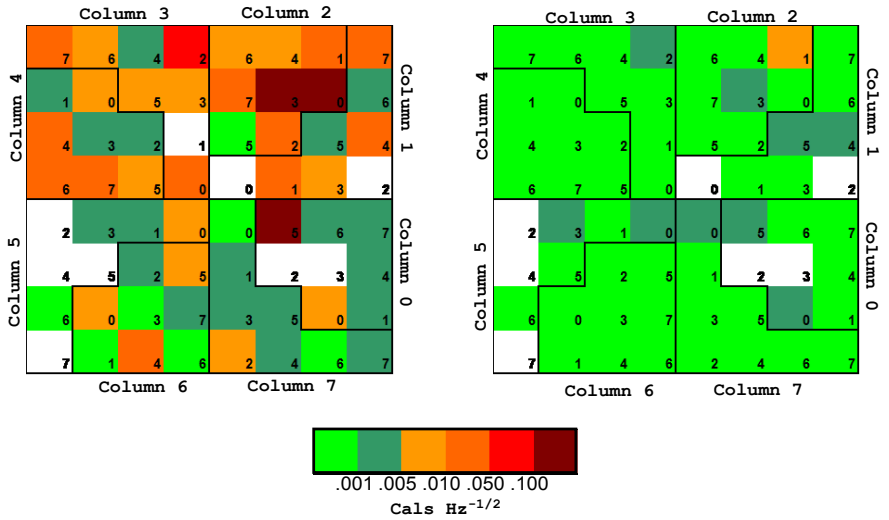

Figure 2.22 - Distribution of $1/f$ noise across the array before (left) and after (right) PT vibration isolation. The color assigned to each pixel corresponds to the noise level at 1 Hz normalized in units of the optical response.

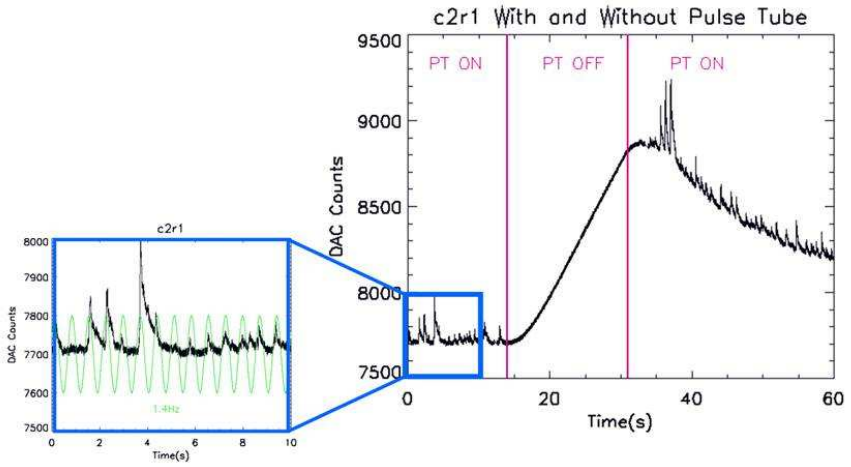

Figure 2.23 - Timestream of a single pixel with the Pulse Tube on and off. Inset displays the timestream overlaid with a 1.4 Hz sine wave

close examination of the timestream reveals that the excursions are synchronized with the 1.4 Hz pulsing of helium in the PT. The amplitude of these fluctuations varies with a $1/f$ envelope. This effect is conveyed by the inset of Figure 2.23. When the PT is disabled, the noise vanishes and the signal drifts due to warming. When it is turned back on, the noise returns.

To further probe the characteristics of the microphonics which drive $1/f$ fluctuations in individual pixels, sinusoidal vibrations of known frequencies were introduced into the system. Loudspeakers driven by a signal generator were placed on top of the 300 K lid of the cryostat. Sound waves were sourced through a range of frequencies between 20 Hz and several kHz. Timestream files of the entire array were taken at each frequency in 2Hz intervals across the range. Later, 0.5 Hz steps were taken across a region of interest. The standard deviation of the TES current timestreams for each file is plotted against driving frequency in Figures 2.24 and 2.25. By introducing driving frequencies around 150 Hz at 300 K, we were able to create timestream fluctuations with $1/f$ spectra and virtually indistinguishable characteristics to those that plagued the instrument on the telescope. This experiment was repeated later with finer frequency resolution (0.5 Hz). These results

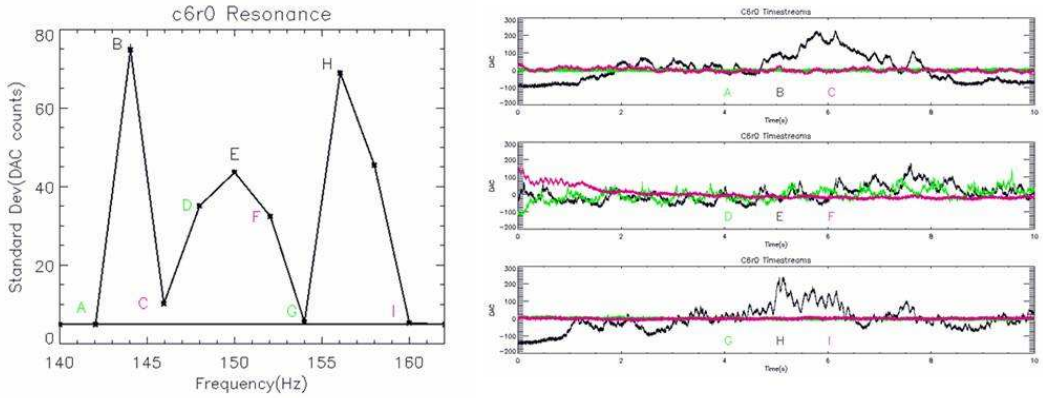

Figure 2.24 - Timestreams(Right) and their corresponding standard deviations(Left) from a single pixel with driving frequencies coupled from an audio speaker between 140 Hz and 162 Hz.

for an entire multiplexed column are displayed in Figure 2.25. While the general location of features ($\sim$ 150 Hz) in pixel c6r0 is consistent with the coarser data, morphology and exact location vary slightly. This suggests that mechanical properties in the cryostat are variable to some degree.

A key result of this test conveyed by Figure 2.25 is the presence of variation in resonant frequencies from detector to detector. It is also important to note that fluctuations in timestreams taken when multiple pixels are resonating do not display common mode characteristics. In higher frequency scans not displayed in Figure 2.25, a small overtone feature near 300 Hz is also seen.

The mechanical environment on the GBT is also of concern. The turret is equipped with a "blower" designed to maintain a constant flow of warm air over the Goretex covers of the feedhorns to prevent condensation. The compressor which drives this blower produces significant vibrations which excite this resonance. For this reason, the blower is always disabled during MUSTANG observations.

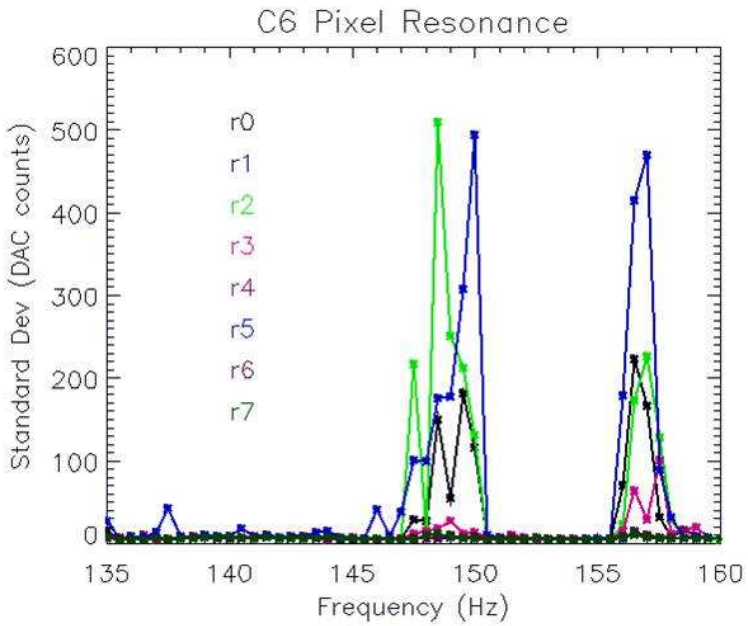

Figure 2.25 -0.5 Hz resolution timestream standard deviation as a function of driving frequency for all pixels in column 6.

Chapter 3

Observations

The custom observing procedures have been developed for MUSTANG to optimize efficiency in mapping compact and extended sources are described in this chapter. Currently, MUSTANG observations are only carried out at night beginning no sooner than 2 hours after sunset. This is done to avoid thermal changes on the telescope caused by solar illumination. It is essential to ensure that the cryogenics are fully operational having completed a thermodynamic cycle described in Section 2.2.2 before the start of an observing run. This is generally completed automatically on a daily basis, however monitoring the system in the hours before the observing run is generally required to avoid lost telescope time.

3.1 SQUID Biasing for Observations

Once the second stage of the PT is cool and stable after the completion of a cycle, the electronics can be activated. During a cycle, the power supplies to the warm tower and the rack of DFB cards is turned off. This is done to avoid producing currents and changing the magnetic environment in the cryostat when various metallic components go through their superconducting transitions. The multiplexing and data acquisition electronics are activated and configured with the sampling parameters given in Table 2.2. Once the mul-

tiplexing is functional and the control computer is parsing the incoming data packets, the SQUID amplifier chain can be biased. For each multiplexed column of detectors, there are four DC voltages which need to be set. This consists of a bias and "feedback" for both the second stage SQUID and series array. The nomenclature of "feedback" parameters in this case is somewhat misleading as they are really DC biases across an inductor coupled to the SQUID input. There is no active feedback process enabled at the later stages of amplification. The purpose of these inductors is to provide a tunable offset to each stage of SQUID such that all are biased to the linear section of their response curves and the gain is both stable and linear.

The optimum series array and second stage biases are determined by intrinsic SQUID properties and therefore do not require modification from session to session. The baseline magnetic environment in the cryostat, however, can change slightly from cycle to cycle. Therefore, feedback parameters occasionally need to be modified. To tune the SQUIDs before observing the following process is executed.

- A set of previously determined optimum biases are restored. This generally brings the response of the SQUIDs close to the optimum state.

- The output of the DFB cards is ramped as a triangle wave while the output of the amplifier chain is monitored in the time domain. This allows for visual inspection of the SQUID response and the relative magnetic phase offsets of the three stages.

- If the response of a given column is determined to be less than optimum, the feedbacks are changed. The key desired characteristics of a well biased amplifier chain are a large overall amplitude ($> 10,000$ counts), and minimal secondary maxima and minima. If a secondary peak or trough, caused by the misalignment of the nulls in second and third stage response has an amplitude comparable to the location of the linear part of the curve, the feedback loop can have difficulty locking at the appropriate

position as the target value is degenerate within one ϕ_o. An example of a secondary peak is visible in Figure 2.16 at $\sim 5,000$ counts DAC. In this case the amplitude is sufficiently low to avoid issues with locking. If the secondary peak is present at an obstructive level, second stage feedback is stepped systematically until the amplitude is reduced to acceptable levels.

- The target level for the feedback algorithm are set. This value is chosen to be near the center of the range of outputs of the amplifier chain and in the region where the output is linear.

- The "Default DAC" parameter is set, generally to 8,000 counts. This parameter gives the feedback loop an initial guess at the voltage required to linearize the SQUID output. Since the SQUID response is periodic, there are several DAC values within the dynamic range (2^{14} counts) which will bring the output to the target value. 8,000 counts is chosen as it is close to the center of the dynamic range. This value is therefore optimized to avoid loss of lock due to drifts in loading or the mapping of very bright sources.

3.2 Detector Biasing for Observations

The above process of SQUID biasing can be carried out before the MUSTANG observer gains control of the telescope. However, when another observer is using the GBT with a different Gregorian receiver, MUSTANG will be in the turret at a location other than the focus. The architecture of the GBT is set such that the main beam from the receiver will be obstructed by various support structures when it is not in the focus. This will produce an increased load on the detectors which makes biasing the TES array difficult.

Once the MUSTANG observer is given telescope control, the receiver is rotated into

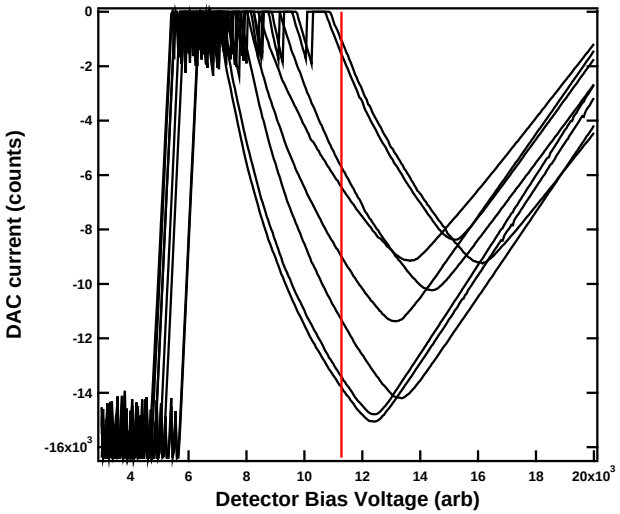

Figure 3.1 - $I-V$ curves for all pixels in a single column taken on the telescope with MUSTANG in the Gregorian focus. The scatter in T_C and R_{Shunt} yields a variation in the location of the transition region in bias curves. Since all detectors in a single column are biased with a single voltage, the detectors will have different resistances and therefore scattered gain. The red line shows the chosen bias voltage which places all detectors on their transitions. The spread in these bias curves produces variations in the gain of individual pixels. This is accounted for by flat-fielding using CAL.

the Gregorian focus. With the loading on the detectors dominated by sky emission as it is during observations, the detectors can be biased. $I-V$ curves for each detector are taken to map the bias locations of the sensitive transition regions of each pixel. The multiplexed architecture of the MUSTANG array, by design, limits the number of detector bias lines going to the array and each electrical column is wired in series. A side effect of this is that all pixels in a given column must be biased on their transitions with a single voltage. As Figure 3.1 conveys, scatter in TES properties such as T_C and G can produce a non-negligible scatter in the location of the transition in an $I-V$ curve. The voltage chosen to bias the column in this example is indicated by the red line. While all pixels can be simultaneously biased on their transitions, the intrinsic spread leads to a range in the fraction of normal resistance each detector has at the given bias point. The range in this case, which all pixels are sensitive to photons, spans the biases between 6,000 and 12,000 counts. The chosen bias was 11,500, closer to the top of the allowed range. This was selected to avoid biasing

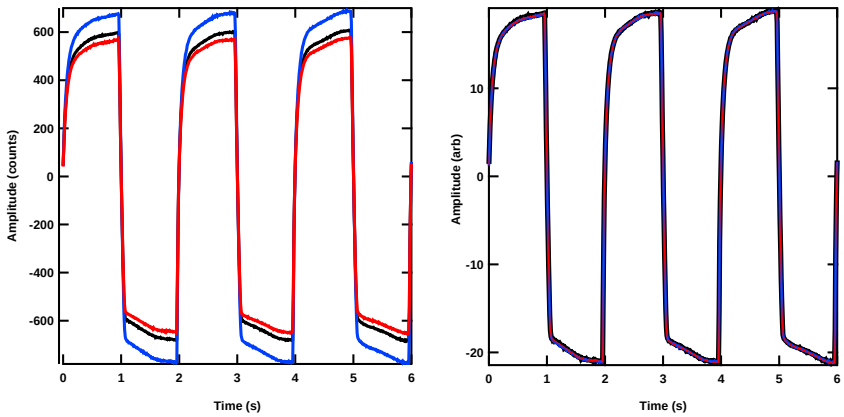

Figure 3.2 - Left: Raw time domain response of three detectors to the CAL pulse flashing with a 1 s period square wave. These time streams are fit to a digital square wave from the interface card which reads 1 when CAL is biased and 0 when it is off. Right: The same three pixels after being normalized by their individual gains.

any of the pixels towards the bottom of their transitions. When R_{TES} is comparable to R_S, most of the current flows through the TES and it is no longer voltage biased. This can produce instabilities which render the detector useless. Once all columns have been biased on their transitions, the receiver is sensitive to incoming radiation and is ready for observations.

3.3 Flat-Fielding the Array

The effects of intrinsic detector scatter are also evident in the gain distribution of the array. When producing images from an array it is essential to flat-field the gains by normalizing each detector by its response to a bright, stable source. To accomplish this, MUSTANG uses the internal calibrator (CAL) fixed to the Lyot stop, which provides uniform illumination of the array. At the start of each observing session, a 30 s file is taken with the CAL flashing with a square wave with a 1 s period and a 1 s duty cycle. The time responses to this source of three pixels are shown in Figure 3.2. The signal which drives the CAL (a 1.2 V_{pp} square wave) is fed into the digital interface card in the electronics

rack. The signal is digitized with a single bit (**0** = off, **1** = on) and archived at the same sampling rate as the detectors. To measure the gain of each pixel, a simple fit is performed. The function fitting the detector CAL response is simply an amplitude multiplied by the digital square wave. The amplitude is taken to be the gain of the detector. This process is repeated multiple times throughout an observing session to track fluctuations in the gain. On a typical night with low and stable sky opacity, the gain variation in an individual detector is on the order of 2%. The responses to CAL of three pixels after normalization is also shown in Figure 3.2.

3.4 Out-of-Focus Holography (OOF)

Once the detectors and SQUIDs are biased and their sensitivity is verified by CAL responses, out-of-focus (OOF) holography is performed. This technique, developed by the Green Bank precision telescope control system team led by Bojan Nikolic and Todd Hunter, is a method for measuring and correcting the large scale deformations of the primary mirror in real time. The method and algorithms implemented are described in detail in Nikolic et al. [2007]. The process consists of using MUSTANG to map the GBT beam pattern at several stages of focus. The de-focusing is introduced by varying the relative distance between the primary and secondary mirrors, or the local focus correction in the y-axis (LFCy). The entire process including measurement of beams, calculation of phase offsets and applying the calculated changes to the active surface configuration is completed within $\sim$15 minutes.

Three beam patterns are measured on a bright ($\sim$ 1 Jy) unresolved astronomical source with the LFCy set to the position nominally in focus, and with the LFCy set to $\sim$ 3 λ ($\sim$ 9 mm) on either side of focus. The resulting beam patterns are passed to a real time automated analysis which fits the asymmetric morphologies using the algorithm described

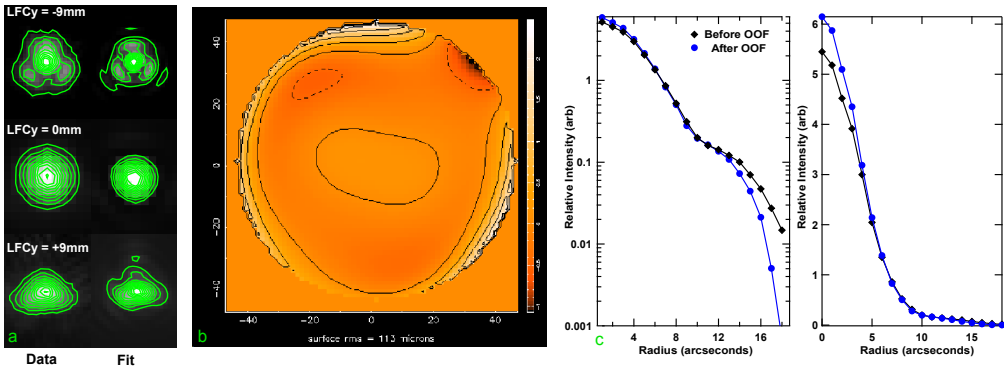

Figure 3.3 - A typical measurement of Out of Focus Holography (OOF). This process is used to measure and correct for large scale deformities in the shape of the GBT primary and is performed at the start of every observing run. MUSTANG beam patterns are measured with local focus corrections in the y axis (LFCy) nominally in focus and $\sim 3\lambda$ on either side of focus. The shapes of the patterns are fit and compared to those of an ideal telescope. The phase errors in the primary shape required to produce the difference between the ideal and best fit beams are calculated using the algorithm described in Nikolic et al. [2007]. Corrections to the active surface are then applied. a: Measured (left) and fit (right) MUSTANG beam patterns at the three LFCy positions. b: A reconstructed image of the large scale deformations in the GBT primary mirror. Axis are in units of meters and the color scale is in microns. c: Logarithmic (left) and linear (right) azimuthally averaged beam profiles before and after applying the corrections derived by the OOF process. In this case, the corrections have improved the main beam efficiency by $\sim 20\%$. This is visible in both the increased peak amplitude and the decreased power in the side-lobes at high radii.

in Nikolic et al. [2007]. An example case of a set of holography beams and their best fit models are shown in Figure 3.3a. The phase abberations of the primary mirror are parameterized by a linear combination of the first six orders of Zernicke's circle polynomials. This series of polynomials are by definition orthogonal on a unit disk. The phase offsets introduced by path length differences created by dish deformations required to produce the measured beam shapes are calculated. From this, a map of the deformations to the primary is produced. An example of a surface deformation map is shown in Figure 3.3b. The necessary modifications to the positions of actuators required to bring the shape of the primary back to the required paraboloid are calculated and applied. The efficiency of the solution is verified by making another beam map with the focus and active surface corrections applied. The response pattern before and after the OOF process are compared. Figure 3.3c shows an example of the effects of OOF on the main beam efficiency. The beams here are shown on both a logarithmic and linear scale to convey the increase in peak amplitude as well as the reduction of power in the first sidelobe.

3.5 Scan Strategies

Observations conducted with bolometers are inherently done in the time domain. Unlike optical CCD measurements, the vast majority of the photons received by TESs do not come from the celestial source. In the millimeter, the atmosphere is highly emissive and dominates the power incident on the detectors. It is therefore much more efficient to measure a differential signal of interest on top of the far more powerful emission from the atmosphere. The celestial signal is modulated into the time domain by scanning the telescope across the source. The speed at which the telescope scans determines the time it takes to cross the source and map the emission to a timestream. The atmosphere has temporal characteristics as well. It tends to fluctuate with a $1/f$ spectrum and therefore

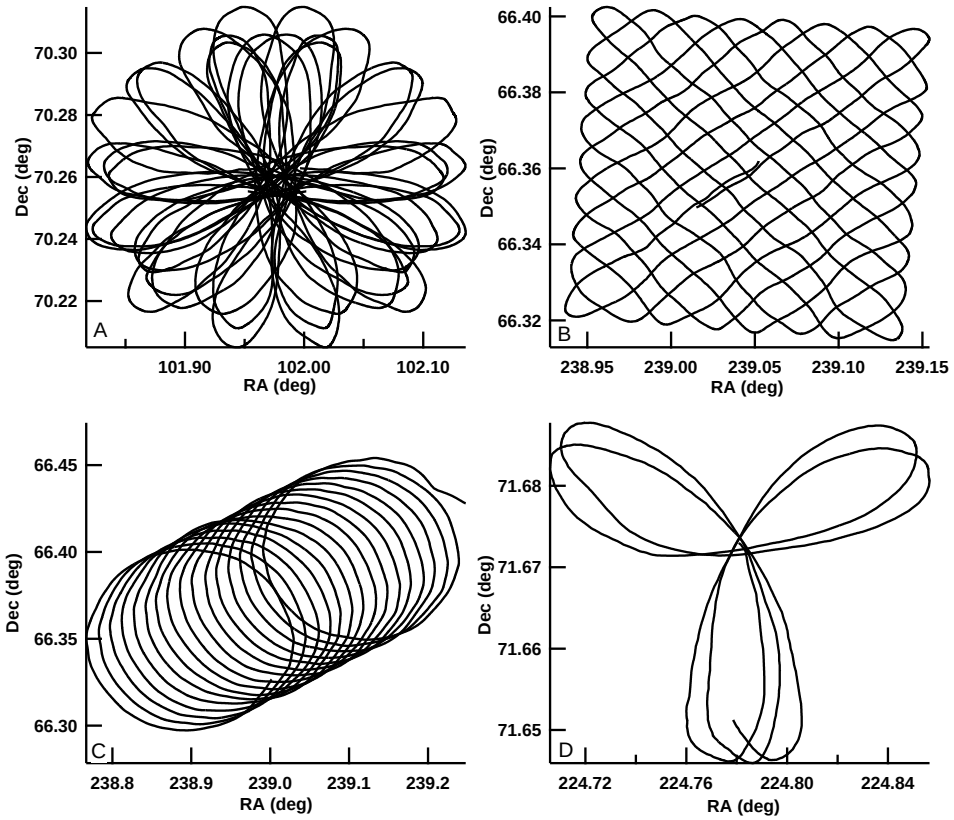

Figure 3.4 - GBT boresight trajectories for four scan types. A: The full lissajous daisy scan provides high telescope velocities towards the center but has non-uniform coverage. B: A Box scan provides uniform coverage and speed throughout the field of view but makes it difficult to move the telescope faster. C: The circle scan has near constant acceleration and high velocity. D: A quick daisy scan is useful for mapping bright calibrators and takes a very short amount of time to complete.

emits more power on slower timescales. It is therefore beneficial to scan the telescope with high velocity. This separates the signal from the atmosphere in the time domain and makes it easier to filter out the unwanted fluctuations.

For MUSTANG, the maximum scan speed is set by how fast the GBT can move. The telescope has a mass of over 7.7 million kg which limits the maximum scan velocity. Additionally, the off-axis optical design of the GBT has a free standing feedarm which holds the secondary mirror and receivers. Drastic acceleration and jerk in the telescope motion can cause the feedarm to wobble which produces pointing and focus problems. It is also beneficial to scan with a pattern which provides a high degree of cross-linking. This means that a given point on the sky will be scanned multiple visits at different time intervals to provide additional constraints on the fluctuations in the atmosphere.

The majority of all MUSTANG observations were carried out with one of several custom designed scan strategies. All of these were constructed to provide data with good cross-linking, high velocity, and minimal antenna acceleration. Examples of the GBT boresight trajectory during these scans are shown in Figure 3.4. Each has advantages and disadvantages and are used for optimal mapping on different types of sources. The most frequently used strategy for cluster mapping is the Lissajous daisy scan shown in Figure 3.4A. This has the advantage of achieving relatively high speeds in the central region ($2'.5 s^{-1}$ for a $2'.5$ radius scan). The resulting sky coverage is highly centrally weighted and will produce maps with radially increasing noise. When mapping clusters of galaxies with typical sizes of $\sim 5'$, pointing centers are tiled to expand the regions with deep coverage. The box scan shown in Figure 3.4B is more useful for mapping bright galactic highly extended regions. It is very uniform in both speed and coverage and provides cross linking on many timescales. The main disadvantages of this strategy is a slower maximum speed ($\sim 0'.4 s^{-1}$ for a $3'.0$ square box) which makes it more difficult to remove atmospheric fluctuations. The quick daisy featured in Figure 3.4D is very short and takes only 60 s to complete. This is utilized

predominantly for calibration point sources.

3.6 Integration and Calibration Procedure

Deep observations, such as those conducted to map clusters, require the integration of many hours of data, often taken over multiple observing sessions on different nights. It is therefore essential to track changes in the atmosphere and telescope gain. For each scientific target, a bright (> 0.5 Jy), compact, nearby ($<10^o$ from the science target) quasar is used as a secondary calibrator. Many radio loud quasars are known to exhibit time variability in their brightness. However, these flux fluctuations take place on timescales much longer than several hours. Therefore it is reasonable to assume the secondary calibrators are constant during a single observation session, but may vary from week to week. At least once per session, a planet or solar system object is observed and used as a primary calibrator and infer the flux of the secondary calibrator on a given night. The brightness temperature of planets varies with epoch as well, however, these variations are well studied and modeled. Planet fluxes and are taken from the models in Weiland et al. [2010].

For cluster observations, the secondary calibrator was mapped after every set of 2 Lissajous daisy scans ($\sim$30 minutes). This allows for a measurement of the beam shape and amplitude to be used later in image reconstruction. The beam maps are examined in real time. If significant ellipticity or amplitude decrease is observed, the OOF procedure is repeated. These frequent observations of point sources are also used to track offsets in telescope pointing, which go into image reconstruction.

Chapter 4

Data Reduction

The raw data from the MUSTANG detectors is purely in the time domain. The majority of the structure in a timestream is dominated not by astronomical signal, but by fluctuations from the atmosphere and internal loading conditions. A substantial amount of effort is required to separate out the signal of interest from the swamping foregrounds. To accomplish this task, a custom imaging algorithm implemented in the interactive data language (IDL) is used to produce maps from the time ordered bolometer data. The data is heavily filtered to remove atmospheric fluctuations prior to map making.

4.1 The Common Mode

The first step in data processing accounts for gain inhomogeneities across the detector array. The array is flat-fielded using the CAL scans taken throughout an observing session using the process described in Section 3.3. These data are also used to identify and mask unresponsive detectors (typically 10-15 out of 64). This accounts for the discrepancies in the gain of each detector, however, due to residual vibration coupling, detectors in the array have a varied range of noise properties and must be weighted individually by these characteristics.

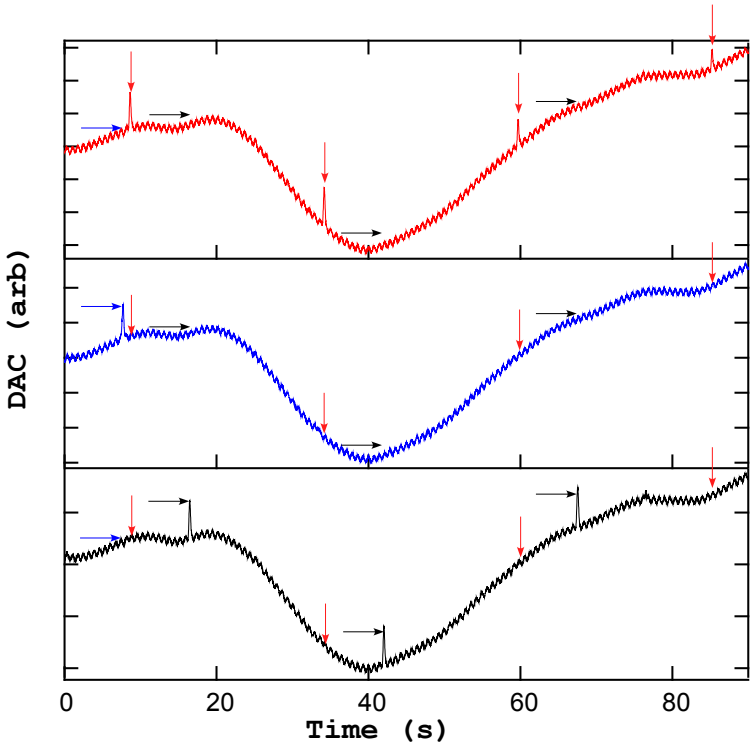

Figure 4.1 - Time ordered data from three pixels at separated locations on the array during a single daisy scan on a bright unresolved source. These data were taken during poor weather conditions which accentuates the effects of the atmosphere and is useful for illustration purposes. Each crossing of the source is marked with an arrow. The color of each arrow corresponds to the pixel which is scanning across the source at a given moment in time. The same atmospheric signal is seen in all pixels, this is manifested as the long timescale baseline fluctuations common to all three traces. Because the detectors are looking through the same atmosphere and different astronomy at a given instant, a common mode template which contains only long timescales will have no astronomical signal and can be used to remove the atmosphere. This technique is only valid in the approximation that the signal of interest is on angular scales smaller than the instantaneous field of view.

The ability to distinguish atmosphere from signal through the subtraction of a common mode is a distinct advantage of an array imager. The characteristic inhomogeneities in the optical loading from the sky (clouds) do not exhibit significant structure on angular scales comparable to the instantaneous FOV of MUSTANG. The characteristic timescale for temporal fluctuations in atmospheric loading is typically many seconds. When the telescope is scanned across a source, the atmosphere affects all detectors uniformly. If the celestial signal being mapped is on angular scales smaller than the FOV, the source will appear in different detectors at different times as the telescope is scanned. This phenomenon, illustrated in Figure 4.1, can be exploited to remove atmosphere by the generation of a common mode template. *For signals on angular scales smaller than the* $42''$ *instantaneous FOV, the atmosphere is common mode across the array and the signal is not.*

The common mode template is constructed from a weighted average of the time ordered data of all accepted detectors. To remove the celestial signal from the atmosphere model, it is low-pass filtered in Fourier space. This filtering requires a characteristic frequency to be defined at which all of the common mode signal is taken to be atmosphere. The template is then subtracted in the time domain from each detector after being scaled by the appropriate gain. The effectiveness of this filter relies on the assumption that the celestial signal is not common mode, which is valid only in the limit of compact sources. SZE signal from clusters can be smooth and often extend for many arcminutes on the sky and not well approximated in this assumption. Consequently, some smooth extended astronomical structure will be removed from the data along with the atmosphere. The effects of the low pass cutoff frequency choice are shown in Figure 4.2, where the same data are imaged with varied common mode filters. The source used for this illustration is the Orion nebula, discussed in detail in Section 6.1. It is extremely bright, with extended flux on the order of 1 Jy (4 orders of magnitude brighter than typical SZE signal) spanning several arcminutes on the sky. When high values of the cutoff frequency are used, the extended signal is removed.

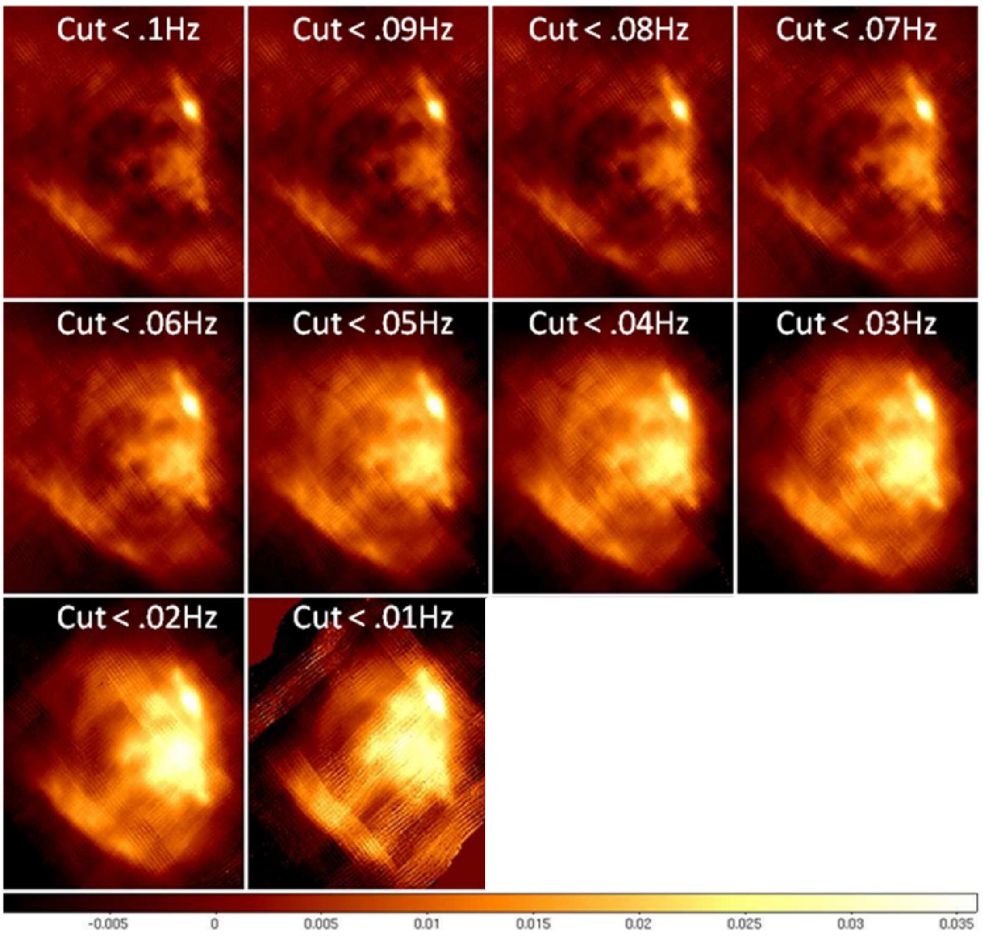

Figure 4.2 - Each image shows a map produced from a single scan on the Orion nebula. Each map was produced with a different characteristic cutoff frequency used to low-pass the common mode atmospheric template. When a high frequency is used, much of the astronomical signal is removed with the atmosphere. When a low frequency is used, not enough atmosphere is used and striping is visible.

When low values are used, the atmosphere permeates the reconstructed image. Therefore, to quantitatively understand a reconstructed image, it is essential to simulate and generate the angular transfer function of the imaging pipeline with the particular choice of filter used. After common mode filtering, a low-order polynomial is fit and subtracted from each timestream. This further removes the long timescale fluctuations in the data.

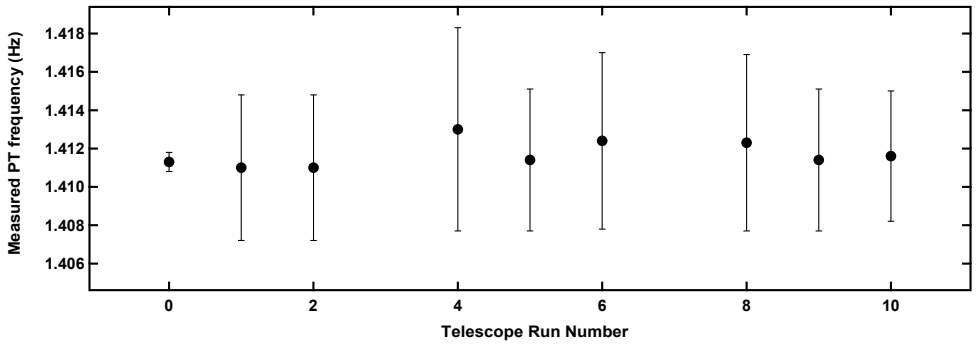

Figure 4.3 - The frequency of the oscillations in the detector data caused by thermal fluctuations of the PT is remarkably stable. Each data point represents the location of the peak around 1.4 Hz in a power spectrum of the time ordered bolometer data taken during a different observing session in the AGBT08A056 project. Run 0 corresponds to data taken in the laboratory which is a substantially longer scan (3000 s), allowing for high spectral resolution in the Fourier transform.

4.2 1.4 Hz Pulse Tube Fluctuations

The data all contain a coherent 1.4 Hz signal produced by fluctuations in optical load on the detectors caused by the thermal cycle of the PT. The signal is clearly visible in the time streams shown in Figure 4.1. This frequency is in the heart of the signal band expected from astronomical signals. Fortunately, it is well approximated by a sinusoid and can be removed efficiently in data processing. The frequency of the signal is remarkably stable at 1.411 Hz. Figure 4.3 shows redundant measurements of the frequency at which the power spectrum of all detectors peak in the $1-2$ Hz band. The majority of these spectra were taken from early science data with the receiver on the telescope spanning 8 observing runs separated by months. The spectral resolution in any power spectrum is determined by the length of contiguously sampled timestream used to make the measurement. On the telescope, scans are typically $\sim$100 s long. In each measurement the PT line is unresolved indicating its sinusoidal shape in real space. The line remains unresolved with laboratory data taken with 0.0005 Hz resolution, noted as Run 0 in Figure 4.3. The PT signal is removed from the timestreams by fitting a 1.411 Hz sine wave in the time domain to the

outputs of all detectors. In this fit, a phase and amplitude are floated while the frequency is fixed.

4.3 High Pass Filtering

To further remove uncorrelated low frequency noise in the data, a per-pixel high-pass filter is applied in Fourier space. This aggressive technique removes all low frequency spatial modes from the data indiscriminately. A characteristic frequency is defined at this stage as well. The filter is generated in Fourier space and is simply a step function smoothed with a moving average several times to avoid extensive ringing from sharp edges. This filtering will further affect the angular scales present in the reconstructed image.

Individual detector weights are computed based on the noise characteristics of each detector after the processing described above. This is used to create an effective exposure weight for each map pixel on the sky. After all of the above filtering, the time stream data are averaged using the appropriate weights and binned on a $2'' \times 2''$ grid in Right Ascension and Declination on the sky.

An example of a single MUSTANG timestream taken during a scan on a cluster is presented in Figure 4.4. This plot shows the same trace after each stage of filtering described in this chapter. Since the level of signal in a single scan on an SZE cluster is much smaller than the noise, after processing, the trace should appear as a featureless, homogenous noise distribution with no discernable baseline structure.

4.4 Parameter Space Optimization

The MUSTANG SZE images presented in this work have been optimized for peak signal to noise on the compact features of the clusters. As described above, there are two selectable

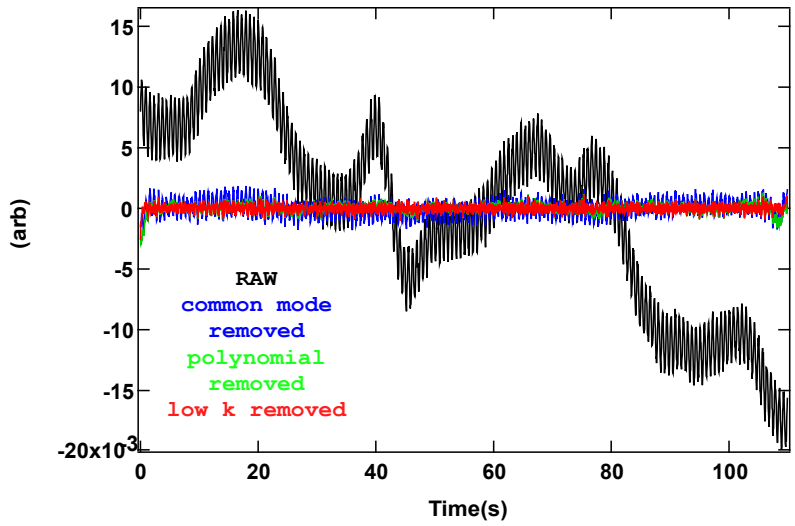

Figure 4.4 - Timestream of a single MUSTANG pixel on a cluster scan at various stages of filtering to remove atmospheric and other systematics. Data shown here were collected in relatively low quality weather to better illustrate the effects of the atmosphere. Black shows the raw timestream. The width of this trace is set entirely by the 1.4 Hz sinusoid created by thermal fluctuations in the PT. Blue shows the data after a low passed template of the common-mode of all pixels has been subtracted. Green is the timestream after a low order polynomial and template for the PT signal have been removed. Red shows the time stream after the final stage of filtering. A Fourier domain high pass filter which acts on each pixel independently.

filter parameters used in the imaging pipeline, one for the common mode template and the other for the per-detector high-pass. These selected frequencies correspond to spatial scales on the sky through the speed at which the signal is modulated by the telescope scan (usually $\sim 0.5'\mathrm{s}^{-1}$). The optimal filter for each object depends on the intrinsic structure of the source as well as the noise properties of the scans used in each observation. To determine the optimal filter for each map, parameter space is explored systematically by mapping each object with varied degrees of filtering. The peak signal-to-noise ratio (SNR) as a function of these two parameters is displayed in Figure 4.5. SNR decreases towards the top right of this figure because too much signal is being filtered out. It also decreases towards the lower left because too much atmosphere is allowed in the map. A single optimal value for each parameter is assumed for the entire data set on each cluster.

In a SNR calculation, the noise in each map is defined by the standard deviation of all map pixels in an off-source region free from obvious signal. To account for uneven exposure, the SNR is calculated using the map multiplied by the square root of the weight map. For this reason, there is no simple conversion from a flux scale to significance (Jy/σ), this number varies depending on the location of a feature in the map.

4.5 The Transfer Function

The necessary filtering steps described above result in an attenuation of flux in the recovered map. The magnitude of this attenuation depends strongly on angular scale. Typically, structure larger than the instantaneous FOV is attenuated, and by $\sim 100''$ is less than half the amplitude of the signal within the instantaneous field of view. The angular transfer function for each object mapped is calculated using the specific scans and filter parameters selected to produce the map. When estimating the flux in a map or quantitatively comparing observational data to model fits, it is essential to correct for the

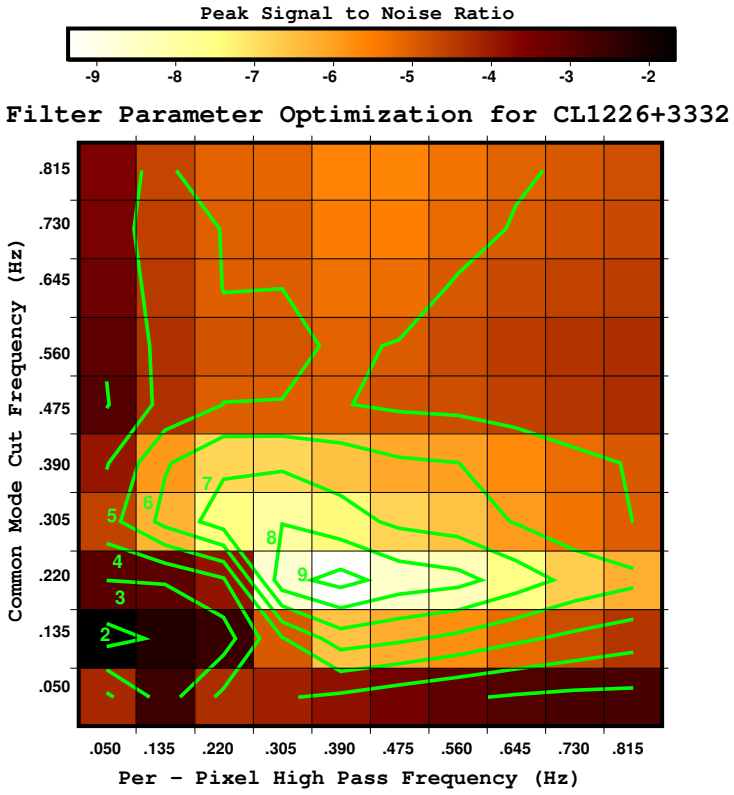

Figure 4.5 - Parameter space optimization for filter variables. For illustration purposes, the dataset obtained on CL1226+3332 is used here. The color-scale of each cell represents the peak signal to noise ratio (SNR) in the central region for a map produced using the filter parameter combination demarcated by the two axes. SNR decreases to the lower left as not enough atmosphere is removed. It also decreases to the upper right of this plot as aggressive filtering removes signal along with the atmosphere. The optimal map is chosen to be at the peak of this plot.

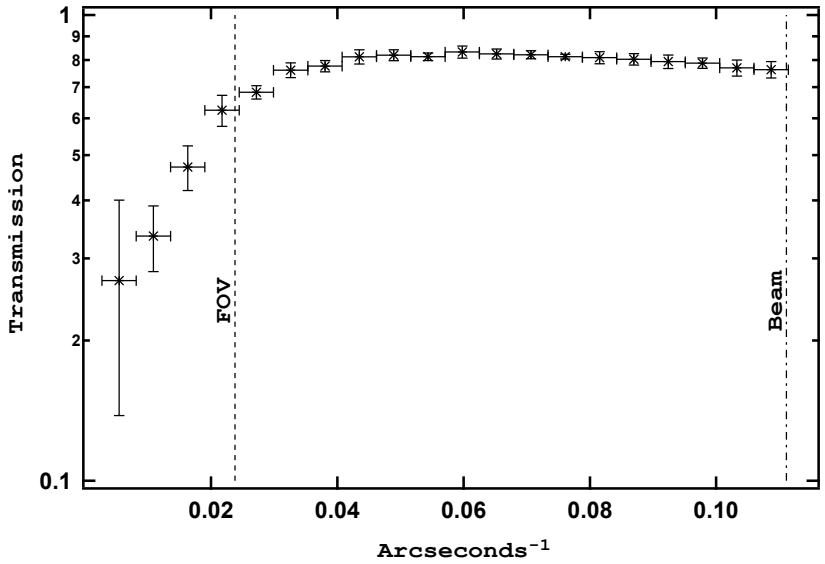

Figure 4.6 - The angular transfer function for CL1226+3332. The transfer function was created by generating mock sky signals with equal power on all spatial scales, translating the signal into timestreams through the actual scans used for the observations, and passing the data through the reduction pipeline. The transfer function is defined as the ratio of power spectrum of the input map to the power spectrum of the output map. Error bars were determined by the standard deviation of each angular bin in 10 realizations of random skies.

effects of this transfer function.

The transfer function is generated by passing randomized sky structure with equal power on all spatial scales through simulated observing software which produces time ordered data for a set of scans. Those timestreams are then processed with the same filtering as is done on the real data and maps of the given instance of randomized sky are output. The transfer function is defined as the ratio in Fourier space of the power spectrum of the reconstructed image to the power spectrum of the input map. An example of a transfer function, as calculated for the scans and integration on CL1226, is given in Figure 4.6.

Table 4.1. Archival *Chandra* Data

Cluster	Time (ksec)	ObsIds
Abell 1835	222	495, 496, 6880 6881, 7370
MACS J0744.8+3927	90	3197, 3585, 6111
CL J1226.9+3332	74	3810, 5014, 932

4.6 *Chandra* Data Reduction

Archival *Chandra* data presented in this thesis were reduced using CIAO version 4.2 and calibration database 4.2.0. Starting with the level 1 events file, standard corrections were applied along with light curve filtering and other standard processing [for reduction details see, Reese et al., 2010]. Images were made in full resolution ($0\farcs492$ pixels) and exposure maps computed at 1 keV. When merging data from separate observations, images and exposure maps from each data set were combined and a wavelet based source detector was used on the combined image and exposure map to find and generate a list of potential point sources. The list is examined and adjusted by eye and used for the point source mask. A summary of the archival *Chandra* data used in this thesis is presented in Table 4.1.

Chapter 5

Commissioning

5.1 Installation on the GBT

Over four seasons of operation with several installations per year, the process of interfacing MUSTANG with the GBT has been streamlined and can now be accomplished within several hours. The process is outlined below.

1. In the week before installation, the receiver is cooled down in the Jansky lab at Green Bank. After all systems are confirmed to be operating efficiently, the receiver is deemed ready and will is placed on standby until the next available GBT maintenance day.

2. On the morning of installation, the receiver is disconnected from the compressor in the Jansky lab and begins to warm slowly. All electronics are shut down and sealed in the RFI-tight crate.

3. The receiver and electronics rack are transported to the telescope.

4. Once at the base of the GBT, the cryostat and electronics rack are separately hoisted up to a platform at the base of the feedarm below the dish on the tipping structure.

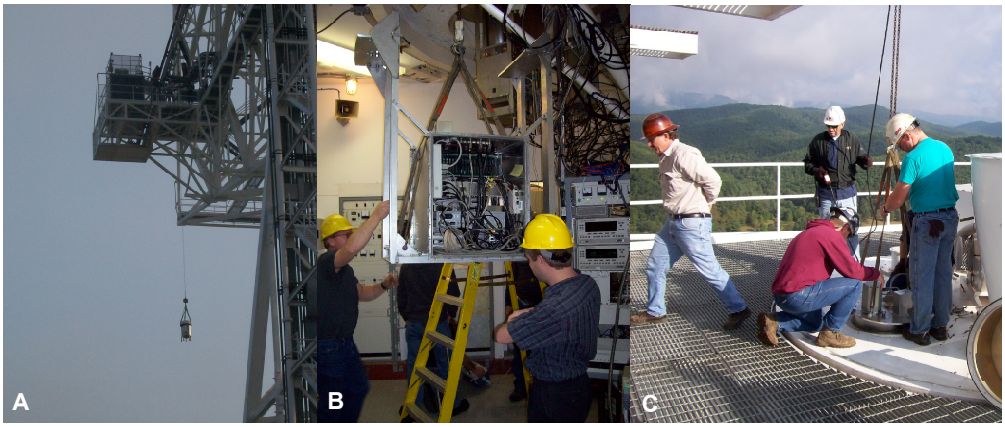

Figure 5.1 - Photographs of the process of installing MUSTANG on the GBT. A: The cold receiver is hoisted up to the feedarm elevator on the tipping structure. From there, it is placed on a cart with pneumatic tires and taken up to the receiver cabin in the feedarm elevator. B: The electronics crate is lifted by a hoist on top of the receiver cabin and bolted to the rotating turret at the Gregorian focus. C: The receiver is lowered into its slot in the roof of the receiver cabin on top of the rotating turret.

There they are placed on carts with pneumatic tires. A photograph of the cryostat being hoisted to this level is shown in Figure 5.1A.

5. The receiver and electronics crate are taken on the feedarm elevator. The electronics rack is brought into the receiver cabin and the cryostat up an additional level to the roof of the cabin.

6. The slot in the roof of the receiver cabin is opened. The GBT is equipped with another hoist above the Gregorian focus. The electronics rack is lifted using this hoist inside the cabin and bolted to the ceiling of the turret. A photograph of this step is shown in Figure 5.1B. Once the rack is fixed, power to the crate is connected and the control computer is booted up. A single fiber connects the control computer to the GBT network which will carry all archived data.

7. Once on the roof of the receiver cabin, the donut shield to the lid of the cryostat is removed. At this stage it is essential to ensure the RFI and weather seal gaskets underneath the lip of the cryostat are replaced and properly fitted. The cryostat is

then lowered into the turret with the hoist. The appropriate clocking of the cryostat is ensured with two pins fixed to the turret ceiling. A photograph of MUSTANG being lowered into the turret is shown in Figure 5.1C.

8. With the receiver held down only by gravity, the helium lines which connect the PT to the compressor 400 ft below at the base of the telescope are connected and the receiver begins to cool back down.

9. The coaxial cables and command fiber which connect the cards in the electronics crate to the warm tower are routed through an RFI tight conduit which feeds through the lid of the cryostat. Once all connections are made, the system is activated to verify multiplexing capabilities and data readout.

10. After it has been determined that the system is functioning, the donut is lowered over the cryostat taking care to hook up a tube which provides compressed dry air to the space between the vacuum window and Goretex weather shield. This prevents condensation on the vacuum window.

11. The cryostat is bolted to the turret roof and additional weather sealing caulk is applied. In the cabin, the RFI tight electronics rack is sealed. At the end of the process, the only connections which interface the receiver to the telescope system are the AC 110 V source, the cryogenic hoses and a single fiber to carry out the data.

5.2 Instrument Improvements

The MUSTANG receiver was first installed on the GBT in the fall of 2006. First light was achieved on September, 26, 2006 when Saturn was mapped. The resulting image, signed by the commissioning team consisting of Phil Korngut, Mark Devlin, Simon Dicker

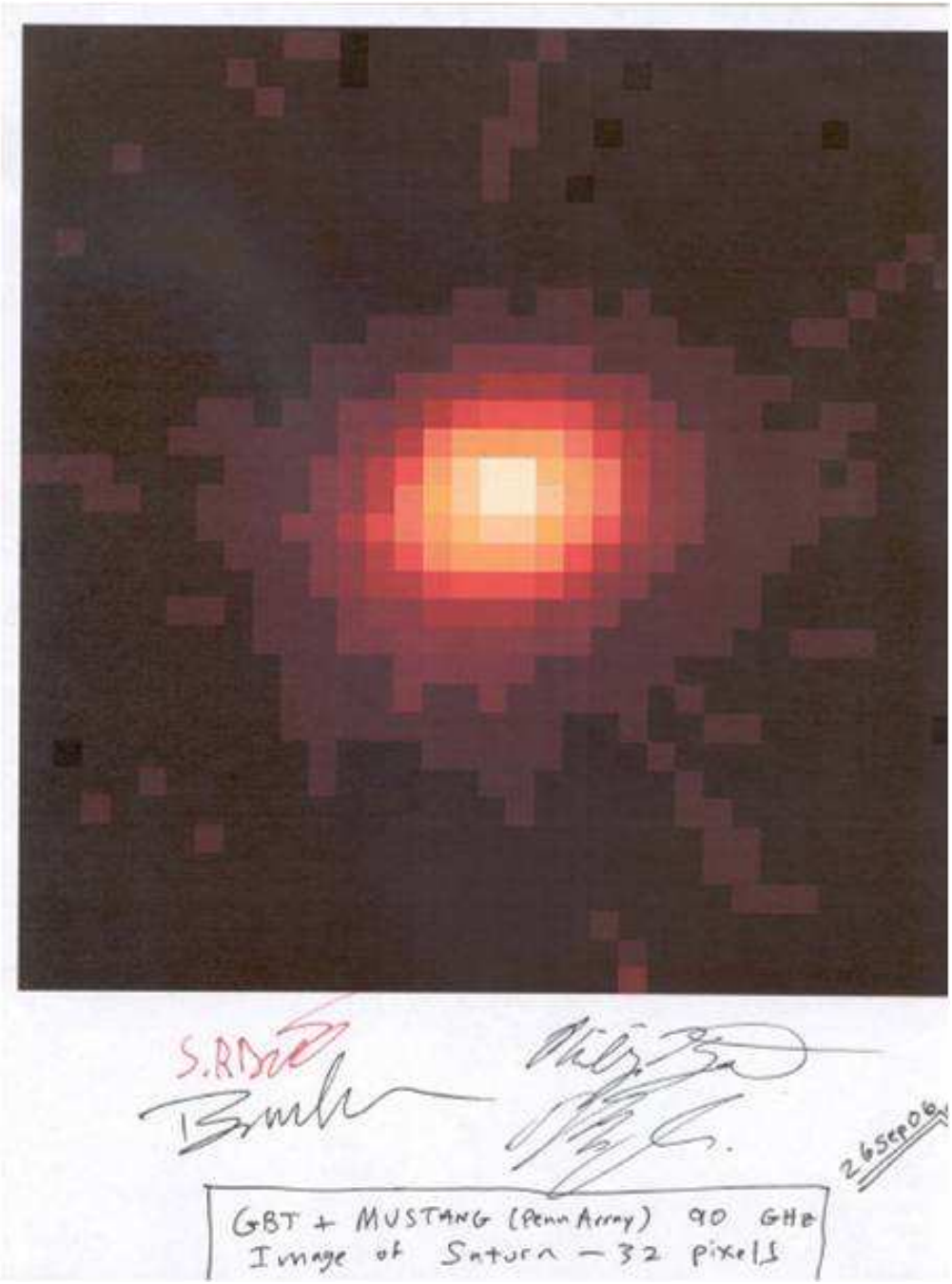

Figure 5.2 - MUSTANG's first light image of Saturn, taken on September 26th, 2006, my 23rd birthday. Included are the signitures of the commissioning team, Simon Dicker, Brian Mason, Phil Korngut and Mark Devlin.

and Brian Mason, is shown in Figure 5.2. This first season was considered highly successful because the receiver demonstrated full systems integration and functionality. The processes of focusing the telescope, scanning, and crude map making were developed and implemented. However, the sensitivity was drastically limited due to several contributing factors.

1. The noise of the detectors was completely dominated by excess $1/f$ fluctuations discussed in Section 2.5. This consisted of uncorrelated sharp telegraph noise with orders of magnitude more power than radiation from interesting celestial sources provide.

2. The panel alignment of the GBT primary yielded a surface of 390 μm RMS. This resulted in a very low ($\sim 10\%$) main beam efficiency.

3. The bandpass was relatively narrow, 86 GHz to 94 GHz which resulted in less power from the source reaching the focal plane. This was designed to reduce loading from the atmospheric emission lines at the edges of the bandpass. However, since the receiver was not photon noise limited, this proved unnecessarily narrow.

4. The reimaging optics were designed such that the detectors were spaced by 0.5 $f\lambda$. This was intended to provide instantaneous Nyquist sampling of the sky. However, since the sky is modulated by scanning the telescope (see Section 3.5), a fully sampled FOV is not required.

The MUSTANG receiver is not generally used in the months spanning May and October due to poor photometric conditions in West Virginia in the summer. During the off-seasons of the three years between May 2007 and October 2010, modifications were made to the telescope and receiver which drastically improved the sensitivity. The solutions to the above problems are stated below.

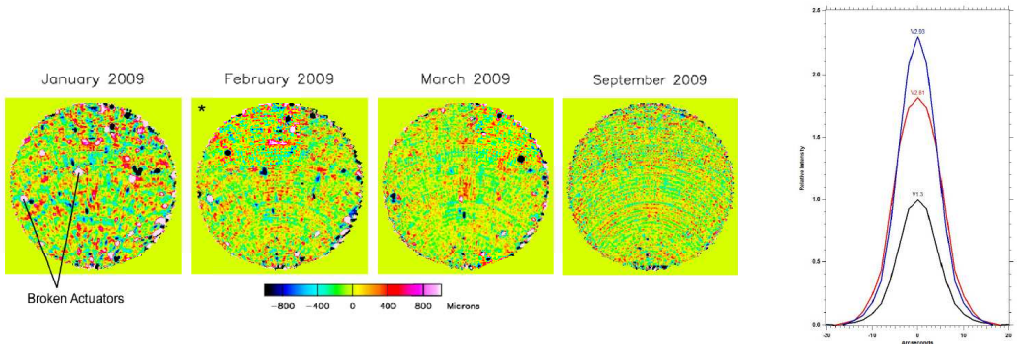

Figure 5.3 - Left: Maps of the irregularities on the GBT surface made from January 2009 through September 2009. The initial map, on the left, has an RMS of 390 μm while the latest map, on the right, has an RMS of 220 μm. Figure courtesy of Todd Hunter. Right: The telescope gain measured by MUSTANG with the initial 390 μm Ruze-equivalent RMS surface (black), intermediate versions of the surface with 315 μm RMS (red), and 295 μm RMS surface (blue)

1. The $1/f$ noise in the detector timestreams was identified to be caused by the coupling of microphonic vibrations, predominantly caused by the PT. By mechanically isolating all thermal links between the PT and cryostat, the noise was removed from the data. The characteristics and mitigation of this noise is discussed in detail in Section 2.5.

2. The precision telescope control system team at Green Bank led an effort to achieve a dramatic improvement to the accuracy of the primary mirror. By iterating with increasingly accurate models of the small scale fluctuations in panel alignment as measured with phase coherent holography, the efficiency of the GBT primary was vastly improved. As MUSTANG is the highest frequency receiver on the telescope it is the most sensitive to improved surface accuracy. It was therefore used to verify the improvements. Figure 5.3 shows surface maps from phase coherent holography at various stages of alignment. Also shown are measurements of a bright celestial source, with several versions of the active surface configurations. The gain in sensitivity is obvious and has resulted in an improvement of close to a factor of 4 in sensitivity.

3. After the commissioning run of 2006, collaborators at Cardiff University fabricated a new bandpass filter. This widened the range of frequencies accessible to MUSTANG to 81 GHz to 99 GHz. This increases the power available from a given source.

4. The original design of the reimaging optics had the detectors spaced at 0.5 fλ. This was done to ensure that the instantaneous FOV was Nyquist sampled at a given instant. At the time of design, the detectors had not yet been fabricated and were expected to have NEPs be below the photon noise limit. If a receiver is not detector noise dominated, spreading the power from a single beam over multiple pixels does not reduce the sensitivity. However, it became clear after testing that the detector NEPs were significantly higher than expected and were far greater than the photon noise limit. Therefore, to increase the power on a single pixel, modifications to the cold optics tube were made to increase the detector spacing to 0.62 fλ. This was implemented by replacing the final HDPE lens with a nearly hemispherical lens which had a much faster focus. This also required decreasing the distance between the array and final optic, implemented by designing a new, shorter, 300 mK kevlar suspension. This resulted in a sensitivity improvement by a factor of $(0.62/0.50)^2 = 1.54$. The altered optical design is shown in Figure 2.6.

Chapter 6

Early Science Results

6.1 The Orion Nebula

6.1.1 Target Selection

The first astrophysical measurements carried out with the MUSTANG receiver targeted the bright Huygens region in the star-forming Orion nebula, M42. Observations of high mass star-forming regions are well matched to MUSTANG capabilities as they are bright in both free-free emission from the ionized inter-stellar medium, as well as thermal emission from dust in the molecular clouds. The Orion nebula was the ideal first target for MUSTANG early science for several reasons:

- Located only 437±19 pc away from the Sun [Hirota et al., 2007], it is extremely bright and extended on the sky with peak flux at the $\sim$ 2 Jy level and extent over $\sim$ 50 square arcminutes. It was important that the early science results to have high signal to noise and spatial dynamic range. The measurement can be used to confirm MUSTANG's sensitivity and image fidelity.

- It has been well studied across the electromagnetic spectrum and a large body of archival multi-wavelength data is publicly available (See O'dell [2001] for a com-

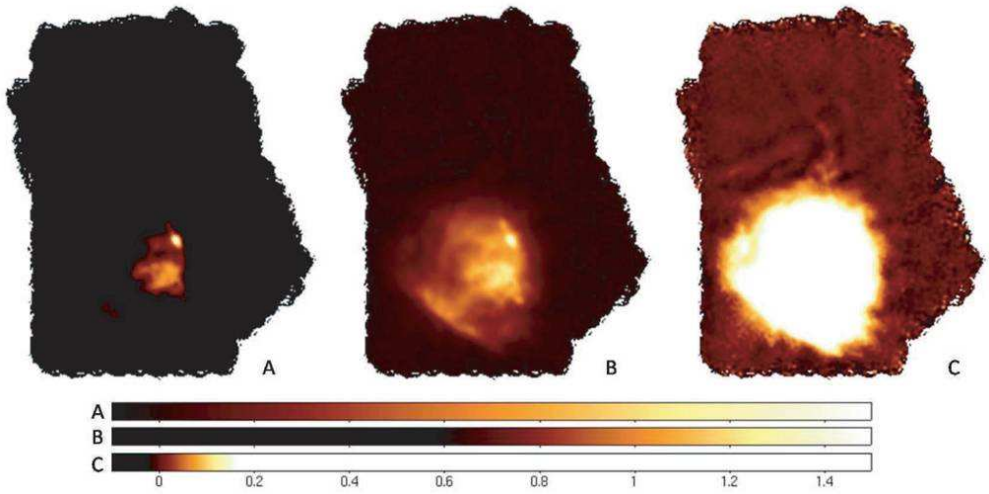

Figure 6.1 - MUSTANG image of the Orion nebula on 3 color scales to show the dynamic range of the measurement. The emission at 90 GHz from this region is a combination of thermal radiation from the molecular cloud OMC-1 and free-free from the ionized HII region.

prehensive review). Comparison of feature morphology with maps from well vetted instruments such as the Very Large Array (VLA) provides verification of observation and data reduction capabilities.

- There have been no high angular resolution measurements of this object published in the literature at ~ 3 mm. While the object is well studied, MUSTANG observations still provide something new.

- A simultaneous measurement of free-free and thermal emission is quite unique to this wavelength regime. This allows simultaneous access to measurements of the emission measure of the photo-ionized plasma and dust temperature and emissivity index in the star forming cores of the molecular cloud.

6.1.2 Orion Morphology

The MUSTANG map of M42 is approximately $5' \times 9'$ and is the result of 5.6 hours of on-source integration. The observations were done predominantly using the box scan

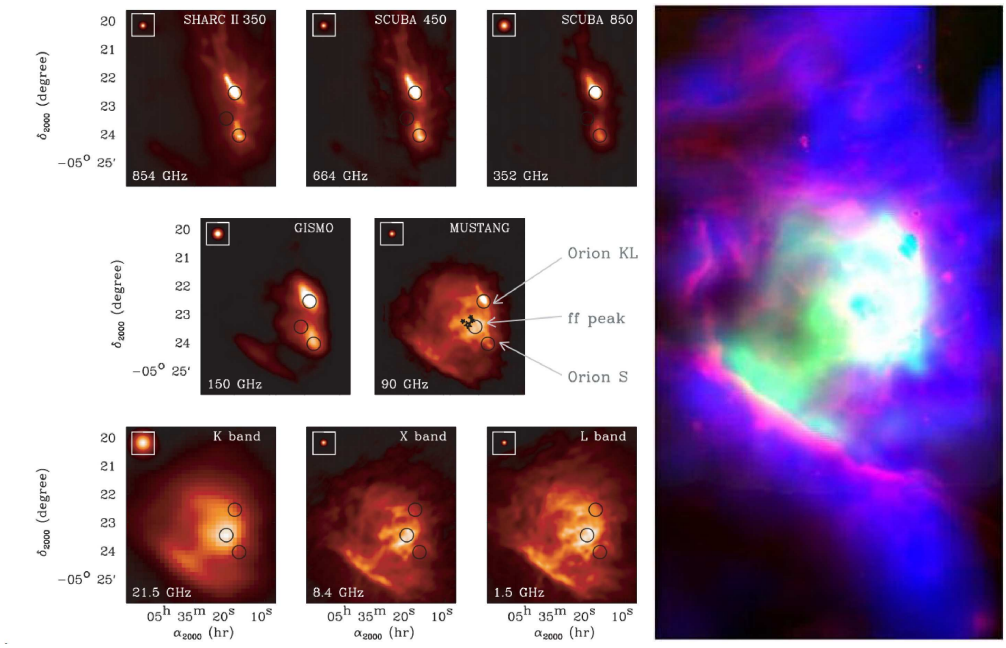

Figure 6.2 - Left:Maps of M42/OMC-1 from the radio to submm. All datasets are displayed with their nominal resolution. Each map has an inset that shows a Gaussian approximation of the relevant beam. The 30 ″ circles show the areas used for spectral fitting on Orion-KL, Orion-S and the free-free emission peak. The stars on the MUSTANG map show the locations of the Trapezium with the larger one representing Θ^1 Ori C. This figure appears in Dicker et al. [2009]. Right:Multiwavelength composite image of the Orion nebula and OMC-1. *Green* : MUSTANG 3.3 mm which traces predominantly the free-free radiation from the HII region created by the ionizing UV photons emitted by young hot stars in the Trapezium. Dust emission also contributes to the signal. *Blue* : SCUBA 850 μm image which traces the thermal dust emission from the molecular cloud OMC-1. *Red* : IRAC 8 μm image from the *Spitzer* space telescope. This is dominated by spectral line emission from Polycyclic Aromatic Hydrocarbons (PAHs) in the photo-dissociative region.

strategy described in Section 3.5 which produced a relatively uniform coverage across the field. This resulted in a final map RMS of 2.8 mJy bm^{-1}. The map is shown in Figure 6.1 on three linear color scales to show the dynamic range of the measurement which spans three orders of magnitude. The image contains flux in nearly equal parts from the background molecular cloud OMC-1 and the HII region ionized by UV radiation from a group of OB stars known as the Trapezium.

This result is featured in Dicker et al. [2009], where the MUSTANG map is analyzed with a suite of multi-wavelength data spanning from the submm to the radio. The morphology of

the region at each wavelength is shown in Figure 6.2. At the shorter submm wavelengths, the emission is entirely dominated by thermal dust radiation from the molecular cloud OMC-1. The SHARCII (350 μm) and SCUBA (450 μm and 850 μm) maps are doubly peaked, which show the two bright star forming cores, Orion KL/BN and Orion S. At the longer radio wavelengths, the emission is entirely dominated by free-free emission from the H II region. The MUSTANG map is a linear combination of the two phenomena.

By combining the MUSTANG data with 1.4, 8, and 21 GHz radio data from the VLA and GBT, an estimate of the emission measure (EM) averaged electron temperature of $T_e = 11376 \pm 1050$ K was obtained by an original method relating free-free emission intensities at optically thin and optically thick frequencies. Combining Infrared Space Observatory-longwavelength spectrometer (ISO-LWS) data with the MUSTANG data, a new estimate of the dust temperature and spectral emissivity index within the 80″ ISO-LWS beam toward Orion KL/BN, $T_d = 42 \pm 3$ K and $\beta_d = 1.3 \pm 0.1$ were derived. With a model consisting of only free-free and thermal dust emission, data taken at frequencies from 1.5 GHz to 854 GHz were simultaneously fit.

6.2 Spectral Aging in AGN

Other bright extended objects were mapped in the first two seasons of MUSTANG observations. These included the measurement of spatially resolved synchrotron emission from the jets along two active galactic nuclei (AGN), Hydra A and M87. The MUSTANG images of these objects, shown on top of the stellar optical emission are given in Figure 6.3. By combining these data with lower frequency measurements from the VLA, spectral indices were fit at several locations along the jets. By measuring the synchrotron spectrum out to 90 GHz, energy losses in the relativistic population of radiating particles should be apparent, manifested as a steepening of the spectral index along the jet. M87 showed only

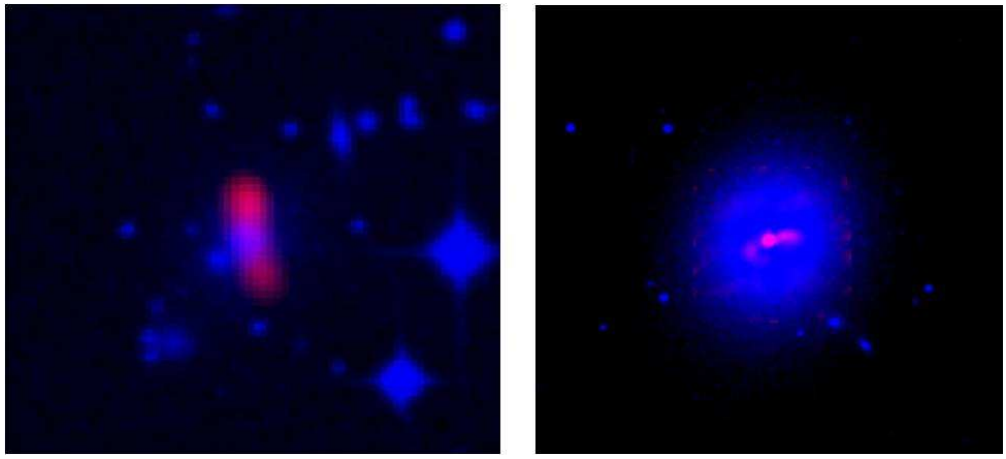

Figure 6.3 - MUSTANG observations of AGN. *Red* : MUSTANG data tracing the synchrotron emission along the jets. *Blue* : Archival optical data from the Palomar Schmidt 48 in. tracing stellar emission in the galaxies. Analysis of the spectral aging of relativistic electrons along the jets are given in Cotton et al. [2009].

weak evidence for steepening of the spectrum along the jet suggesting either re-acceleration of the relativistic particles in the jet or insufficient losses to affect the spectrum at 90 GHz. The jets in Hydra A show strong steepening as they move from the nucleus suggesting unbalanced losses of the higher energy relativistic particles. The difference between these two sources may be accounted for by the lengths over which the jets are observable, 2 kpc for M87 and 45 kpc for Hydra A. These conclusions are derived from work featured in Cotton et al. [2009] where the spectra analysis can be found.

6.3 Other Bright Extended Observations

In the process of commissioning the instrument, several other bright extended millimeter sources were imaged and are displayed in Figure 6.4. These maps were made primarily for verification of imaging capabilities.

- **NGC 2024** : top left of Figure 6.4. This bright high mass star forming region is located several degrees away from M42 in the Orion star forming complex. Like

M42, the 3.3 mm emission is a combination of free-free and thermal dust from the background molecular cloud. The compact objects seen in a vertical arrangement are dusty cores in the molecular cloud.

- **The Moon** : top right of Figure 6.4. Perhaps the brightest celestial object in the sky (save the Sun), this image features a section of the Earth's Moon seen in thermal emission at 3.3 mm. Shadows and craters are clearly visible in the image. When mapping the Moon with MUSTANG it was essential to scan without the FOV leaving the surface of the moon as the difference in loading from the Moon to the background far exceeded the dynamic range of the feedback electronics. The Moon was also a good test for commissioning as it moves across the sky much faster than other sources and allows for testing the ephemeris tracking capabilities of the telescope and imaging software.

- **Crab Nebula** : bottom left of Figure 6.4. The Crab nebula is a nearby supernova remnant from a type II explosion. It harbors a pulsar in the center and is used extensively as a calibrator for high energy astrophysics such as gamma rays. The emission at 90 GHz is entirely synchrotron. It is believed to be the remnant from a supernova explosion in the year 1054 A.D. observable by the naked human eye and described by Chinese astronomers. This data is featured in Arendt et al. [2011].

- **Cassiopeia A**: bottom right of Figure 6.4. Cassiopeia A is also a nearby supernova remnant. Located at high declination and extremely bright in the radio, it was historically used as a radio calibrator.

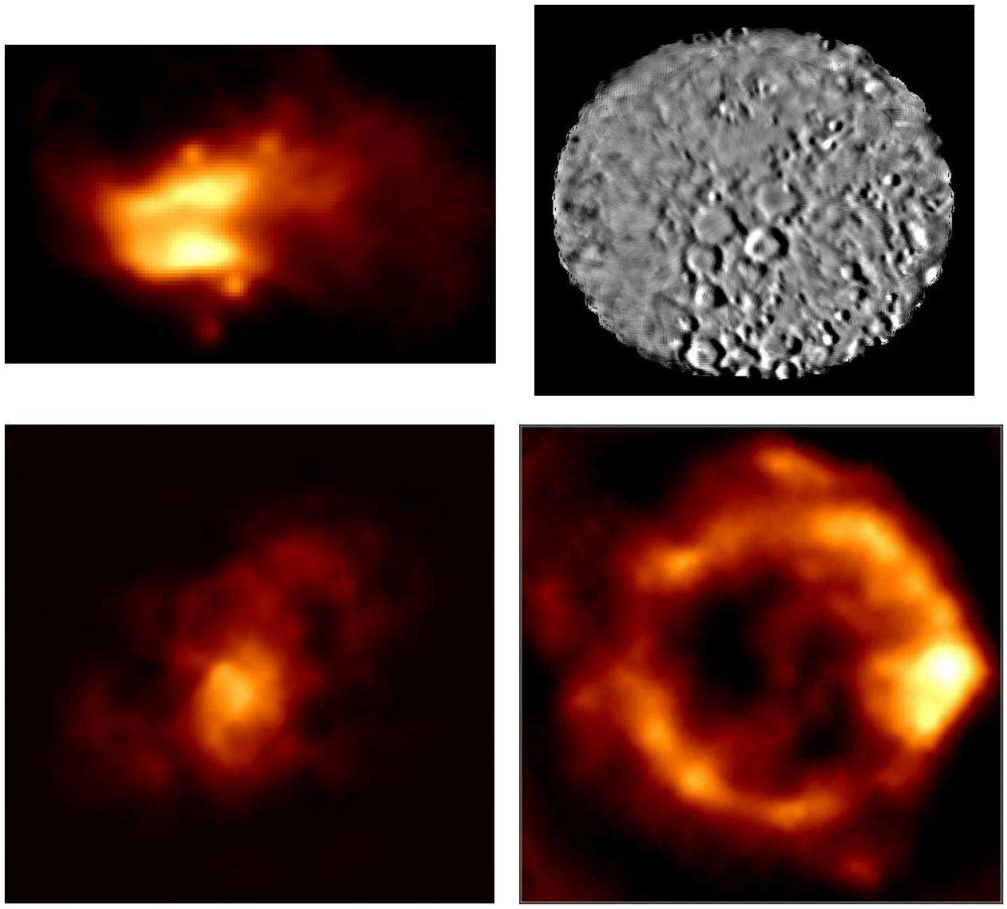

Figure 6.4 - Examples of maps made with MUSTANG during commissioning science observations. Top left: NGC2024, otherwise known as the "Flame nebula". Like Orion, it contains emission from both free-free and thermal dust radiation. There are three compact cores in the molecular cloud visible. Top right: A small section of the moon seen in thermal emission. Bottom left: The Crab nebula supernova remnant. The emission is dominated by synchrotron. Bottom right: Synchrotron radiation from the Cassiopeia A supernova remnant.

Chapter 7

RX J1347-1145 (z = 0.45)

7.1 Introduction

The rich cluster RXJ1347-1145 ($z = 0.45$) is the most X-ray luminous galaxy cluster known [Schindler et al., 1997, Allen et al., 2002] and has been the object of extensive study at radio, millimeter, submillimeter, optical and X-ray wavelengths [Kitayama et al., 2004, Komatsu et al., 2001, Gitti et al., 2007, Allen et al., 2002, Schindler et al., 1997, Pointecouteau et al., 1999, Ota et al., 2008, Cohen and Kneib, 2002, Bradač et al., 2008, Miranda et al., 2008]. Discovered in the ROSAT All-Sky Survey, RXJ1347-1145 was originally thought to be a dynamically old, relaxed system [Schindler et al., 1997] based on its smooth, strongly-peaked X-ray morphology— a prototypical relaxed "cooling-flow" cluster. The NOBA 7 bolometer system on the 45-meter Nobeyama telescope [Kitayama et al., 2004, Komatsu et al., 2001] has made high-resolution observations (13″ FWHM, smoothed to $\sim 19''$ in the presented map) of the Sunyaev-Zel'dovich effect (SZE) at 150 GHz which indicate a strong enhancement of the SZ effect 20″ (170 kpc) to the south-east of the peak of the X-ray emission, however. Hints of this asymmetry had been seen in earlier, lower resolution measurements with the Diabolo 2.1 mm photometer on the IRAM 30-m [Pointecouteau et al., 1999]. The enhancement has been interpreted as being due to

hot ($T_e > 20\,\mathrm{keV}$) gas which is more difficult to detect using X-rays than cooler gas is, owing to the lower responsivities of imaging X-ray telescopes such as Chandra and XMM at energies above $\sim 10\,\mathrm{keV}$. In contrast, the SZE intensity is proportional to T_e up to arbitrarily high temperatures, aside from relativistic corrections which are weak at 90 GHz, so such hot gas stands out. The feature is consistent with the presence of a large substructure of gas in the intra-cluster medium (ICM) shock-heated by a merger; this interpretation has been supported by more recent observations [e.g. Allen et al., 2002, Ota et al., 2008]. *Thus, rather than being an example of a hydrostatic, relaxed system, high-resolution SZE observations suggest that the observed properties of the ICM in RXJ1347-1145 are strongly affected by an ongoing merger.* This is a striking cautionary tale for ongoing blind SZE surveys [Carlstrom et al., 2002a], for which useful X-ray data will be difficult or impossible to obtain for many high-z systems.

Reports [Komatsu et al., 2001, Pointecouteau et al., 2001, Kitayama et al., 2004] of a strong enhancement of the SZE away from the cluster center are based on relatively low-resolution images compared to the size of the offsets and features involved. SZE images at lower frequencies also show show substantial offsets between the peak of X-ray and SZE emission; for instance, the 21 GHz [Komatsu et al., 2001] and SZE peak is $\sim 20''$ to the SE of the X-ray peak, and the 30 GHz [Reese et al., 2002] SZE peak is $\sim 13''$ to the SE of the X-ray peak. The situation is further complicated by the presence of a radio source in the center of the cluster. We have sought to test these claims, and to begin to untangle the astrophysics of this interesting system, with higher resolution imaging at a complementary frequency. The data presented in this chapter were originally published in Mason et al. [2010] and contain the highest angular resolution image of the SZE yet made.

7.2 Beam Characterization

Imaging diffuse, extended structure requires a good understanding of the instrument and telescope beam response on the sky. To achieve this we collected numerous beam maps through our observing runs, including several deep beammaps on bright (5 Jy or more) sources. After applying the Out-of-Focus holography corrections to the aperture the beam results were repeatable; Figure 7.1 shows the radial beam profile from maps of a bright source (3C279) collected on two occasions. We find a significant error beam concentrated around the main lobe which increases the beam volume from 87 arcsec^2 (for the core component only) to 145 arcsec^2. We attribute this beam to residual medium and small scale phase errors on the primary aperture. The beam shape and volume is taken into account when comparing to model predictions. By way of comparison, Figure 7.1 also shows the profile of the beam determined from the radio source in the center of RXJ1347-1145. Since the SZ map has been smoothed, the apparent beam is slightly broader, but allowing for this, still consistent with the beam determined on 3C279.

7.3 RXJ1347 Map

The final map of RXJ1347, smoothed by a 4″ FWHM Gaussian, is shown in Figure 7.2, along with the difference between the two individual maps. It shows a strong, clear SZE decrement, well separated from the central point source and consistent with the level expected from the Kitayama et al. [2004, hereafter K04] 150 GHz measurement. The right hand panel shows the image formed by differencing the images of the two individual nights. By computing the RMS in a fiducial region in the center of the difference image (and scaling down by a factor of 2 to account for the differencing and the shorter integration times) we estimate a map-center image noise of ~ 0.3 mJy/bm (rms). The noise level in regions

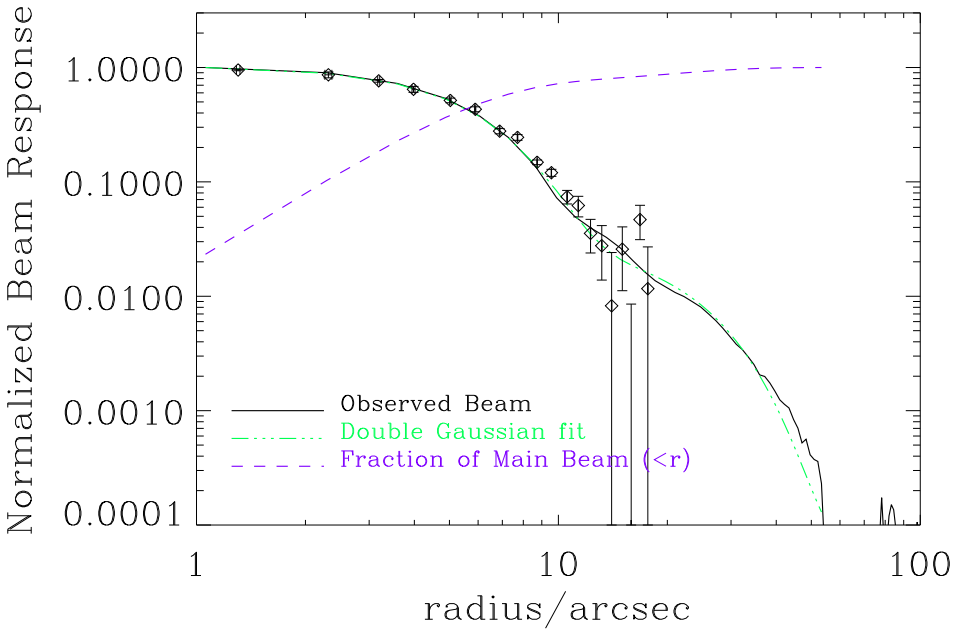

Figure 7.1 MUSTANG+GBT beams determined from observations of 3C279. The green dash triple-dot line shows a double-Gaussian fit to the observed beam. The purple dashed line is the cumulative fractional beam volume. We attribute the excess power in the wings of the observed beam to residual medium and small scale phase errors on the dish. The data points (diamonds with error bars) show a complementary determination of the beam from the 5 mJy radio source in the center of RXJ1347-1145. The beam in this case is slightly wider due to the smoothing (4" FWHM) applied to the final map, which is accounted for in the analysis.

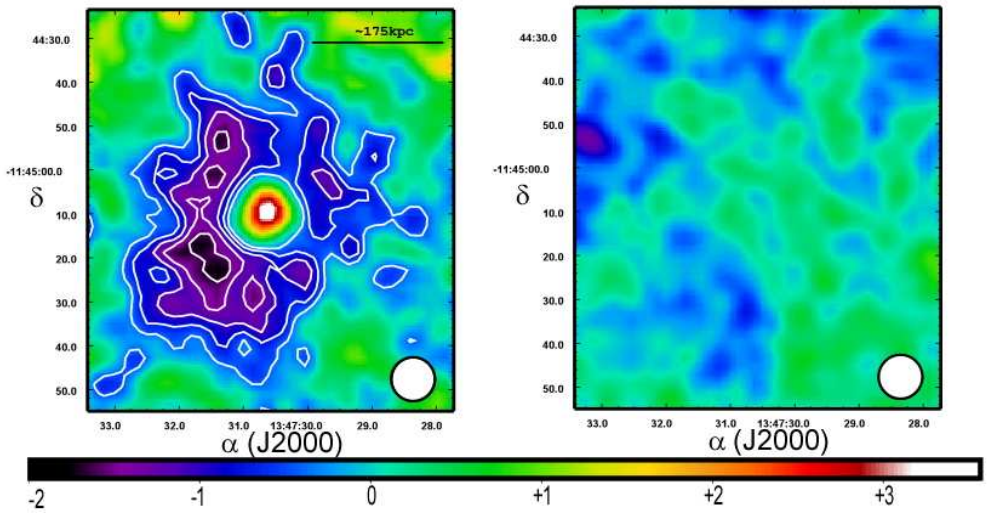

Figure 7.2 MUSTANG image of the SZE in RXJ1347-1145 (left); and the individual nights imaged separately and differenced, on the same color scale (right). The noise in the center of the map is is $\sim 0.3\,\mathrm{mJy/bm}$; contours in the left panel correspond to SNR of 1 to 5 in 1σ increments and account for variations in integration time in the map, so are not directly proportional to the image. Color scale units are mJy/bm. The MUSTANG beam ($10''$ FWHM after smoothing) is shown in the lower right of each panel.

of the map outside the fiducial region is corrected for exposure time variations assuming Gaussian, random noise with a white power spectrum. The enhancement of the SZE to the south east of the x-ray peak, originally detected by Komatsu et al. at 4.2σ significance, is confirmed by this measurement at 5.4σ (indicating the peak SNR per beam) with a factor of ~ 2 greater angular resolution.

7.4 Interpretation & Conclusions

7.4.1 Comparison with Previous SZE Observations

Figure 7.3 presents a direct comparison of the MUSTANG and NOBA results in units of main-beam averaged Compton y_C parameter. For a more accurate comparison, we downgrade the resolution and pixelscale of the MUSTANG map to match that of NOBA (13" FWHM on a 5" pixel grid). The overall agreement between the maps is excellent,

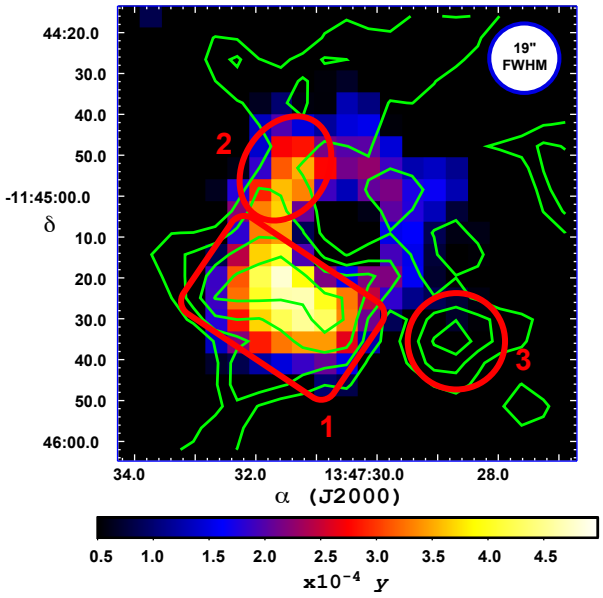

Figure 7.3 - Comparison of NOBA and Mustang maps of RX J1347-1145. The color scale shows the MUSTANG data with $5''$ pixels, smoothed to match the published NOBA map resolution. The contours show the NOBA map at intervals of 1.16×10^{-4} in y starting from 5×10^{-5}. Three labeled features are discussed in the text: *1*, the hot shock south-east of the cluster core; *2*, an enhancement in integrated pressure to the east; and *3*, a compact decrement observed at $\sim 3\sigma$ by NOBA that is absent from the MUSTANG image.

in particular as regards the amplitude and morphology of the local enhancement of the SZE south-east of the cluster core. The largest discrepancy is south west of the cluster, where NOBA shows a 3σ compact decrement which is absent from the MUSTANG data. Considering the low and uniform X-ray surface brightness in the vicinity of this discrepancy (see Figure 7.5) and the higher angular resolution and lower noise of the MUSTANG data, it is likely that this feature is a spurious artifact in the NOBA map. Both datasets also show a ridge extending north from the enhancement on the eastern side of the cluster. In the 150 GHz map the feature is of marginal significance ($1 - 2\sigma$); interestingly, it is clearly visible in the 350 GHz SZE increment map but K04 dismiss it due to the possibility of confusing dust emission from the nearby galaxies.

Component	Amplitude $[y/10^{-3}]$	Offset $['']$	Notes
β-model	1.0	$0, 0$	$\theta_c = 10''$, $\beta = 0.60$
Shock	1.6	-14, 14	$\sigma_1 = 8''$, $\sigma_2 = 2''$, P.A. $= 45°$
Ridge	1.0	10, 14	$\sigma_1 = 8''$, $\sigma_2 = 2''$, P.A. $= -15°$

Table 7.1 Note: Offset is (north,east) of peak X-ray position

7.4.2 Empirical Model of the SZE in RXJ1347-1145

We construct a simple empirical model for the cluster SZE assuming the isothermal β-model of Schindler et al. [1997] normalized by the SZE measurement of Reese et al. [2002] and Kitayama et al. [2004] to describe the bulk cluster emission. We add a 5 mJy point source in the cluster core, coincident with the peak of the β-model, and two Gaussian components in integrated pressure, one south-east and one almost directly east of the cluster center. In comparing to our 90 GHz data, we use the relatavistic correction of Sazonov and Sunyaev [1998], assuming $kT = 25\,\mathrm{keV}$ (which reduces the amplitude of the decrement by 15%) for the Gaussian components and $kT = 10\,\mathrm{keV}$ for the bulk component. The parameters chosen (two Gaussian widths for each component, a position, a peak surface brightness, and a position angle) are shown in Table 7.1. The resulting sky image is convolved with our beam (Section 7.2) and transfer function (Section 4.5). We find that this provides a good match to the data (Figure 7.4). The peak comptonization at $10''$ Gaussian resolution is 3.9×10^{-4} on the eastern ridge and 6.0×10^{-4} on the region identified as a shock by Komatsu et al. When convolved to $19''$ FWHM (NOBA) resolution, we find $\Delta y = 3.9 \times 10^{-4}$, close to their observed value $\Delta y = 4.1 \times 10^{-4}$. The intent of this static, phenomenological model is simply to provide a description of the observed high angular-resolution SZE and a direct comparison of NOBA and MUSTANG results.

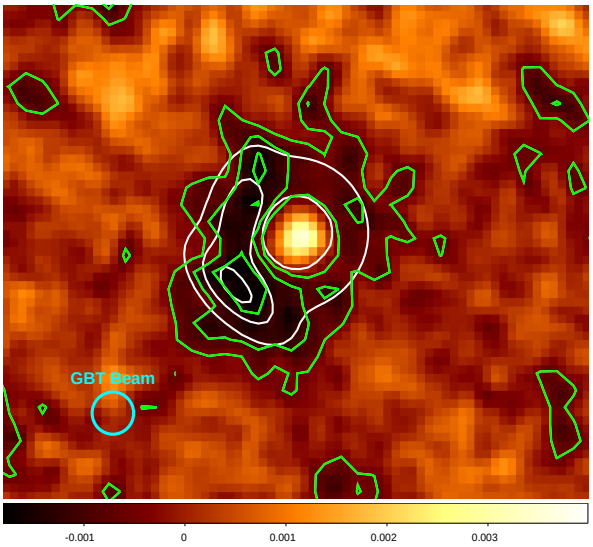

Figure 7.4 Empirical Model of the SZE in RXJ1347-1145
- MUSTANG SZE image of RXJ1347-1145 with contours (thin green lines) at −1.5, −1.0, and −0.5 mJy/bm. The bold white contours, at the same surface brightness levels, show the model SZ signal discussed in the text.

7.4.3 Multi-wavelength Phenomenology

Our data show an SZE decrement with an overall significance of 5.4σ. At the center of the cluster, coincident with the peak of X-ray emission and the brightest cluster galaxy (BCG), there is an unresolved 5 mJy radio source. This flux density is consistent with the 90 GHz flux density presented in Pointecouteau et al. [2001], as well as what is expected from a power law extrapolation of 1.4 GHz and 30 GHz measurements [Condon et al., 1998, Reese et al., 2002]. A strong, localized SZE decrement can be seen $20''$ to the south-east of the center of X-ray emission and clearly separated from the cluster center. Our data also indicate a high-pressure ridge immediately to the east of the cluster center.

K04 tentatively attribute the south-east enhancement to a substructure of gas $240 \pm 183\,\mathrm{kpc}$ in length along the line of sight, at a density (assumed uniform) of $(1.4 \pm 0.59) \times 10^{-2}\,\mathrm{cm}^{-3}$ and with a temperature $T_e = 28.5 \pm 7.3\,\mathrm{keV}$. Recent X-ray spectral measurements [Ota et al., 2008] with SUZAKU also indicate the presence of hot gas in the south-east region ($T_e = 25.1^{+6.1}_{-4.5}\ ^{+6.9}_{-9.5}\,\mathrm{keV}$ with statistical and systematic errors, respectively, at 90%

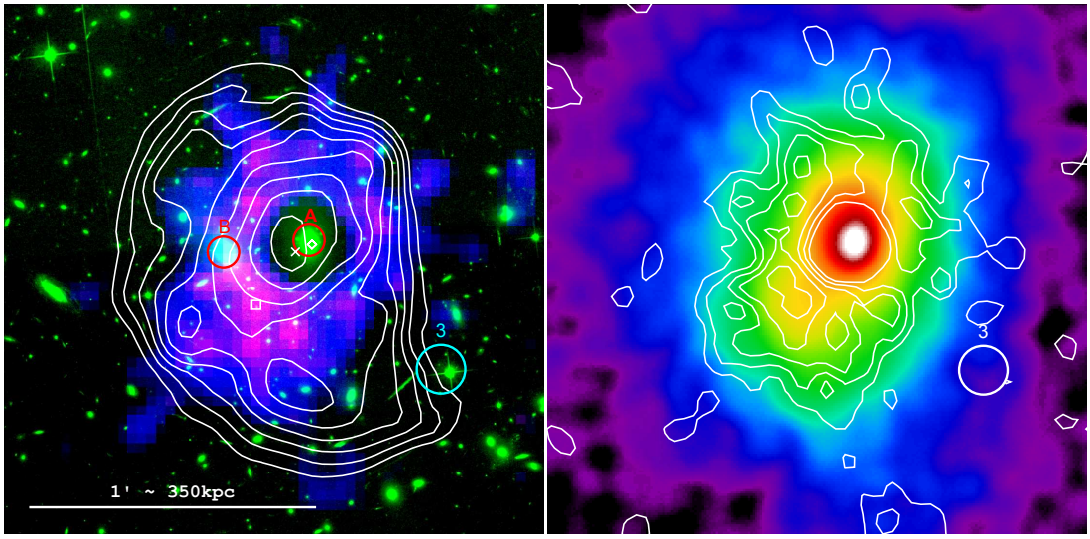

Figure 7.5 - **Left:** False color composite Image of RXJ1347-1145. Red/blue: Mustang SZ. Green: Archival HST/ACS image taken through the F814W filter; and white contours: Surface mass density κ from the weak + strong lensing analysis of Bradač et al. [2008]. Contours are linearly spaced in intervals of $\Delta\kappa = 0.1$ beginning at $\kappa = 1.0$. Several features are labelled: *A* indicates the central BCG, which is a radio source; *B* indicates the BCG of the secondary cluster; and *3* (also labeled in the right-hand panel) indicates the location of the discrepancy between NOBA and MUSTANG, discussed in the text and Figure 7.3. The diamond, cross and box mark the locations of the peaks in X-ray surface brightness, surface mass density and SZE decrement respectively. **Right:** Contours of the MUSTANG decrement SNR (1σ to 5σ in 1σ increments) superposed on the Chandra count-rate image smoothed to $10''$ resolution.

confidence level). Allen et al. [2002] have reported that the slight enhancement of softer X-ray emission in this region seen by Chandra is consistent with the presence of a small substructure of hot, shocked gas. Kitayama et al. [2004] attribute the hot gas to an ongoing merger in the plane of the sky. The merger hypothesis is supported by optical data, in particular, the presence of a second massive elliptical $\sim 20''$ directly to the east of the BCG that coincides with the center of X-ray emission (and with the radio point source). Furthermore the density and temperature of the hot substructure indicate that it is substantially overpressured compared to the surrounding ICM. Assuming a sound speed of 1600 km/sec this overpressure region should relax into the surrounding ICM on a timescale ~ 0.1 Gyr, again arguing for an ongoing merger.

Our data support this merger scenario. To put them in context, Figure 7.5 shows a composite image with archival Chandra and HST data, and the weak + strong lensing mass map of Bradač et al. [2008]. We propose that the data are best explained by a merger occuring in or near the plane of the plane of the sky. The left-hand ("B") cluster, having fallen in from the south-*west*, has just passed closest approach and is hooking around to the north-west. As the clusters merge shock forms, heating the gas in the wake of its passage. As argued by Kitayama et al. [2004], and seen in simulations [Takizawa, 1999], the clusters must have masses within a factor of 2 or 3 of equality and a substantial (~ 4000 km/sec) relative velocity in order to produce the high observed plasma temperatures, $T_e > 20$ keV. This merger geometry is consistent with the lack of structure in the line-of-sight cluster member galaxies' velocities [Cohen and Kneib, 2002]. The primary (right-hand, "A") cluster contains significant cold and cooling gas in its core (a "cooling flow"). Such gas is seen to be quite robust in simulated major cluster mergers [Gómez et al., 2002, Poole et al., 2008]. Even in cases where the cooling flow is finally disrupted by the encounter, Gómez et al. [2002] find a delay of $1-2$ GYr between the initial core encounter and the collapse of the cooling flow. The existence of a strong cooling flow, therefore, does not argue against

a major merger in this case. More detailed simulations could shed further light on this interesting system.

Chapter 8

CL1226+3332 (z = 0.89)

8.1 Background

With a mass of $(1.4 \pm 0.2) \times 10^{15}$ $M_{\odot}$ [Jee and Tyson, 2009] within r_{200}, this system is among the largest known in the high redshift Universe. Early measurements of the baryons were reported by Ebeling et al. [2001b] who identified it in the ROSAT WARPS survey. With the limited resolution of ROSAT, the cluster was deemed to display relaxed morphology.

Because of its high-redshift, X-ray spectroscopy on this object is difficult. Initial temperature measurements by *Chandra* [Bonamente et al., 2006] indicated a hot ICM ($\sim$ 14 keV). This was consistent with Maughan et al. [2004] who made previous measurements with XMM *Newton* ($\sim$ 12 keV). A more detailed analysis of the ICM properties by Maughan et al. [2007] combined *Chandra* and XMM spectroscopy. They confirmed the hot ICM and found an asymmetry in the temperature map with the cluster emission south-west of the cluster center hotter than ambient. This object has also been mapped in the SZE on arcminute scales by the SZA and a strong central decrement was measured [Muchovej et al., 2007, Mroczkowski et al., 2009].

Jee and Tyson [2009] mapped the dark matter distribution of this system through a

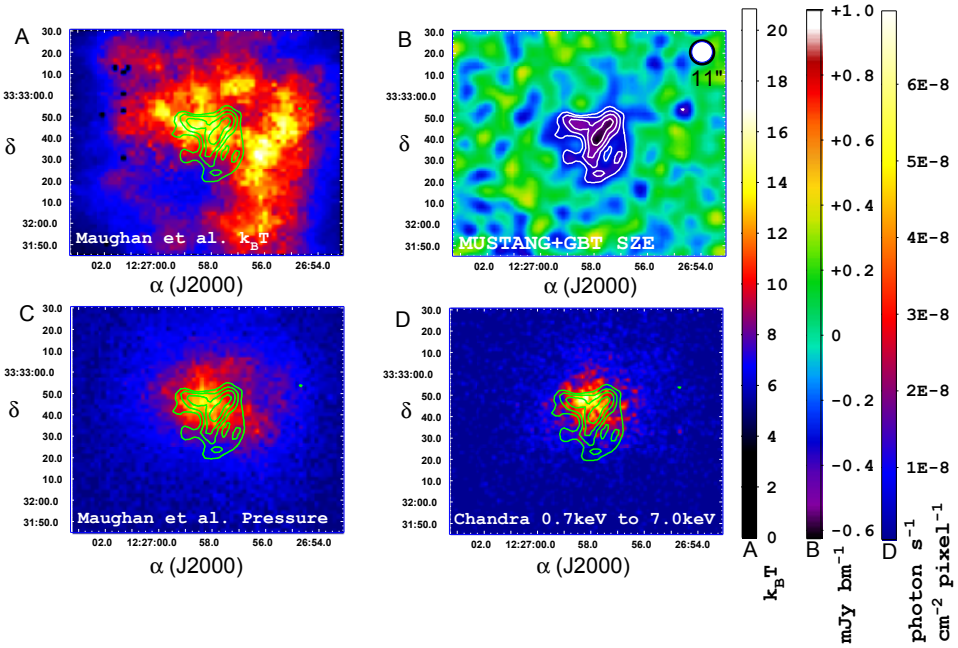

Figure 8.1 - Cl1226+3332 X-ray and SZE morphology. The contours on all images in this figure are MUSTANG SZE in units of 1σ starting at 3σ. Panel *A*: Temperature distribution from Maughan et al. [2007]. Panel *B*: MUSTANG+GBT SZE image with $11''$ effective resolution. Panel *C*: X-ray derived pseudopressure map from Maughan et al. [2007]. This was produced by taking the product of the temperature map and the square root of the surface brightness. Panel *D*: *Chandra* surface brightness in the 0.7 keV to 7.0 keV band smoothed with a $1''.5$ Gaussian.

weak lensing analysis. They found that on large scales the cluster was consistent with a relaxed morphology but the core was resolved into two distinct peaks: the dominant one in close proximity to the BCG and another $\sim 40''$ to the south west. While this sub-clump shows no surface brightness peak in either *Chandra* or XMM data, the location is consistent with the temperature enhancement reported by Maughan et al. [2007] and a secondary peak in the member galaxy density. One possible explanation of this is a merger scenario in which a smaller cluster has passed through the dominant core on a south west trajectory stripping its baryons and causing shock heating.

8.2 CL1226 MUSTANG map and Comparison to Previous Work

The MUSTANG map is shown in Figure 8.1. It reveals an asymmetric, multiply peaked pressure morphology in this high-z system. The most pronounced feature is a narrow ridge $\sim 20''$ long located $\sim 10''$ south-west of the X-ray peak. A second peak is found in good proximity to the X-ray emission which is also coincident with the BCG. Also shown in this figure is the X-ray derived temperature and pseudopressure (defined as the product of the temperature map and the square root of surface brightness) maps from Maughan et al. [2007]. The *Chandra* surface brightness image was produced with 74 ksec of archival data taken in ObsIds 3180, 5014 and 932. There is good qualitative agreement between the two data sets, although the small scale features seen by MUSTANG are absent in the Maughan map. This is not unexpected as the X-ray derived pressure relies heavily on the temperature map which was produced with a variable sized aperture. Therefore, adjacent pixels are not independent. This correlation makes the map less sensitive to small-scale features.

8.3 CL1226 Elongation and Substructure

Figure 8.2 shows radial profiles of the X-ray surface brightness, SZE and lensing mass distribution. The profiles are centered on the X-ray peak which is coincident with the BCG. Each plot shows two profiles, one taken from the south-eastern quadrant (red) and the other in the south-western quadrant (black). It is clear that all data sets are consistent with an asymmetry elongated towards the south-west as proposed by the merger scenario.

The core of this cluster is compact on the sky due to its high redshift. For this reason, the MUSTANG map can be expected to contain non-negligible amounts of flux that have been modeled in other SZE observations. To quantify the significance of the sub-structure, we compare our map to the best fit spherically symmetric Nagai et al. [2007] model of the SZA data as presented by Mroczkowski et al. [2009]. Figure 8.3 shows our map. We assume the spherically symmetric extended component modelled is centered on the X-ray peak and take the difference between the two maps. The residual map figure, contains the peak of the ridge at a 4.6-σ level.

There is a positive unresolved feature in the residual map in Figure 8.3 located $8''$ northwest of the X-ray peak. This unexplained feature could have several interpretations. It could simply be a noise artifact. However, it is also possible that it is a faint unresolved source. Because it is not detected at 30 GHz [Mroczkowski et al., 2009], such a source would require a rising spectrum in the millimeter as would be expected from a high-redshift, dusty star-forming galaxy. This galaxy could be lensed as speculated by Blain et al. [2002] and Lima et al. [2010] and similar to the one found in the Bullet cluster by Wilson et al. [2008] and confirmed by Rex et al. [2009]. Disentangling speculation such as this requires the addition of resolved millimeter or sub-millimeter follow-up with different instruments.

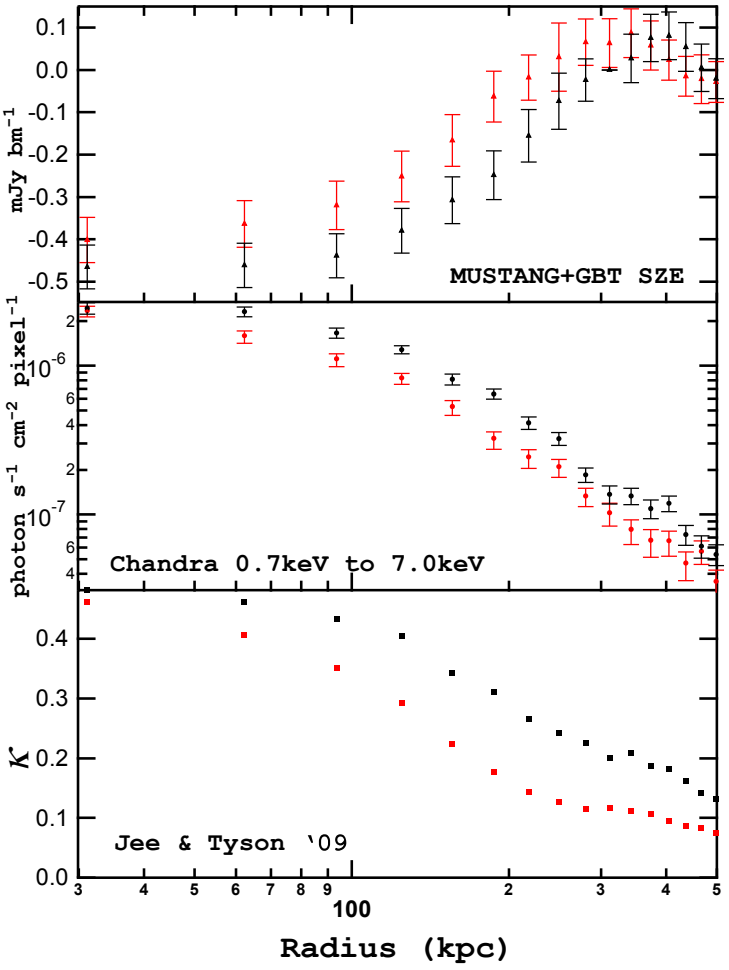

Figure 8.2 Radial profiles of CL1226+3332 from the SZE (top), X-ray surface brightness (middle) and lensing mass distribution from Jee and Tyson [2009](bottom). Profiles are centered on the X-ray peak and are taken from the south-eastern quadrant (red) and south-western quadrant(black). The SZE map was convolved with a 10″ Gaussian before averaging. All data sets are consistent with an elongation in the south-west direction as proposed by the merger scenario

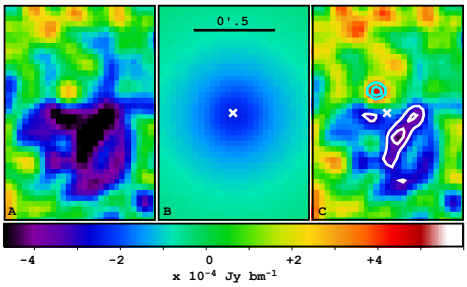

Figure 8.3 - Panel A: MUSTANG SZE map of the core in CL1226. Panel B: The best fit model of a Nagai et al. [2007] profile to SZA data as is presented in Mroczkowski et al. [2009]. The model has been passed through the appropriate transfer function. Panel C: The residual of Panel A - Panel B. The white contours are $(-3\sigma,-4\sigma)$ which show the significance of the sub-structure not accounted for in the azimuthally symmetric model. The cyan contours are $(+3\sigma,+4\sigma)$. The white x shows the location of the X-ray peak as measured by *Chandra*.

8.4 CL1226 Multiwavelength Phenomena

A multi-wavelength composite image of this system is presented in Figure 8.4 which includes the weak lensing mass distribution presented in Jee and Tyson [2009]. The northern end of the dominant ridge in the MUSTANG image, labelled "B" in this figure, is roughly coincident with the lensing mass peak. The orientation of the ridge is approximately orthogonal to a vector connecting the BCG and secondary lensing peak which is most likely the trajectory of the sub-cluster. We posit that the ridge is produced by a reservoir of shock-heated gas created in the core passage of the sub-cluster, reminiscent of the eastern peak in the famous "Bullet Cluster" [Markevitch et al., 2002a].

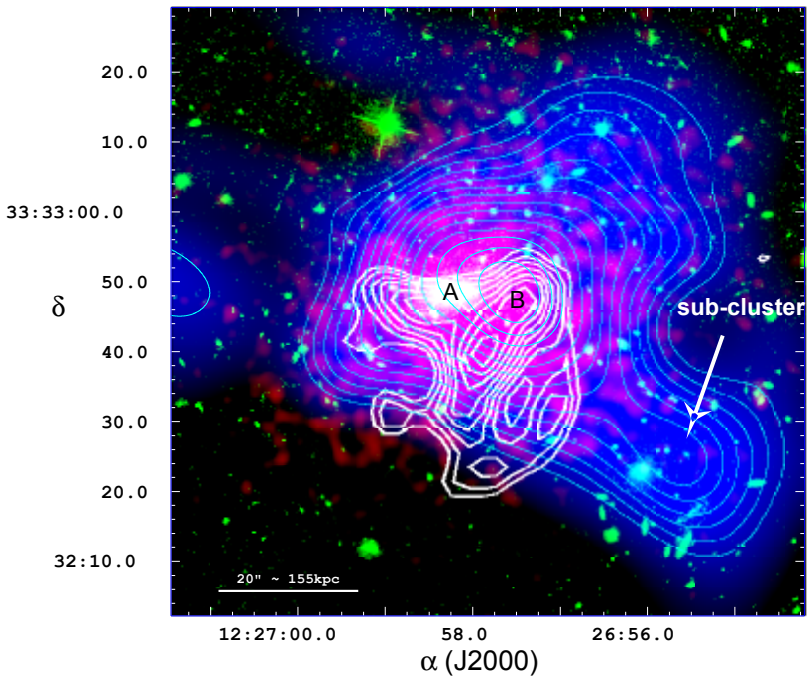

Figure 8.4 - Composite image of CL1226. Red shows the *Chandra* surface brightness in the 0.7keV to 7.0keV band. Blue color scale and cyan contours show the surface mass density distribution of Jee and Tyson [2009]. Contours are linearly spaced in 15 intervals between $\kappa = 0.25$ and $\kappa = 0.59$. Green traces the optical emission as measured by the HST/ACS in the F814W band. White contours show the MUSTANG measurement in units of 0.5σ starting at 3σ. Location A demarcates the BCG and is coincident with the X-ray surface Brightness peak. Location B shows the Dark Matter peak which is coincident with the northern lobe of the SZ ridge revealed by MUSTANG imaging.

Chapter 9

MACS0744+3927 (z = 0.69)

This massive high-redshift system, found in the MAssive Cluster Survey (MACS) of the all sky ROSAT data [Ebeling et al., 2001a], has appeared in several studies using X-ray and SZE data [e.g., LaRoque et al., 2003, 2006, Ebeling et al., 2007]. Unlike the other clusters in our sample, targeted multi-wavelength studies of MACS0744 are scarce in the literature. Kartaltepe et al. [2008] include this object in a red sequence galaxy distribution study of a subsample of 12 MACS clusters. They note that understanding the assembly dynamics of this system is made difficult by its complex morphology, which includes some evidence of a dense core in the X-ray images, and an elongated, doubly-peaked distribution of red sequence galaxies. Additionally, this cluster field contains no significant compact radio sources, as determined in a search of the Faint Images of the Radio Sky at Twenty-Centimeters [FIRST; White et al., 1997] and NRAO VLA Sky Survey [NVSS; **?**] catalogs at 1.4 GHz, as well a literature search for SZA, OVRO, and BIMA sources detected in this cluster field at ≈ 30 GHz [LaRoque et al., 2006, Mroczkowski et al., 2009].

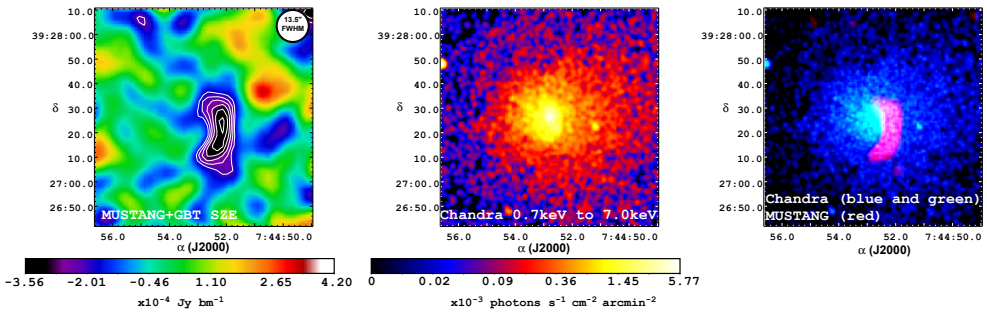

Figure 9.1 - SZE and X-ray images of MACS0744. Left: MUSTANG+GBT SZE at 13.″5 FWHM effective resolution after smoothing. Contours are multiples of 0.5σ starting at 3σ. Center: Chandra X-ray surface brightness in the cluster core. The image has been smoothed with a 1.″5 Gaussian. Right: Composite image of Chandra X-ray and MUSTANG SZE. Blue and Green are identical data on different logarithmic color scales. Red shows the MUSTANG SZE data. The kidney shaped ridge revealed by MUSTANG is aligned concentrically with a sharp surface brightness discontinuity in the Chandra map.

9.1 MUSTANG Data

The SZE map produced from 5.8 hours of MUSTANG data is shown in Figure 9.1. It consists of a kidney shaped ridge $\sim 25''$ long in the north-south direction. From east to west, the structure is roughly the width of our beam, and thus is not resolved in this direction. The curvature of this feature is well described empirically as an 80 degree sector of an ellipse with an axial ratio of 1.25, with the minor axis and center of the observed SZE being 12 degrees south of west on the sky.

9.2 *Chandra* Data

The *Chandra* image is shown beside the MUSTANG map in Figure 9.1. It was produced from nearly 90 ksec of combined archival data merged from ObsIDs 3197, 3585 and 6111 and reduced with the method described in section 4.6. The core of this cluster displays an asymmetric X-ray surface brightness morphology with a sharp discontinuity on the western edge. The concave side of the SZE peak identified by MUSTANG is aligned concentrically

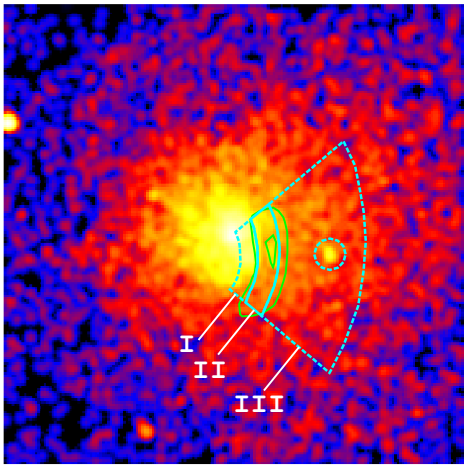

Figure 9.2 Geometry and regions used for elliptical profiles and X-ray spectroscopy on MACS0744 overlaid on the *Chandra* surface Brightness image. Green contours are $(-4.5, -5.5)\sigma$ SZE decrement. The three regions correspond to the cool intact core (I), the shock heated gas (II) and pre-shock region (III). One X-ray point source has been excised from the pre-shock region. The borders of the wedge indicate the azimuthal range used in producing radial profiles.

with the convex edge of the surface brightness discontinuity in the X-ray. Such an enhancement in the SZE in a location offset from the peak in X-ray surface brightness requires a significantly heated plasma.

9.3 X-ray Surface Brightness Shock Modeling

The combined SZE and X-ray image morphology presented in Figure 9.1 is suggestive of a system dominated by a merger driven shock-front. Arriving at this conclusion based on the existing relatively low SNR X-ray and SZE data alone would be quite tenuous; however, the kidney shaped ridge seen by MUSTANG combined with the sharp edge seen by *Chandra* is difficult to explain without invoking a shock-heating mechanism. We proceed to model the system in the framework of a shock-front through a complementary analysis of X-ray and SZE in the approach outlined below:

- The elliptical geometry and location of the shocked gas is approximated from the

SZE data.

- This geometry is used to fit a two dimensional X-ray surface brightness profile with a model consisting of three regions: a cold intact core bordered by a cold-front, a shock-heated region bordered by a shock-front, and a pre-shock region. These correspond to I, II and III, respectively, in Figure 9.2.

- X-ray spectroscopy is performed in each region to obtain the plasma temperature.

- Three dimensional density and pressure models are produced from the surface brightness and spectral fits.

- The pressure model is integrated along the line of sight to produce a two dimensional Compton y_C map.

- A mock SZE image is constructed at the resolution and with the angular extent of the MUSTANG map, and the model and data are compared.

We model the X-ray emissivity as a power law, $\varepsilon \propto r^{-p}$, within each region assuming an ellipsoidal geometry with two axes in the plane of the sky and one along the line of sight (see Appendix 11.1 for details). The model has 8 parameters in total, two characteristic radii, and a normalization and power law index in each of three regions. We perform a Markov chain Monte Carlo (MCMC) analysis using Poisson statistics for the X-ray data [for analysis and statistics details see, e.g., Reese et al., 2000, 2002, Bonamente et al., 2006]. Each chain is run for a million iterations. Convergence and mixing are checked by running two chains and comparing them against one another [Gelman and Rubin, 1992, Verde et al., 2003]. The choice of burn-in period does not significantly affect the results but for concreteness we report results using a burn in of 10,000 iterations. The model fit is limited to a wedge subtending 80° and extending from 10″ to 40″ from the nominal center.

This region corresponds to the region of interest suggested by the SZE and X-ray data as discussed in Section 9.2.

Initial attempts to model all 8 parameters at once were unsuccessful due to low SNR in these small regions, with the chains showing poor convergence. To limit the number of free parameters, we implement chains to determine the discontinuity radii, R_{s1} and R_{s2}, individually and then fix those radii. This entails using a single discontinuity model, which has 5 parameters, rather than 8. The inner discontinuity radius, R_{s1}, is determined with single discontinuity chains using the entire fitting region. The outer discontinuity radius, R_{s2}, is fit with a single discontinuity model limiting the fitting region to larger radii than R_{s1}.

With both discontinuity radii in hand, the double discontinuity model chains are run with fixed characteristic radii. This is enough of a reduction of parameter space to produce converged chains. Best fit and 68% confidence level uncertainties are shown in Table 9.1. In this table, the parameter f is defined to be the ratio of the normalization of a given region over the normalization in the cool intact core (region I). Because the radial dependence of the model follows a power law with an exponent less than zero, the amplitudes quoted here are normalized at the cold-front radius, $R_{s1} = 14\farcs19$, to avoid a singularity at the origin. Figure 9.3 shows the X-ray surface brightness profile within the fitting region along with the best fit model.

We also ran MCMC fits modeling a constant X-ray background in addition to the shock model. It has no statistically significant effect on the shock model results. This is not surprising as the X-ray background is over an order of magnitude down in surface brightness compared to the cluster signal at the outermost radius considered in the fit. The X-ray background becomes even less important towards the inner radii where the cluster signal rises.

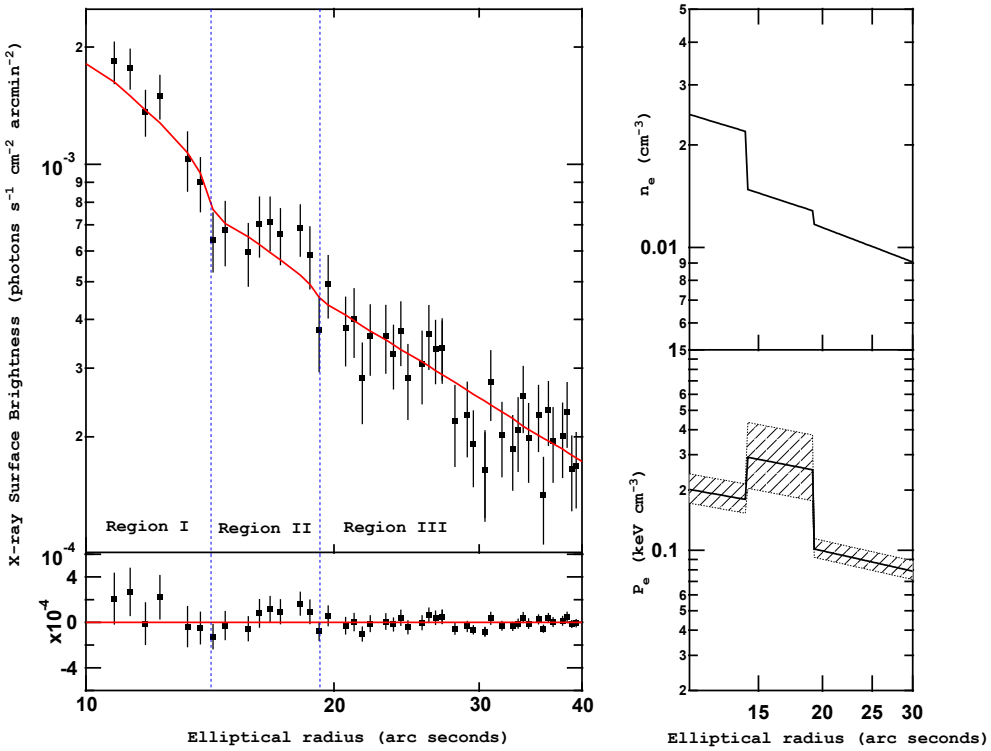

Figure 9.3 Top Left: Chandra X-ray surface brightness elliptical profile (points) and best fit analytical model in MACS0744 (red line). Bottom left: Residual of data and model in top left. Blue lines show the best fit characteristic radii for the cold-front and shock-front, 14.″19 and 19.″23 respectively. Top Right: Intrinsic electron number density model produced from the surface brightness fit on the left. Bottom Right: Pressure model produced from the above density model and the temperatures derived from *Chandra* spectroscopy. The shaded regions show the uncertainty based on the spectroscopically measured temperatures. Radii in this figure are elliptical and follow the conventions described in Appendix 11.1.

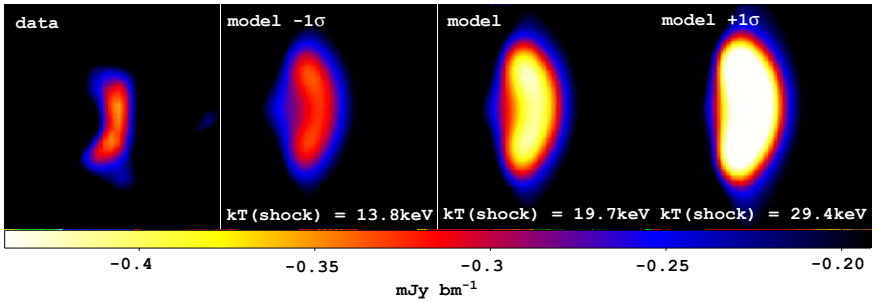

Figure 9.4 MUSTANG SZE data and models in MACS0744. Model images were generated by integrating the best fit and 1σ three dimensional pressure models from the X-ray along the line of sight and passed through the relavent angular transfer function. Comparison to the MUSTANG data shows the excellent agreement with predicted flux scale. A shock temperature closer to the -1σ value is favored by the measured SZE data.

To produce Compton y_C maps, the three dimensional pressure model was numerically integrated along the line of sight using Equation 11.17 out to an elliptical radius of $60''$, where the single power law model becomes a poor description of the X-ray data. This map is then used to produce a predicted SZE image at 90 GHz. After convolving with the GBT beam, the angular transfer function of the analysis pipeline is applied to the model in Fourier space and compared to the measured SZE data. Since the model is only valid in a specified range of angles about the center of the ellipse, the remaining sky was assumed to be well described by the double β model of LaRoque et al. [2006] and a single temperature of 8.0 keV. Three model MUSTANG maps were produced using this process and are shown alongside the data in Figure 9.4. The model uncertainty is dominated by the errors in spectroscopic $k_B T_e$ in region II. To account for this in data comparison we show three model images corresponding to pressure models produced with the best fit and the temperature fits to *Chandra* data at ± 1-σ. The flux scale in the MUSTANG map is completely consistent with the X-ray analysis and is suggestive of a temperature closer to the low end of the allowed 1-σ parameter space.

9.4 *Chandra* Spectroscopy

Informed by the shock modeling of the *Chandra* data, regions corresponding to the core, shock heated and pre-shock regions are constructed and used for spectral extraction. These correspond to regions I, II and III in Figure 9.2. Since the calibration varies both in time and over the ACIS CCDs, spectra are extracted and response files computed for each of the 3 observations individually. All three spectra are then fit simultaneously.

XSPEC [Arnaud, 1996, Dorman and Arnaud, 2001] is used to model the ICM with a Mekal spectrum [Mewe et al., 1985, 1986, Liedahl et al., 1995, Arnaud and Rothenflug, 1985, Arnaud and Raymond, 1992]. In this fit we account for Galactic extinction and assume

Table 9.1. Best Fit Parameters for the Shock Model in MACS0744

Region	f	p	$k_B T_e$ (keV)
I	1	$0.913^{+0.379}_{-0.285}$	$8.2^{+1.6}_{-1.2}$
II	$0.480^{+0.124}_{-0.084}$	$0.986^{+0.559}_{-0.349}$	$19.7^{+9.7}_{-5.9}$
III	$0.406^{+0.086}_{-0.063}$	$1.151^{+0.041}_{-0.040}$	$8.7^{+1.1}_{-0.8}$

the solar abundances of Asplund et al. [2009]. The cross sections of Balucinska-Church and McCammon [1992] with an updated He cross section [Yan et al., 1998] are used. The "cstat" statistic, which is similar to the Cash [1979] statistic, is used when modeling the data to properly account for low counts. All three spectra are fit simultaneously to the same plasma model with the abundance fixed to be 0.3 solar in all cases. The normalizations are allowed to float between data sets. The fit is limited to photons within the energy range 0.7–7.0 keV. Best fit values for the electron temperature and 68% confidence ranges are summarized in Table 9.1. Though the uncertainty is large in the photon-starved shock heated region, it is clear that there is a significant increase in temperature in this region compared to the surrounding regions.

9.5 Mach Number

We calculate the Mach number of the shock-front by fitting the Rankine-Hugoniot jump conditions. This quantity can be obtained independently by fitting the jump in density from X-ray surface brightness or in temperature as measured by spectroscopy. We use the analytic expressions from Finoguenov et al. [2010] for the Mach number in these two cases

$$\mathcal{M}_\rho = \left[\frac{2\frac{\rho_2}{\rho_1}}{\gamma + 1 - (\gamma - 1)\frac{\rho_2}{\rho_1}} \right]^{1/2} \tag{9.1}$$

and

$$\mathcal{M}_T = \left\{ \frac{8\frac{T_2}{T_1} - 7 + \left[\left(8\frac{T_2}{T_1} - 7 \right)^2 + 15 \right]^{1/2}}{5} \right\}^{1/2} , \tag{9.2}$$

where we assume the adiabatic index for a monatomic gas $\gamma = \frac{5}{3}$ and ρ_1, ρ_2, T_1 and T_2 are the density and temperature before and after the shock.

The Mach number can also be calculated from the stagnation condition. This relates the ratio of the pressure at the edge of the cold-front, P_{st}, over the pressure just ahead the shock-front, P_1, to the Mach number through the relationship

$$\frac{P_{st}}{P_1} = \mathcal{M}_{st}^2 \left(\frac{\gamma + 1}{2} \right)^{\frac{\gamma+1}{\gamma-1}} \left(\gamma - \frac{\gamma - 1}{2\mathcal{M}_{st}^2} \right)^{-\frac{1}{\gamma-1}} \tag{9.3}$$

as presented in Sarazin [2002].

We calculate the Mach number for the potential merger in MACS0744 using Equations 9.1, 9.2 and 9.3. The value obtained from the density jump conditions was calculated from the posterior MCMC used in the fit to the X-ray surface brightness. This yielded the value $\mathcal{M}_\rho = 1.2^{+0.2}_{-0.2}$ where the errors are 1-σ and the full discrete probability distribution function is shown in Figure 9.5. The Mach number obtained from the relation imposed by the stagnation condition is $\mathcal{M}_{st} = 1.4^{+0.2}_{-0.2}$ which is in excellent agreement with the number provided by fitting the density jump. The temperature jump conditions at the shock yield a higher value, $\mathcal{M}_T = 2.1^{+0.8}_{-0.5}$. While this measurement suggests a greater shock velocity, the error bars are large and it agrees at the 1.3-σ level with our estimate from the density jump condition. The flux scale in the MUSTANG image suggests the true temperature is towards the low end of the *Chandra* range as is shown in Figure 9.4. The shock velocity in this cluster is 1827^{+267}_{-195} km s^{-1} assuming the Mach number obtained from the density jump conditions.

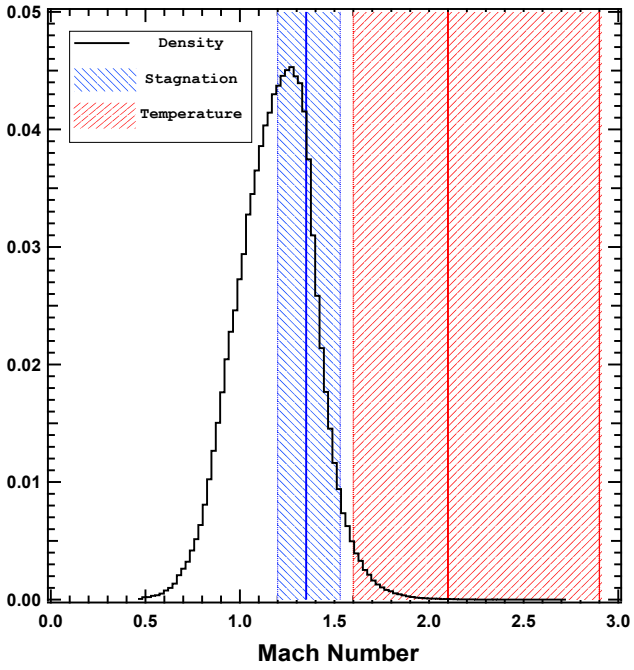

Figure 9.5 Mach number in MACS0744 obtained with 3 methods. The black histogram shows the discrete PDF calculated from the density jump conditions in the MCMC fit to the surface brightness distribution. The red area shows the 68% confidence region from the calculation of a temperature jump across the shock-front as measured from from *Chandra* spectroscopy. The blue area is the 68% confidence region obtained by fitting the stagnation condition. The solid red and blue lines are the best fit values obtained from the temperature jump and stagnation conditions respectively. While the stagnation and density jump conditions yield highly consistent results, the result from the temperature jump conditions appear to be biased high. This is due to a heavy reliance on the spectroscopy in the low SNR region II.

9.6 Discussion

This high-redshift system has proved to be an excellent example of the power of combining resolved SZE and X-ray imaging. The high-resolution SZE measurements reveal a region which is likely the result of a shock. Guided by this data, two sharp discontinuities and a spectrum consistent with a substantially hotter plasma are detected in the low SNR X-ray data. Deeper *Chandra* observations of this cluster will help confirm the presence of a shock and more accurately determine its Mach number, which for the density jump fit to the current data is mildly consistent with a transonic event ($\mathcal{M} = 1$).

Figure 9.6 shows a composite image of this system including the strong lensing mass distribution [Richard, 2011, in prep.](see also Jones et al. [2010]). This reveals a highly asymmetric elliptical mass distribution elongated to the west consistent with the red sequence member galaxy distribution presented in Kartaltepe et al. [2008]. Zitrin et al. [2010] have also done a mass reconstruction and independently obtained a similar mass distribution. The HST data shown in green contains multiple bright red elliptical galaxies with BCG-like characteristics. Galaxy $G1$ is coincident with the X-ray surface brightness peak and is assumed to be the BCG of the main cluster. Roughly one arcminute to the west of the X-ray center, the lensing mass reveals a second peak containing the bright red galaxies $G2$ and $G3$. While the baryon distribution is elongated in the direction of this potential sub-cluster, there is no X-ray peak associated with it. This is likely explained by ram-pressure stripping during passage of the sub-cluster through the main core. Galaxy $G4$ is another massive cluster member located west of the main peak. This too has a significant dark matter halo with no apparent baryonic peak. The presence of multiple peaks in dark matter and galaxy density with no accompanying baryonic mass is suggestive of a merger scenario in which a smaller cluster has passed through the main core, stripping it of its baryons and producing a shock wave in the ICM. The geometry of the westerly elongated

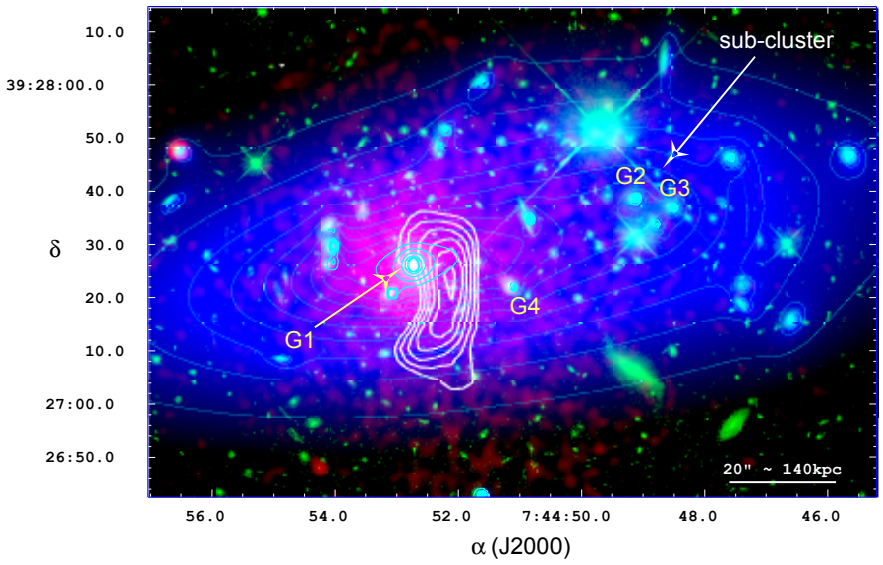

Figure 9.6 Multi-wavelength composite image of MACS0744. Green is HST/ACS data in the F814W band. Red is *Chandra* X-ray smoothed with a 1.″5 Gaussian. Blue color-scale and contours show the strong lensing mass reconstruction of Richard [2011, in prep.]. White contours are the MUSTANG SZE and are identical to those in Figure 9.1. They are in units of SNR to account for uneven exposure across the field shown here. Galaxy "G1" is the BCG of the main cluster. The lensing mass reveals a distinct elongation towards the west. Galaxies "G2" and "G3" are bright red ellipticals located in the center of a secondary mass peak with no corresponding baryonic emission seen in X-ray. The SZE shows no enhancement at this location either; however, the constraint is weaker as the SZE map has large uncertainty at this location due to central weighting of scan strategy. "G4" is another bright cluster member which harbors an X-ray point source. It too is coincident with a dark matter peak. The presence of peaks in mass distribution with no corresponding baryons is suggestive of a merger scenario in which an infalling sub-cluster has passed through the main core, losing its baryons to ram pressure stripping. It is likely that the weak shock identified by MUSTANG was produced by one of these events.

multiply peaked dark matter distribution is qualitatively suggestive of a merger scenario in which the shock-heated gas identified by MUSTANG could have been produced. However, an accurate interpretation of the merger dynamics requires detailed modeling through hydrodynamical simulations.

Chapter 10

Future Work

The diversity of the 3 mm sky and the potential impact of a high angular resolution single dish camera have been realized through MUSTANG on the GBT. Since its commissioning, it has been applied to a wide range of science. Examples in our own Galaxy include mapping the emission from high mass star forming regions [Dicker et al., 2009], probing dense cores in class 0 protostars [Shirley et al., 2011] and measuring the short wavelength synchrotron emission from supernova remnants [Arendt et al., 2011]. Extragalactic science with MUSTANG has included a survey of flat spectrum point sources [Sajina et al., 2011], measurements of spectral aging along jets in nearby AGN [Cotton et al., 2009], and of course, the resolved imaging of the SZE in merging clusters of galaxies.

The SZE work presented in this thesis has been built on several decades of progress in the fields of cosmology and extragalactic astrophysics. The discovery and exploration of the intrinsic properties of the CMB has provided a profound and precise dataset. As is demonstrated in this thesis, the field is currently at a stage where the CMB is used not only for its intrinsic information, but can be exploited as a tool to probe the physics which govern the plasma atmospheres in clusters of galaxies.

The targeted SZE sample imaged with MUSTANG presented here represents a pilot study. It has demonstrated the potential of high-resolution SZE to identify sub-structures

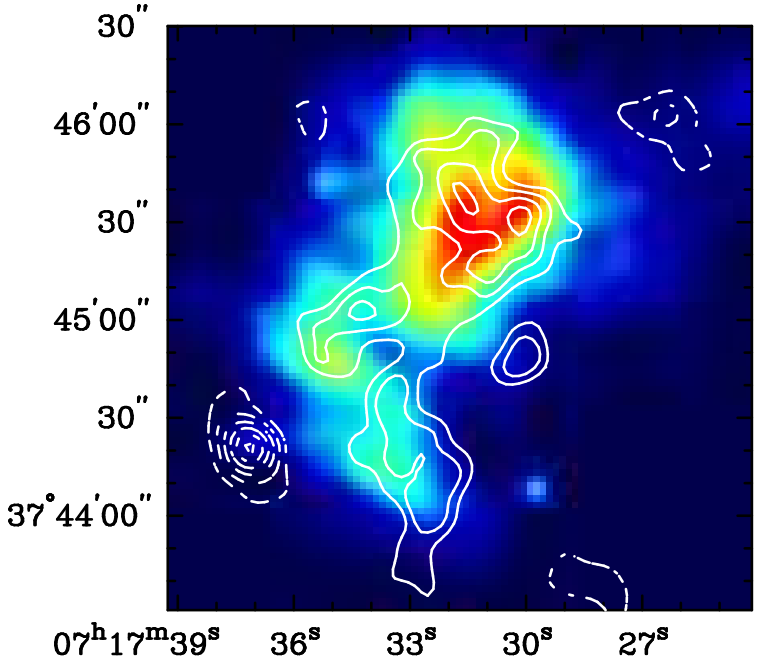

Figure 10.1 *Chandra* X-ray surface brightness (color scale) and new MUSTANG SZE (contours) image of MACSJ0717+3927. The system is extraordinarily complex with highly asymmetric morphology. Figure courtesy of Tony Mroczkowski.

such as weak shocks in galaxy clusters. This is particularly true of the high-redshift universe where the X-ray data are photon starved. Observations are currently underway to expand the sample of MUSTANG clusters with the goal of identifying and quantifying substructure in the pressure distributions. New data measured on the superbly disturbed cluster MACSJ0717.5 are shown in Figure 10.1. This system is highly asymmetric and displays complex morphology in the optical, X-ray, SZE and radio. Work to extract the energetics and merger dynamics of this complicated cluster is underway using a high quality multiwavelength dataset.

A next generation feedhorn-coupled TES bolometer array for the GBT is currently in the planning stages called MUSTANG-2. With a much larger FOV (4.′5) and a mapping speed 1000 times that of MUSTANG it will be able to image a large number of clusters on angular scales from 9″ to 9′. With such a high mapping speed and spatial dynamic range, the MUSTANG-2 data set will provide not only interesting phenomenological studies on

individual clusters, but a systematic investigation into global effects which can contribute to conclusions on cosmological constraints using clusters. Other instruments coming on line in the next decade, such as ALMA, the LMT, SCUBA2 and CCAT will also have high-resolution SZE capabilities.

Chapter 11

Appendix: Shock model

11.1 Surface Brightness Profiles

In this work, we measure the density characteristics of a shock-front and cold front in MACS0744 by analyzing the elliptical profiles of X-ray surface brightness $I(x, y)$ in some observed photon energy band E_1 to E_2. (In this paper, we consider the surface brightness in the 0.7–7 keV band.) Here, we give the analytic expressions for the X-ray surface brightness of elliptical X-ray images with discontinuities. The X-ray surface brightness is given by the line of sight integral

$$I(x, y) = \frac{1}{4\pi(1 + z_r)^\eta} \int \varepsilon(x, y, z)\, dz\,, \tag{11.1}$$

where ε is the X-ray emissivity integrated over all directions in the emitted energy band $E_1(1 + z_r)$ to $E_2(1 + z_r)$. The Cartesian coordinates x, y, and z are aligned as shown in Figure 11.1, with z being along the line of sight. The cluster redshift is z_r. The parameter η is 4 if $I(x, y)$ is given in energy units, and $\eta = 3$ if $I(x, y)$ is in counts units, which is generally the case for X-ray observations.

We fit the data with an analytic expression for the above integral obtained with the following assumptions:

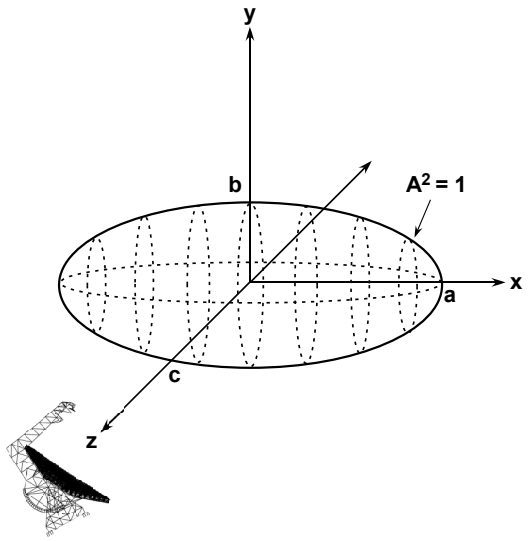

Figure 11.1 - Elliptical geometry for a single surface brightness edge used in modeling shock fronts.

1. The X-ray emissivity $\varepsilon(x, y, z)$ is constant on concentric, aligned, similar ellipsoidal surfaces with the geometry and conventions described in figure 11.1. The three principal axes of this elliptical distribution are a, b, and c.

2. Two of the principal axes of the distribution (a and b) lie in the plane of the sky, and the third axis (c) lies along the line of sight. We take the x axis of our coordinate system to be parallel to a, and the y axis to be parallel to b. The axis given by a or x is along the direction of propagation of the shock and/or cold front.

3. Between each of the discontinuities, the emissivity varies as a power-law of the radius, $\varepsilon = \varepsilon_o r^{-p}$. Here, r is the scaled elliptical radius $r = [(x/a)^2 + (y/b)^2 + (z/c)^2]^{1/2}$ and p is the power law index. The emissivity changes discontinuously at the shock front and/or cold front.

4. The shock front and/or cold front has rotational symmetry about an axis in the plane of the sky along its direction of propagation ($c = b$). Although we make this assumption in our analysis of the data on MACS0744, none of the expressions given

below depend on this assumption, and are correct for any c.

We treat separately each of the regions bounded by one or two discontinuities. In the case of a shock and cold front, there are three separate regions: the pre-shock gas, the shock-heated gas, and the cold front gas. Since equation (11.1) is linear in ε, we can then sum the surface brightnesses of these regions to give the total surface brightness.

Since the plane of the sky corresponds to a plane of symmetry at $z = 0$ in this model, the integral for the surface brightness can limited to positive z and doubled, giving

$$I(x, y) = \frac{1}{2\pi(1 + z_r)^\eta} \int_{q_1}^{q_2} \varepsilon(x, y, z)\, dz\,. \tag{11.2}$$

The values of $q_1 \geq 0$ and $q_2 \geq 0$ give the extent of the cluster region along the line of sight. The general form for the surface brightness for each of the regions obtained with these assumptions after integration is

$$I(x, y) = \frac{1}{4\pi^{1/2}(1 + z_r)^\eta} \epsilon_0 c \frac{\Gamma(p - \frac{1}{2})}{\Gamma(p)} A^{-2p+1} \phi\,, \tag{11.3}$$

where we define A to be the two-dimensional scaled elliptical radius

$$A(x, y) \equiv \left(\frac{x^2}{a^2} + \frac{y^2}{b^2} \right)^{1/2}\,, \tag{11.4}$$

and Γ is the standard Gamma function. The piecewise function ϕ takes a form which depends on the complexity of the model for a given region of interest. Between the discontinuities, each emission region can be treated as having a single outer edge, a single inner edge, or both an inner and outer edge. For example, in MACS0744, the pre-shock region has a single inner edge, the cold core has a single outer edge, and the shock-heated region has both and inner and outer edge. The total surface brightness is the sum of these three regions.

For one outer edge, we assume this edge is located at $r = 1$ in three dimensions and at $A = 1$ in projection. Then, the bounds on the integral in equation (11.2) are $q_1 = 0$ and

$$q_2 = c \begin{cases} (1 - A^2)^{1/2} \,, & A < 1 \\ 0 & A \geq 1 \,, \end{cases} \tag{11.5}$$

and ϕ takes the form

$$\phi = \begin{cases} 1 - I_{A^2}(p - \frac{1}{2}, \frac{1}{2}) \,, & A < 1 \\ 0 \,, & A \geq 1 \,. \end{cases} \tag{11.6}$$

Here, $I_x(u, v)$ is the scaled incomplete beta function $I_x(u, v) \equiv B_x(u, v)/B(u, v)$, $B_x(u, v)$ is the incomplete beta function, and $B(u, v) \equiv \Gamma(u)\Gamma(v)/\Gamma(u + v)$ is the beta function. Note that very efficient algorithms for calculating $B(u, v)$ and $I_x(u, v)$ exist and can be found as intrinsic functions on most computer systems. Alternatively, they are given in *Numerical Recipes* [Press et al., 1993].

For a single inner edge located at $r = R$ in three dimension and at $A = R$ in projection, the bounds are

$$q_1 = c \begin{cases} (R^2 - A^2)^{1/2} \,, & A < R \\ 0 \,, & A \geq R \,, \end{cases} \tag{11.7}$$

and $q_2 = \infty$ and we have

$$\phi = \begin{cases} I_{\frac{A^2}{R^2}}(p - \frac{1}{2}, \frac{1}{2}) \,, & A < R \\ 1 \,, & A \geq R \,. \end{cases} \tag{11.8}$$

It is useful to note that our expression for a single outer edge is mathematically identical to the expression derived in Vikhlinin et al. [2001] but uses the incomplete beta function (which is more convenient numerically) as opposed to the hyper-geometric function .

Finally, for a region with two edges, we will take their locations to be $r = 1$ in three

dimensions and $A = 1$ in projection for the inner edge, and $r = R$ or $A = R$ for the outer edge, where $R > 1$. The bounds on the integral become

$$q_1 = c \begin{cases} (1 - A^2)^{1/2} \,, & A < 1 \\ 0 \,, & A \geq 1 \,, \end{cases} \tag{11.9}$$

and

$$q_2 = c \begin{cases} (R^2 - A^2)^{1/2} \,, & A < R \\ 0 \,, & A \geq R \,. \end{cases} \tag{11.10}$$

The expression for ϕ becomes

$$\phi = \begin{cases} I_{A^2}(p - \frac{1}{2}, \frac{1}{2}) - I_{\frac{A^2}{R^2}}(p - \frac{1}{2}, \frac{1}{2}) \,, & A < 1 \\ 1 - I_{\frac{A^2}{R^2}}(p - \frac{1}{2}, \frac{1}{2}) \,, & 1 \leq A < R \\ 0 \,, & A \geq R \,. \end{cases} \tag{11.11}$$

11.2 Density Profiles

Once we have obtained the power law index p and the normalization ε_o by fitting equation 11.3 to the data, we can reconstruct the intrinsic emissivity distribution. This is related to the density distribution $n_e(r)$ by

$$n_e(r) = \left[\frac{\varepsilon(r)}{\Lambda(T_e, Z)} \right]^{1/2} \,, \tag{11.12}$$

where Λ is the X-ray emissivity function which depends on electron temperature T_e and abundance Z.

If XSPEC[1] is used to determine the temperatures in the emission regions, the same models can easily be used to determine the value of Λ. This has the great advantage

[1] http://heasarc.nasa.gov/xanadu/xspec/

that the models, temperature, abundances, and instrument responses used for the spectral analysis will be completely consistent with those used to determine $n_e(r)$. We assume here that the model is a single-temperature MEKAL or APEC model. For this purpose, only the shape of the spectrum matters, not its normalization, so the region fit in XSPEC need not be identical to the region fit in the surface brightness analysis, as long as the spectral shape is assumed to be the same. If the surface brightness I is analyzed in energy units, then the procedure is to determine the X-ray flux F of the spectral region in the same band and with the same instrument as used to fit the surface brightness. If the surface brightness was corrected for absorption, then the absorbing column should first be set to zero. One also needs to record the normalization of the thermal model, which is defined as

$$K \equiv \frac{10^{-14}}{4\pi(1+z_r)^2 D_A^2} \int n_e n_p \, dV \,, \tag{11.13}$$

where D_A is the angular diameter distance to the cluster, n_p is the proton number density, and V is the volume of the emitting region. Then, the relevant X-ray emissivity function is

$$\Lambda = \frac{F(1+z_r)^2}{10^{14} K (n_e/n_p)} \,. \tag{11.14}$$

Here, $n_e/n_p \approx 1.21$ is the ratio of the electron to proton number densities, and is essentially a constant for typical cluster temperatures and abundances.

If the surface brightness is determined in count units (as is typically the case with X-ray observations), then the procedure is to set the observed energy band and instrument in XSPEC to the one used for the surface brightness measurements, and then type "show" to determine the model countrate CR. Then, the emissivity function is

$$\Lambda = \frac{CR\,(1+z_r)}{10^{14} K (n_e/n_p)} \,. \tag{11.15}$$

11.3 Pressure and SZE

With a three dimensional density model obtained through the above procedure and measurements of T_e from X-ray spectroscopy, one can produce a three dimensional pressure model which can be used to predict the observed SZ flux. From the ideal gas law, the electron pressure is simply

$$P_e(r) = k_B n_e(r) T_e(r)\,. \tag{11.16}$$

By integrating this along the line of sight, one can obtain a two dimensional map of the Compton y_C parameter

$$y_C(x,y) = \int \frac{P_e(r)\sigma_T}{m_e c_l^2}\, dz. \tag{11.17}$$

Here, k_B is Boltzmann's constant, σ_T and m_e are the Thomson cross section and mass of the electron respectively, and c_l is the speed of light.

Assuming that $T_e(r)$ is either a constant or is a power-law function of the radius within each region, the electron pressure will vary as a power-law of the elliptical radius, and the same analytic expression (equation 11.3) can be used to determine $y_C(x,y)$. One simply makes the substitution

$$\frac{1}{4\pi(1+z_r)^\eta}\varepsilon \rightarrow \frac{P_e(r)\sigma_T}{m_e c_l^2}\,. \tag{11.18}$$

From a map of y_C, it is straightforward to produce a model SZE image.

Chapter 12

Appendix: Acronyms

Acronym	Meaning
AC	Alternating Current
ACIS	Advanced CCD Imaging Spectrometer
AGN	Active Galactic Nucleus
BCG	Brightest Cluster Galaxy
BIMA	Berkeley Illinois Maryland Association
CCD	Charge Coupled Device
CMB	Cosmic Microwave Background
DAC	Digital to Analog Converter
DC	Direct Current
DFB	Digital Feed Back
FB	FeedBack
FOV	Field Of View
FPGA	Field Programmable Gate Array
FWHM	Full Width Half Max
GBT	Green Bank Telescope
GSFC	Goddard Space Flight Center
HDPE	High Density Poly Ethylene
HST	Hubble Space Telescope
ICM	Intra Cluster Medium
IDL	Interactive Data Language
IR	Infra Red
LFC	Local Focus Correction
LUT	Look Up Table
MACS	MAssive Cluster Survey
MCMC	Markov Chain Monte Carlo
MUSTANG	The MUltiplexed SQUID TES Array at Ninety Gigahertz

Acronym	Meaning
NEP	Noise Equivalent Power
NIST	National Institute of Standards and Technology
NRAO	National Radio Astronomy Observatory
NVSS	NRAO VLA Sky Survey
OFHC	Oxygen Free High Conductivity
OOF	Out Of Focus
OVRO	Owens Valley Radio Observatory
PAH	Polycyclic Aromatic Hydrocarbon
PT	Pulse Tube
RA	Right Ascension
RF	Radio Frequency
RFI	Radio Frequency Interference
RMS	Root Mean Square
SA	Series Array
SAE	Scaled Accumulated Error
SNR	Signal to Noise Ratio
SQUID	Superconducting Quantum Interference Device
SPT	South Pole Telescope
SZE	Sunyaev Zel'dovich Effect
SZA	Sunyaev Zel'dovich Array
TES	Transition Edge Sensor
TFN	Thermal Fluctuation Noise
UV	Ultra Violet
VLA	Very Large Array
XMM	X-ray Multi-mirror Mission

Bibliography

S. W. Allen, R. W. Schmidt, and A. C. Fabian. Chandra observations of RX J1347.5-1145: the distribution of mass in the most X-ray-luminous galaxy cluster known. *MNRAS*, 335:256–266, September 2002. doi: 10.1046/j.1365-8711.2002.05554.x.

R. G. Arendt, J. V. George, J. G. Staguhn, D. J. Benford, M. J. Devlin, S. R. Dicker, D. J. Fixsen, K. D. Irwin, C. A. Jhabvala, P. M. Korngut, A. Kovács, S. F. Maher, B. S. Mason, T. M. Miller, S. H. Moseley, S. Navarro, A. Sievers, J. L. Sievers, E. Sharp, and E. J. Wollack. The Radio - 2 mm Spectral Index of the Crab Nebula Measured with GISMO. *ArXiv e-prints*, March 2011.

K. A. Arnaud. XSPEC: The First Ten Years. In G. H. Jacoby & J. Barnes, editor, *Astronomical Data Analysis Software and Systems V*, volume 101 of *Astronomical Society of the Pacific Conference Series*, page 17, 1996.

M. Arnaud and J. Raymond. Iron ionization and recombination rates and ionization equilibrium. *ApJ*, 398:394, October 1992. doi: 10.1086/171864.

M. Arnaud and R. Rothenflug. An updated evaluation of recombination and ionization rates. *A&AS*, 60:425, June 1985.

M. Asplund, N. Grevesse, A. J. Sauval, and P. Scott. The Chemical Composition of the Sun. *ARA&A*, 47:481, September 2009. doi: 10.1146/annurev.astro.46.060407.145222.

M. Balucinska-Church and D. McCammon. Photoelectric absorption cross sections with variable abundances. *ApJ*, 400:699, December 1992. URL http://adsabs.harvard.edu/cgi-bin/nph-bib$_q$*uery?bibcode* = 1992*ApJ*...400..699*Bdb*$_k$*ey* = *AST*.

M. Birkinshaw. The Sunyaev-Zel'dovich effect. *Phys. Rep.*, 310:97–195, March 1999. doi: 10.1016/S0370-1573(98)00080-5.

A. W. Blain, I. Smail, R. J. Ivison, J.-P. Kneib, and D. T. Frayer. Submillimeter galaxies. *Phys. Rep.*, 369:111–176, October 2002. doi: 10.1016/S0370-1573(02)00134-5.

M. Bonamente, M. K. Joy, S. J. LaRoque, J. E. Carlstrom, E. D. Reese, and K. S. Dawson. Determination of the Cosmic Distance Scale from Sunyaev-Zel'dovich Effect and Chandra X-Ray Measurements of High-Redshift Galaxy Clusters. *ApJ*, 647:25–54, August 2006. doi: 10.1086/505291.

M. Bradač, T. Schrabback, T. Erben, M. McCourt, E. Million, A. Mantz, S. Allen, R. Blandford, A. Halkola, H. Hildebrandt, M. Lombardi, P. Marshall, P. Schneider, T. Treu, and J.-P. Kneib. Dark Matter and Baryons in the X-Ray Luminous Merging Galaxy Cluster RX J1347.5-1145. *ApJ*, 681:187–196, July 2008. doi: 10.1086/588377.

J. E. Carlstrom, G. P. Holder, and E. D. Reese. Cosmology with the Sunyaev-Zel'dovich Effect. *ARA&A*, 40:643–680, 2002a. doi: 10.1146/annurev.astro.40.060401.093803.

J. E. Carlstrom, G. P. Holder, and E. D. Reese. Cosmology with the Sunyaev-Zel'dovich Effect. *ARA&A*, 40:643–680, 2002b. doi: 10.1146/annurev.astro.40.060401.093803.

W. Cash. Parameter estimation in astronomy through application of the likelihood ratio. *ApJ*, 228:939, March 1979. URL http://adsabs.harvard.edu/cgi-bin/nph-bib$_q$*uery?bibcode* = 1979*ApJ*...228..939*Cdb*$_k$*ey* = *AST*.

J. G. Cohen and J.-P. Kneib. Losing Weight: A Keck Spectroscopic Survey of the Massive Cluster of Galaxies RX J1347-1145. *ApJ*, 573:524–532, July 2002. doi: 10.1086/340658.

J. J. Condon, W. D. Cotton, E. W. Greisen, Q. F. Yin, R. A. Perley, G. B. Taylor, and J. J. Broderick. The NRAO VLA Sky Survey. *AJ*, 115:1693–1716, May 1998. doi: 10.1086/300337.

W. D. Cotton, B. S. Mason, S. R. Dicker, P. M. Korngut, M. J. Devlin, J. Aquirre, D. J. Benford, S. H. Moseley, J. G. Staguhn, K. D. Irwin, and P. Ade. 90 GHz Observations of M87 and Hydra A. *ApJ*, 701:1872–1879, August 2009. doi: 10.1088/0004-637X/701/2/1872.

M. J. Devlin, S. R. Dicker, J. Klein, and m. p. Supanich. A high capacity completely closed-cycle 250 mK ^{3}He refrigeration system based on a pulse tube cooler. *Cryogenics*, 44:611–616, 2004.

S. R. Dicker, B. S. Mason, P. M. Korngut, W. D. Cotton, M. Compiègne, M. J. Devlin, P. G. Martin, P. A. R. Ade, D. J. Benford, K. D. Irwin, R. J. Maddalena, J. P. McMullin, D. S. Shepherd, A. Sievers, J. G. Staguhn, and C. Tucker. 90 GHz and 150 GHz Observations of the Orion M42 Region. A Submillimeter to Radio Analysis. *ApJ*, 705:226–236, November 2009. doi: 10.1088/0004-637X/705/1/226.

B. Dorman and K. A. Arnaud. Redesign and Reimplementation of XSPEC. In F. R. Harnden Jr., F. A. Primini, & H. E. Payne, editor, *Astronomical Data Analysis Software and Systems X*, volume 238 of *Astronomical Society of the Pacific Conference Series*, page 415, 2001.

H. Ebeling, A. C. Edge, and J. P. Henry. MACS: A Quest for the Most Massive Galaxy Clusters in the Universe. *ApJ*, 553:668–676, June 2001a. doi: 10.1086/320958.

H. Ebeling, L. R. Jones, B. W. Fairley, E. Perlman, C. Scharf, and D. Horner. Discovery of

a Very X-Ray Luminous Galaxy Cluster at Z=0.89 in the Wide Angle ROSAT Pointed Survey. *ApJ*, 548:L23–L27, February 2001b. doi: 10.1086/318915.

H. Ebeling, E. Barrett, D. Donovan, C.-J. Ma, A. C. Edge, and L. van Speybroeck. A Complete Sample of 12 Very X-Ray Luminous Galaxy Clusters at z larger than 0.5. *ApJ*, 661:L33–L36, May 2007. doi: 10.1086/518603.

A. Finoguenov, C. L. Sarazin, K. Nakazawa, D. R. Wik, and T. E. Clarke. XMM-Newton Observation of the Northwest Radio Relic Region in A3667. *ApJ*, 715:1143–1151, June 2010. doi: 10.1088/0004-637X/715/2/1143.

A. Gelman and D. B. Rubin. ? *Statist. Sci.*, 7:457, 1992.

M. Gitti, C. Ferrari, W. Domainko, L. Feretti, and S. Schindler. Discovery of diffuse radio emission at the center of the most X-ray-luminous cluster RX J1347.5-1145. *A&A*, 470: L25–L28, August 2007. doi: 10.1051/0004-6361:20077658.

P. L. Gómez, C. Loken, K. Roettiger, and J. O. Burns. Do Cooling Flows Survive Cluster Mergers? *ApJ*, 569:122–133, April 2002. doi: 10.1086/339280.

H. Gursky, A. Solinger, E. M. Kellogg, S. Murray, H. Tananbaum, R. Giacconi, and A. Cavaliere. X-Ray Emission from Rich Clusters of Galaxies. *ApJ*, 173:L99+, May 1972. doi: 10.1086/180926.

A. D. Hincks, V. Acquaviva, P. Ade, P. Aguirre, M. Amiri, J. W. Appel, L. F. Barrientos, E. S. Battistelli, J. R. Bond, B. Brown, B. Burger, J. Chervenak, S. Das, M. J. Devlin, S. Dicker, W. B. Doriese, J. Dunkley, R. Dünner, T. Essinger-Hileman, R. P. Fisher, J. W. Fowler, A. Hajian, M. Halpern, M. Hasselfield, C. Hernández-Monteagudo, G. C. Hilton, M. Hilton, R. Hlozek, K. Huffenberger, D. Hughes, J. P. Hughes, L. Infante, K. D. Irwin, R. Jimenez, J. B. Juin, M. Kaul, J. Klein, A. Kosowsky, J. M. Lau, M. Limon, Y. -.

Lin, R. H. Lupton, T. Marriage, D. Marsden, K. Martocci, P. Mauskopf, F. Menanteau, K. Moodley, H. Moseley, C. B. Netterfield, M. D. Niemack, M. R. Nolta, L. A. Page, L. Parker, B. Partridge, H. Quintana, B. Reid, N. Sehgal, J. Sievers, D. N. Spergel, S. T. Staggs, O. Stryzak, D. Swetz, E. Switzer, R. Thornton, H. Trac, C. Tucker, L. Verde, R. Warne, G. Wilson, E. Wollack, and Y. Zhao. The Atacama Cosmology Telescope (ACT): Beam Profiles and First SZ Cluster Maps. *ArXiv e-prints*, July 2009.

T. Hirota, T. Bushimata, Y. K. Choi, M. Honma, H. Imai, K. Iwadate, T. Jike, S. Kameno, O. Kameya, R. Kamohara, Y. Kan-Ya, N. Kawaguchi, M. Kijima, M. K. Kim, H. Kobayashi, S. Kuji, T. Kurayama, S. Manabe, K. Maruyama, M. Matsui, N. Matsumoto, T. Miyaji, T. Nagayama, A. Nakagawa, K. Nakamura, C. S. Oh, T. Omodaka, T. Oyama, S. Sakai, T. Sasao, K. Sato, M. Sato, K. M. Shibata, M. Shintani, Y. Tamura, M. Tsushima, and K. Yamashita. Distance to Orion KL Measured with VERA. *PASJ*, 59:897–, October 2007.

G. Irwin, K. Hilton. *Cryogenic Particle Detection*. Springer, 2005.

M. J. Jee and J. A. Tyson. Dark Matter in the Galaxy Cluster CL J1226+3332 at z = 0.89. *ApJ*, 691:1337–1347, February 2009. doi: 10.1088/0004-637X/691/2/1337.

P. R. Jewell and R. M. Prestage. The Green Bank Telescope. In J. M. Oschmann Jr., editor, *Society of Photo-Optical Instrumentation Engineers (SPIE) Conference Series*, volume 5489 of *Presented at the Society of Photo-Optical Instrumentation Engineers (SPIE) Conference*, pages 312–323, October 2004. doi: 10.1117/12.550631.

T. A. Jones, A. M. Swinbank, R. S. Ellis, J. Richard, and D. P. Stark. Resolved spectroscopy of gravitationally lensed galaxies: recovering coherent velocity fields in subluminous z ˜ 2-3 galaxies. *MNRAS*, 404:1247–1262, May 2010. doi: 10.1111/j.1365-2966.2010.16378.x.

J. S. Kartaltepe, H. Ebeling, C. J. Ma, and D. Donovan. Probing the large-scale structure

around the most distant galaxy clusters from the massive cluster survey. *MNRAS*, 389: 1240–1248, September 2008. doi: 10.1111/j.1365-2966.2008.13620.x.

T. Kitayama, E. Komatsu, N. Ota, T. Kuwabara, Y. Suto, K. Yoshikawa, M. Hattori, and H. Matsuo. Exploring Cluster Physics with High-Resolution Sunyaev–Zel'dovich Effect Images and X-Ray Data: The Case of the Most X-Ray-Luminous Galaxy Cluster RX J1347-1145. *PASJ*, 56:17–28, February 2004.

E. Komatsu, H. Matsuo, T. Kitayama, M. Hattori, R. Kawabe, K. Kohno, N. Kuno, S. Schindler, Y. Suto, and K. Yoshikawa. Substructures Revealed by the Sunyaev-Zel'dovich Effect at 150 GHz in a High-Resolution Map of RX J1347-1145. *PASJ*, 53: 57–62, February 2001.

L. D. Landau and E. M. Lifshitz. *Fluid mechanics*. 1959.

S. J. LaRoque, M. Joy, J. E. Carlstrom, H. Ebeling, M. Bonamente, K. S. Dawson, A. Edge, W. L. Holzapfel, A. D. Miller, D. Nagai, S. K. Patel, and E. D. Reese. Sunyaev-Zeldovich Effect Imaging of MACS Galaxy Clusters at z larger than 0.5. *ApJ*, 583:559–565, February 2003. doi: 10.1086/345500.

S. J. LaRoque, M. Bonamente, J. E. Carlstrom, M. K. Joy, D. Nagai, E. D. Reese, and K. S. Dawson. X-Ray and Sunyaev-Zel'dovich Effect Measurements of the Gas Mass Fraction in Galaxy Clusters. *ApJ*, 652:917–936, December 2006. doi: 10.1086/508139.

D. A. Liedahl, A. L. Osterheld, and W. H. Goldstein. New calculations of Fe L-shell X-ray spectra in high-temperature plasmas. *ApJ*, 438:L115, January 1995. doi: 10.1086/187729.

M. Lima, B. Jain, M. Devlin, and J. Aguirre. Submillimeter Galaxy Number Counts and Magnification by Galaxy Clusters. *ApJ*, 717:L31–L36, July 2010. doi: 10.1088/2041-8205/717/1/L31.

M. Markevitch and A. Vikhlinin. Shocks and cold fronts in galaxy clusters. *Phys. Rep.*, 443:1–53, May 2007. doi: 10.1016/j.physrep.2007.01.001.

M. Markevitch, A. H. Gonzalez, L. David, A. Vikhlinin, S. Murray, W. Forman, C. Jones, and W. Tucker. A Textbook Example of a Bow Shock in the Merging Galaxy Cluster 1E 0657-56. *ApJ*, 567:L27–L31, March 2002a. doi: 10.1086/339619.

M. Markevitch, A. H. Gonzalez, L. David, A. Vikhlinin, S. Murray, W. Forman, C. Jones, and W. Tucker. A Textbook Example of a Bow Shock in the Merging Galaxy Cluster 1E 0657-56. *ApJ*, 567:L27–L31, March 2002b. doi: 10.1086/339619.

T. A. Marriage, V. Acquaviva, P. A. R. Ade, P. Aguirre, M. Amiri, J. W. Appel, L. F. Barrientos, E. S. Battistelli, J. R. Bond, B. Brown, B. Burger, J. Chervenak, S. Das, M. J. Devlin, S. R. Dicker, W. B. Doriese, J. Dunkley, R. Dunner, T. Essinger-Hileman, R. P. Fisher, J. W. Fowler, A. Hajian, M. Halpern, M. Hasselfield, C. Hern'andez-Monteagudo, G. C. Hilton, M. Hilton, A. D. Hincks, R. Hlozek, K. M. Huffenberger, D. H. Hughes, J. P. Hughes, L. Infante, K. D. Irwin, J. B. Juin, M. Kaul, J. Klein, A. Kosowsky, J. M. Lau, M. Limon, Y. -. Lin, R. H. Lupton, D. Marsden, K. Martocci, P. Mauskopf, F. Menanteau, K. Moodley, H. Moseley, C. B. Netterfield, M. D. Niemack, M. R. Nolta, L. A. Page, L. Parker, B. Partridge, H. Quintana, E. D. Reese, B. Reid, N. Sehgal, B. D. Sherwin, J. Sievers, D. N. Spergel, S. T. Staggs, D. S. Swetz, E. R. Switzer, R. Thornton, H. Trac, C. Tucker, R. Warne, G. Wilson, E. Wollack, and Y. Zhao. The Atacama Cosmology Telescope: Sunyaev Zel'dovich Selected Galaxy Clusters at 148 GHz in the 2008 Survey. *ArXiv e-prints*, October 2010.

B. S. Mason, S. T. Myers, and A. C. S. Readhead. A Measurement of Ho from the Sunyaev-Zeldovich Effect. *ApJ*, 555:L11–L15, July 2001. doi: 10.1086/321737.

B. S. Mason, S. R. Dicker, P. M. Korngut, M. J. Devlin, W. D. Cotton, P. M. Koch,

S. M. Molnar, J. Sievers, J. E. Aguirre, D. Benford, J. G. Staguhn, H. Moseley, K. D. Irwin, and P. Ade. Implications of a High Angular Resolution Image of the Sunyaev-Zel'Dovich Effect in RXJ1347-1145. *ApJ*, 716:739–745, June 2010. doi: 10.1088/0004-637X/716/1/739.

J. C. Mather, E. S. Cheng, R. E. Eplee, Jr., R. B. Isaacman, S. S. Meyer, R. A. Shafer, R. Weiss, E. L. Wright, C. L. Bennett, N. W. Boggess, E. Dwek, S. Gulkis, M. G. Hauser, M. Janssen, T. Kelsall, P. M. Lubin, S. H. Moseley, Jr., T. L. Murdock, R. F. Silverberg, G. F. Smoot, and D. T. Wilkinson. A preliminary measurement of the cosmic microwave background spectrum by the Cosmic Background Explorer (COBE) satellite. *ApJ*, 354: L37–L40, May 1990. doi: 10.1086/185717.

B. J. Maughan, L. R. Jones, H. Ebeling, and C. Scharf. An XMM-Newton observation of the massive, relaxed galaxy cluster ClJ1226.9+3332 at z= 0.89. *MNRAS*, 351:1193–1203, July 2004. doi: 10.1111/j.1365-2966.2004.07860.x.

B. J. Maughan, C. Jones, L. R. Jones, and L. Van Speybroeck. Deep XMM-Newton and Chandra Observations of Cl J1226.9+3332: A Detailed X-Ray Mass Analysis of a z = 0.89 Galaxy Cluster. *ApJ*, 659:1125–1137, April 2007. doi: 10.1086/512669.

B. R. McNamara, P. E. J. Nulsen, M. W. Wise, D. A. Rafferty, C. Carilli, C. L. Sarazin, and E. L. Blanton. The heating of gas in a galaxy cluster by X-ray cavities and large-scale shock fronts. *Nature*, 433:45–47, January 2005. doi: 10.1038/nature03202.

F. Menanteau, J. Gonzalez, J.-B. Juin, T. A. Marriage, E. Reese, V. Acquaviva, P. Aguirre, J. W. Appel, A. J. Baker, L. F. Barrientos, E. S. Battistelli, J. R. Bond, S. Das, M. J. Devlin, S. Dicker, A. J. Deshpande, J. Dunkley, R. Dunner, T. Essinger-Hileman, J. W. Fowler, A. Hajian, M. Halpern, M. Hasselfield, C. Hernandez-Monteagudo, M. Hilton, A. D. Hincks, R. Hlozek, J. P. Hughes, K. M. Huffenberger, L. Infante, K. D. Irwin,

J. Klein, A. Kosowsky, Y.-T. Lin, D. Marsden, K. Moodley, M. D. Niemack, M. R. Nolta, L. A. Page, L. Parker, B. Partridge, J. Sievers, N. Sehgal, D. N. Spergel, S. T. Staggs, D. Swetz, E. Switzer, R. Thornton, H. Trac, R. Warne, and E. Wollack. The Atacama Cosmology Telescope: Physical Properties and Purity of a Galaxy Cluster Sample Selected via the Sunyaev-Zel'dovich Effect. *ArXiv e-prints*, June 2010.

R. Mewe, E. H. B. M. Gronenschild, and G. H. J. van den Oord. Calculated X-radiation from optically thin plasmas. V. *A&AS*, 62:197, November 1985.

R. Mewe, J. R. Lemen, and G. H. J. van den Oord. Calculated X-radiation from optically thin plasmas. VI - Improved calculations for continuum emission and approximation formulae for nonrelativistic average Gaunt factors. *A&AS*, 65:511, September 1986.

M. Miranda, M. Sereno, E. de Filippis, and M. Paolillo. The dynamical state of RX J1347.5-1145 from a combined strong lensing and X-ray analysis. *MNRAS*, 385:511–518, March 2008. doi: 10.1111/j.1365-2966.2008.12855.x.

T. Mroczkowski, M. Bonamente, J. E. Carlstrom, T. L. Culverhouse, C. Greer, D. Hawkins, R. Hennessy, M. Joy, J. W. Lamb, E. M. Leitch, M. Loh, B. Maughan, D. P. Marrone, A. Miller, S. Muchovej, D. Nagai, C. Pryke, M. Sharp, and D. Woody. Application of a Self-Similar Pressure Profile to Sunyaev-Zel'Dovich Effect Data from Galaxy Clusters. *ApJ*, 694:1034–1044, April 2009. doi: 10.1088/0004-637X/694/2/1034.

S. Muchovej, T. Mroczkowski, J. E. Carlstrom, J. Cartwright, C. Greer, R. Hennessy, M. Loh, C. Pryke, B. Reddall, M. Runyan, M. Sharp, D. Hawkins, J. W. Lamb, D. Woody, M. Joy, E. M. Leitch, and A. D. Miller. Observations of High-Redshift X-Ray Selected Clusters with the Sunyaev-Zel'dovich Array. *ApJ*, 663:708–716, July 2007. doi: 10.1086/511971.

D. Nagai, A. V. Kravtsov, and A. Vikhlinin. Effects of Galaxy Formation on Thermodynamics of the Intracluster Medium. *ApJ*, 668:1–14, October 2007. doi: 10.1086/521328.

C. B. Netterfield, P. A. R. Ade, J. J. Bock, J. R. Bond, J. Borrill, A. Boscaleri, K. Coble, C. R. Contaldi, B. P. Crill, P. de Bernardis, P. Farese, K. Ganga, M. Giacometti, E. Hivon, V. V. Hristov, A. Iacoangeli, A. H. Jaffe, W. C. Jones, A. E. Lange, L. Martinis, S. Masi, P. Mason, P. D. Mauskopf, A. Melchiorri, T. Montroy, E. Pascale, F. Piacentini, D. Pogosyan, F. Pongetti, S. Prunet, G. Romeo, J. E. Ruhl, and F. Scaramuzzi. A Measurement by BOOMERANG of Multiple Peaks in the Angular Power Spectrum of the Cosmic Microwave Background. *ApJ*, 571:604–614, June 2002. doi: 10.1086/340118.

B. Nikolic, R. M. Prestage, D. S. Balser, C. J. Chandler, and R. E. Hills. Out-of-focus holography at the Green Bank Telescope. *A&A*, 465:685–693, April 2007. doi: 10.1051/0004-6361:20065765.

M. Nord, K. Basu, F. Pacaud, P. A. R. Ade, A. N. Bender, B. A. Benson, F. Bertoldi, H.-M. Cho, G. Chon, J. Clarke, M. Dobbs, D. Ferrusca, N. W. Halverson, W. L. Holzapfel, C. Horellou, D. Johansson, J. Kennedy, Z. Kermish, R. Kneissl, T. Lanting, A. T. Lee, M. Lueker, J. Mehl, K. M. Menten, T. Plagge, C. L. Reichardt, P. L. Richards, R. Schaaf, D. Schwan, H. Spieler, C. Tucker, A. Weiss, and O. Zahn. Multi-frequency imaging of the galaxy cluster Abell 2163 using the Sunyaev-Zel'dovich effect. *A&A*, 506:623–636, November 2009. doi: 10.1051/0004-6361/200911746.

C. R. O'dell. The Orion Nebula and its Associated Population. *ARA&A*, 39:99–136, 2001. doi: 10.1146/annurev.astro.39.1.99.

N. Ota, K. Murase, T. Kitayama, E. Komatsu, M. Hattori, H. Matsuo, T. Oshima, Y. Suto, and K. Yoshikawa. Suzaku broad-band spectroscopy of RX J1347.5-1145: constraints on the extremely hot gas and non-thermal emission. *ArXiv e-prints*, May 2008.

P. Oxley, P. A. Ade, C. Baccigalupi, P. deBernardis, H.-M. Cho, M. J. Devlin, S. Hanany, B. R. Johnson, T. Jones, A. T. Lee, T. Matsumura, A. D. Miller, M. Milligan, T. Renbarger, H. G. Spieler, R. Stompor, G. S. Tucker, and M. Zaldarriaga. The EBEX experiment. In M. Strojnik, editor, *Society of Photo-Optical Instrumentation Engineers (SPIE) Conference Series*, volume 5543 of *Society of Photo-Optical Instrumentation Engineers (SPIE) Conference Series*, pages 320–331, November 2004. doi: 10.1117/12.563447.

L. Page, M. R. Nolta, C. Barnes, C. L. Bennett, M. Halpern, G. Hinshaw, N. Jarosik, A. Kogut, M. Limon, S. S. Meyer, H. V. Peiris, D. N. Spergel, G. S. Tucker, E. Wollack, and E. L. Wright. First-Year Wilkinson Microwave Anisotropy Probe (WMAP) Observations: Interpretation of the TT and TE Angular Power Spectrum Peaks. *ApJS*, 148: 233–241, September 2003. doi: 10.1086/377224.

Y. N. Pariiskii. Detection of Hot Gas in the Coma Cluster of Galaxies. *AZh*, 49:1322–+, December 1972.

T. J. Pearson, B. S. Mason, A. C. S. Readhead, M. C. Shepherd, J. L. Sievers, P. S. Udomprasert, J. K. Cartwright, A. J. Farmer, S. Padin, S. T. Myers, J. R. Bond, C. R. Contaldi, U.-L. Pen, S. Prunet, D. Pogosyan, J. E. Carlstrom, J. Kovac, E. M. Leitch, C. Pryke, N. W. Halverson, W. L. Holzapfel, P. Altamirano, L. Bronfman, S. Casassus, J. May, and M. Joy. The Anisotropy of the Microwave Background to l = 3500: Mosaic Observations with the Cosmic Background Imager. *ApJ*, 591:556–574, July 2003. doi: 10.1086/375508.

A. A. Penzias and R. W. Wilson. A Measurement of Excess Antenna Temperature at 4080 Mc/s. *ApJ*, 142:419–421, July 1965. doi: 10.1086/148307.

T. Plagge, B. A. Benson, P. A. R. Ade, K. A. Aird, L. E. Bleem, J. E. Carlstrom, C. L. Chang, H.-M. Cho, T. M. Crawford, A. T. Crites, T. de Haan, M. A. Dobbs, E. M.

George, N. R. Hall, N. W. Halverson, G. P. Holder, W. L. Holzapfel, J. D. Hrubes, M. Joy, R. Keisler, L. Knox, A. T. Lee, E. M. Leitch, M. Lueker, D. Marrone, J. J. McMahon, J. Mehl, S. S. Meyer, J. J. Mohr, T. E. Montroy, S. Padin, C. Pryke, C. L. Reichardt, J. E. Ruhl, K. K. Schaffer, L. Shaw, E. Shirokoff, H. G. Spieler, B. Stalder, Z. Staniszewski, A. A. Stark, K. Vanderlinde, J. D. Vieira, R. Williamson, and O. Zahn. Sunyaev-Zel'dovich Cluster Profiles Measured with the South Pole Telescope. *ApJ*, 716: 1118–1135, June 2010. doi: 10.1088/0004-637X/716/2/1118.

E. Pointecouteau, M. Giard, A. Benoit, F. X. Désert, N. Aghanim, N. Coron, J. M. Lamarre, and J. Delabrouille. A Sunyaev-Zeldovich Map of the Massive Core in the Luminous X-Ray Cluster RX J1347-1145. *ApJ*, 519:L115–L118, July 1999. doi: 10.1086/312117.

E. Pointecouteau, M. Giard, A. Benoit, F. X. Désert, J. P. Bernard, N. Coron, and J. M. Lamarre. Extended Sunyaev-Zeldovich Map of the Most Luminous X-Ray Cluster, RX J1347-1145. *ApJ*, 552:42–48, May 2001. doi: 10.1086/320447.

G. B. Poole, A. Babul, I. G. McCarthy, A. J. R. Sanderson, and M. A. Fardal. The impact of mergers on relaxed X-ray clusters - III. Effects on compact cool cores. *MNRAS*, 391: 1163–1175, December 2008. doi: 10.1111/j.1365-2966.2008.14003.x.

W. H. Press, S. A. Teukolsky, W. T. Vetterling, B. P. Flannery, C. Lloyd, P. Rees, S. A. Teukolsky, W. T. Vetterling, B. P. Flannery, C. Lloyd, and P. Rees. Book Review: Numerical recipes in C: the art of scientific computing / Cambridge U Press, 1993. *The Observatory*, 113:214–+, August 1993.

E. D. Reese, J. J. Mohr, J. E. Carlstrom, M. Joy, L. Grego, G. P. Holder, W. L. Holzapfel, J. P. Hughes, S. K. Patel, and M. Donahue. Sunyaev-Zeldovich Effect-derived Distances to the High-Redshift Clusters MS 0451.6-0305 and CL 0016+16. *ApJ*, 533:38, April 2000. doi: 10.1086/308662.

E. D. Reese, J. E. Carlstrom, M. Joy, J. J. Mohr, L. Grego, and W. L. Holzapfel. Determining the Cosmic Distance Scale from Interferometric Measurements of the Sunyaev-Zeldovich Effect. *ApJ*, 581:53–85, December 2002. doi: 10.1086/344137.

E. D. Reese, H. Kawahara, T. Kitayama, N. Ota, S. Sasaki, and Y. Suto. Impact of Chandra Calibration Uncertainties on Galaxy Cluster Temperatures: Application to the Hubble Constant. *ApJ*, 721:653, September 2010. doi: 10.1088/0004-637X/721/1/653.

M. Rex, P. A. R. Ade, I. Aretxaga, J. J. Bock, E. L. Chapin, M. J. Devlin, S. R. Dicker, M. Griffin, J. O. Gundersen, M. Halpern, P. C. Hargrave, D. H. Hughes, J. Klein, G. Marsden, P. G. Martin, P. Mauskopf, A. Montaña, C. B. Netterfield, L. Olmi, E. Pascale, G. Patanchon, D. Scott, C. Semisch, N. Thomas, M. D. P. Truch, C. Tucker, G. S. Tucker, M. P. Viero, and D. V. Wiebe. A Bright Submillimeter Source in the Bullet Cluster (1E0657-56) Field Detected with Blast. *ApJ*, 703:348–353, September 2009. doi: 10.1088/0004-637X/703/1/348.

J. et. al. Richard. Dark matter in macs0744. 2011, in prep.

P. R. Roach. Kevlar support for thermal isolation at low temperatures. *Review of Scientific Instruments*, 63:3216–+, May 1992. doi: 10.1063/1.1142582.

A. Sajina, B. Partridge, T. Evans, S. Stefl, N. Vechik, S. Myers, S. Dicker, and P. Korngut. High frequency radio SEDs and polarization fractions of sources in an ACT survey field. *ArXiv e-prints*, January 2011.

C. L. Sarazin. The Physics of Cluster Mergers. In L. Feretti, I. M. Gioia, & G. Giovannini, editor, *Merging Processes in Galaxy Clusters*, volume 272 of *Astrophysics and Space Science Library*, pages 1–38, June 2002.

S. Y. Sazonov and R. A. Sunyaev. Cosmic Microwave Background Radiation in the Direc-

tion of a Moving Cluster of Galaxies with Hot Gas: Relativistic Corrections. *ApJ*, 508: 1–5, November 1998. doi: 10.1086/306406.

S. Schindler, M. Hattori, D. M. Neumann, and H. Boehringer. ROSAT/HRI and ASCA observations of the most luminous X-ray cluster RX J1347.5-1145. *A&A*, 317:646–655, February 1997.

Y. L. Shirley, B. S. Mason, J. G. Mangum, D. E. Bolin, M. J. Devlin, S. R. Dicker, and P. M. Korngut. Mustang 3.3 mm Continuum Observations of Class 0 Protostars. *AJ*, 141:39–+, February 2011. doi: 10.1088/0004-6256/141/2/39.

G. F. Smoot, M. V. Gorenstein, and R. A. Muller. Detection of anisotropy in the cosmic blackbody radiation. *Physical Review Letters*, 39:898–901, October 1977. doi: 10.1103/PhysRevLett.39.898.

R. A. Sunyaev and Y. B. Zeldovich. The Observations of Relic Radiation as a Test of the Nature of X-Ray Radiation from the Clusters of Galaxies. *Comments on Astrophysics and Space Physics*, 4:173–+, November 1972.

Y. D. Takahashi, P. A. R. Ade, D. Barkats, J. O. Battle, E. M. Bierman, J. J. Bock, H. C. Chiang, C. D. Dowell, L. Duband, E. F. Hivon, W. L. Holzapfel, V. V. Hristov, W. C. Jones, B. G. Keating, J. M. Kovac, C. L. Kuo, A. E. Lange, E. M. Leitch, P. V. Mason, T. Matsumura, H. T. Nguyen, N. Ponthieu, C. Pryke, S. Richter, G. Rocha, and K. W. Yoon. Characterization of the BICEP Telescope for High-precision Cosmic Microwave Background Polarimetry. *ApJ*, 711:1141–1156, March 2010. doi: 10.1088/0004-637X/711/2/1141.

M. Takizawa. Two-Temperature Intracluster Medium in Merging Clusters of Galaxies. *ApJ*, 520:514–528, August 1999. doi: 10.1086/307497.

Michael. Tinkham. *Introduction to Superconductivity*. McGraw-Hill, 1996.

K. Vanderlinde, T. M. Crawford, T. de Haan, J. P. Dudley, L. Shaw, P. A. R. Ade, K. A. Aird, B. A. Benson, L. E. Bleem, M. Brodwin, J. E. Carlstrom, C. L. Chang, A. T. Crites, S. Desai, M. A. Dobbs, R. J. Foley, E. M. George, M. D. Gladders, N. R. Hall, N. W. Halverson, F. W. High, G. P. Holder, W. L. Holzapfel, J. D. Hrubes, M. Joy, R. Keisler, L. Knox, A. T. Lee, E. M. Leitch, A. Loehr, M. Lueker, D. P. Marrone, J. J. McMahon, J. Mehl, S. S. Meyer, J. J. Mohr, T. E. Montroy, C. -. Ngeow, S. Padin, T. Plagge, C. Pryke, C. L. Reichardt, A. Rest, J. Ruel, J. E. Ruhl, K. K. Schaffer, E. Shirokoff, J. Song, H. G. Spieler, B. Stalder, Z. Staniszewski, A. A. Stark, C. W. Stubbs, A. van Engelen, J. D. Vieira, R. Williamson, Y. Yang, O. Zahn, and A. Zenteno. Galaxy Clusters Selected with the Sunyaev-Zel'dovich Effect from 2008 South Pole Telescope Observations. *ArXiv e-prints*, March 2010.

L. Verde, H. V. Peiris, D. N. Spergel, M. R. Nolta, C. L. Bennett, M. Halpern, G. Hinshaw, N. Jarosik, A. Kogut, M. Limon, S. S. Meyer, L. Page, G. S. Tucker, E. Wollack, and E. L. Wright. First-Year Wilkinson Microwave Anisotropy Probe (WMAP) Observations: Parameter Estimation Methodology. *ApJS*, 148:195, September 2003. doi: 10.1086/377335.

A. Vikhlinin, M. Markevitch, and S. S. Murray. A Moving Cold Front in the Intergalactic Medium of A3667. *ApJ*, 551:160–171, April 2001. doi: 10.1086/320078.

J. L. Weiland, N. Odegard, R. S. Hill, E. Wollack, G. Hinshaw, M. R. Greason, N. Jarosik, L. Page, C. L. Bennett, J. Dunkley, B. Gold, M. Halpern, A. Kogut, E. Komatsu, D. Larson, M. Limon, S. S. Meyer, M. R. Nolta, K. M. Smith, D. N. Spergel, G. S. Tucker, and E. L. Wright. Seven-Year Wilkinson Microwave Anisotropy Probe (WMAP) Observations: Planets and Celestial Calibration Sources. *ArXiv e-prints*, January 2010.

R. L. White, R. H. Becker, D. J. Helfand, and M. D. Gregg. A Catalog of 1.4 GHz Radio Sources from the FIRST Survey. *ApJ*, 475:479–+, February 1997. doi: 10.1086/303564.

G. W. Wilson, D. H. Hughes, I. Aretxaga, H. Ezawa, J. E. Austermann, S. Doyle, D. Ferrusca, I. Hernández-Curiel, R. Kawabe, T. Kitayama, K. Kohno, A. Kuboi, H. Matsuo, P. D. Mauskopf, Y. Murakoshi, A. Montaña, P. Natarajan, T. Oshima, N. Ota, T. A. Perera, J. Rand, K. S. Scott, K. Tanaka, M. Tsuboi, C. C. Williams, N. Yamaguchi, and M. S. Yun. A bright, dust-obscured, millimetre-selected galaxy beyond the Bullet Cluster (1E0657-56). *MNRAS*, 390:1061–1070, November 2008. doi: 10.1111/j.1365-2966.2008.13774.x.

M. Yan, H. R. Sadeghpour, and A. Dalgarno. Photoionization Cross Sections of He and H 2. *ApJ*, 496:1044, March 1998.

Y. B. Zeldovich and R. A. Sunyaev. The Interaction of Matter and Radiation in a Hot-Model Universe. *Ap&SS*, 4:301–316, July 1969. doi: 10.1007/BF00661821.

A. Zitrin, T. Broadhurst, R. Barkana, Y. Rephaeli, and N. Benitez. Strong-Lensing Analysis of a Complete Sample of 12 MACS Clusters at z0.5: Mass Models and Einstein Radii. *ArXiv e-prints*, February 2010.

J. A. ZuHone, M. Markevitch, and R. E. Johnson. Stirring Up the Pot: Can Cooling Flows In Galaxy Clusters Be Quenched By Gas Sloshing? *ArXiv e-prints*, December 2009.